Integrated optical and mechanical resonators for evanescent field sensing

BY

Callum Doolin

A thesis submitted in partial fulfillment of the requirements for

the degree of

Doctor of Philosophy

Department of Physics

University of Alberta

Abstract

Nanoscale optical and mechanical resonators store energy in a way characterized by a sharp resonance frequency, and through interaction with their surroundings offer a path to the next generation of sensitive measurement tools. In this thesis we investigate a particular geometry of nanofabricated devices—that of monolithically fabricated optical microdisks and nanomechanical resonators, in which the optical microdisk operates as a high-gain amplifier of the mechanical resonator's position.

We began the study with nanoscale silicon microdisks and cantilevers fabricated with a commercial photolithography process for silicon photonics, and used the optomechanical interaction between the cantilevers and optical microdisks to demonstrate readout of the mechanical motion to the $\mathrm{fm\,Hz}^{-1/2}$ precision level. This approach has enabled thermally limited readout of forces on the cantilever to 130 ± 40 $\mathrm{aN\,Hz}^{-1/2}$ at room temperature, optimized by their nanometer-sized geometry and femtogram-scale masses. We then explored the possibility of using these cantilevers for fundamental quantum measurements of phonon number, and although we concluded the cantilever measurement lacked the necessary characteristics, we developed a framework for characterizing the type of optomechanical coupling exhibited by an optomechanical device.

Continuing on resonator development, we switched to fabricating similar geometry optomechanical devices from silicon nitride, an insulating material used in semiconductor fabrication, known to enable a high quality factor mechanical resonator geometry termed nanostrings. Using a fiber-waveguide coupling technique we were able to optomechanically measure picogram-scale nanostring devices down to temperatures below 1 K, finding mechanical quality factors of 10^6, while exhibiting less optically-induced heating than similar silicon devices. While the optical microdisks enable high-precision readout of mechanical motion, they more generally measure

refractive index changes. Using aqueously submerged silicon nitride microdisks, we were able to measure LiCl induced refractive index changes down to the 10^{-6} level.

Finally, we carry out a discussion and review on the subject of digital signal processing. Although appearing unrelated, the techniques covered in Chapter 7 underline every single experimental result covered in this thesis. With an understanding of digital signals, flexible and well adapted measurement protocols can be constructed without being stuck relying on the output of fixed-pipeline measurement tools.

Acknowledgements

This thesis would in no way be possible without the time, support, and enthusiasm provided by Dr. John P Davis throughout the tenure of my doctoral studies. Additionally everyone else involved during my time in the Davis Lab, including Paul Kim, Brad Hauer, Allison MacDonald, Hugh Ramp, Tushar Biswas, Yikai Yang, Clinton Potts, Xavier Rojas, Fabien Souris, Greg Popowich, Kyle Reid, Tommy Clark, Holly Christiani, Alex Shook, Vaisakh Vadakkumbatt, Sean McClure, Matt Rudd, and everyone else I have missed.

I'd like to thank my brother, Pearse Doolin, for (perhaps at the detriment of this thesis) pushing us on the adventure of a lifetime in starting Resolved Instruments Inc., of which John deserve additional thanks for without his involvement, support, and patience it would have never been possible.

The rest of my family—my parents Gary Doolin and Cathy McCabe, and brother Jesse Doolin—for their support throughout this process.

And finally Emma Schmidt who has made the last four years the best years of my life, and which I can only see getting better.

Contents

List of Tables

List of Figures

Chapter 1

Introduction

1.1 Optical microdisks

Optical cavities capable of trapping light for many round trips of the cavity are a well studied nanosystem [1]. They act interferometrically, displaying buildup of optical power when the round trip path length matches integer multiples of the light wavelength [2]. These cavities can exhibit large quality factors (Qs), defined as the stored cavity energy per unit energy lost per cavity cycle. These large Qs sharply define the resonance frequency of the cavity, making these resonators of great interest for a variety of signal processing and quantum applications, as well as in sensing applications where the resonance frequency strongly depends on the index of refraction sampled by the optical field.

Optical cavities come in a variety of geometries. The canonical picture of an optical cavity is that of a Fabry-Pérot cavity—two separated mirrors, with one slightly transmitting such that light can enter and leave the cavity. At the smallest scale, photonic crystal (PC) cavities use metamaterial photonic bandgaps to define optical cavities in dielectric materials [3].

Optical whispering-gallery-mode (WGM) resonators trap light in a circular path, borrowing their name from the acoustic phenomena first correctly described by Lord Rayleigh from his observations of the 33 m diameter dome of St. Paul's cathedral [4]. Scaling the ∼1 m wavelength of the note F4 (349 Hz) to the ∼1 μm wavelength of near-infrared light (300 THz), optical whispering-gallery modes would be expected in circular cavities ∼30 μm in diameter, and correspondingly WGMs with diameters from a few micrometers up to the millimeter scale have been described. Glass spheres and toroids represent the larger WGMs, using the surface tension of melted glass to form very smooth radial surfaces minimizing scattering losses and achieving ultra-high Qs > 10^9 [5, 6]. At the smaller scale, optical microdisks can be fabricated with planar top-down micro/nano-fabrication techniques—similar to PCs—however are simpler to design, have relaxed fabrication requirements, and can be designed with narrow line-widths and large Qs up to 10^6 [7]. For these reasons, we have focused on using planar whispering-gallery mode microdisk resonators as sensors to detect index of refraction changes in the microdisk near-field.

In a WGM resonator, the evanescent field of the optical mode will extend outside of the resonator into the surrounding medium. Refractive index changes of the surrounding medium shift the resonance condition, providing the ability to monitor polarizability of the microdisk environment by monitoring the optical mode frequency. This technique has been used to great success, and sensors based on whispering-gallery mode resonators have been used for the label-free detection of single viruses [8, 9], nanoparticles [10, 11, 12, 13], single proteins [14], nucleotides [15, 16], and are even being used commercially [17].

In Chapter 6 we describe the use of silicon nitride microdisk resonators to detect the bulk index of refraction change in water due to the addition of LiCl, and find we are able to measure refractive index changes with a limit of detection near 10^{-6} refractive index units.

Optical resonators have been used to detect the motion of nanomechanical resonators placed in the near-field with great precision, below the imprecision required to satisfy Heisenberg's uncertainty principle for a continuous measurement—the so-called standard quantum limit [18, 19, 20]. This measurement precision has encouraged interest in the field of cavity optomechanics, exploring the interactions between a tightly coupled optical cavity and mechanical resonator, often with the goal of observing quantum effects. In Chapters 3–5 we will describe the use of optical WGM cavities to measure the motion of mechanical resonators, both for sensing applications, and with the possible use in studying quantum effects of mesoscale mechanical resonators.

1.2 Mechanical resonators

While the previously described optical sensors probe the environment electromagnetically, mechanical resonators interact in a physically intuitive manner. In the simplest sense, mechanical sensors respond via Hooke's law, $F = -kx$, for a given force the mechanical resonator will deflect a proportional distance. Going beyond Hooke's law, it is possible to model the dynamic response of the mechanical resonator as a simple harmonic oscillator with an effective mass different, and usually smaller, than the geometric mass resonator [21]. These resonators exhibit characteristic motion dependent on resonator properties, and AC forces applied near the resonant frequency transduce well to large displacements [22]. Operation of these mechanical resonators at relatively high frequencies reduce environmental $1/f$ noise where the signal can be better isolated and well measured by present high-speed electronics [23, 24, 25].

Fabricating smaller, higher frequency mechanical resonators is a proven way to increase performance in a damped environment [26, 22]. However, measuring the resonator's position becomes difficult—particularly as dimensions fall below the spot size

of a laser beam ($\sim$1 µm)—and optical methods to detect nanotubes and nanowires only achieve $\mathrm{pm\,Hz^{-1/2}}$ sensitivity [27, 28, 29], compared with the 5 $\mathrm{fm\,Hz^{-1/2}}$ sensitivity achieved using optical beam deflection [30], or the 2 $\mathrm{fm\,Hz^{-1/2}}$ sensitivity achieved with interferometry [31], on standard low-frequency (300 kHz) cantilevers. Using the refractive index sensitivity of a WGM cavity, positioning a nanomechanical resonator in the near-field of an optical microdisk can allow the mechanical motion to be measured with great accuracy, down to the $\mathrm{fm\,Hz^{-1/2}}$ scale [32, 33, 22]. Using nanometer-sized resonators with femtogram effective masses, fabricated beside a microdisk to decouple mechanics and optics, we have measured position imprecision of 2 $\mathrm{fm\,Hz^{-1/2}}$ as will be shown in Chapter 3.

Chapter 2

Theory of optical and mechanical devices

2.1 Theory of optical resonators

We will begin our treatment of optical resonators from the quantum perspective, and then quickly reduce to a classical treatment. An optical cavity resonant with light oscillating at angular frequency ω_0 can be modelled as a quantum harmonic oscillator with the Hamiltonian

$$\hat{H}_{\text{opt}} = \hbar\omega_0 \left(\hat{a}^\dagger \hat{a} + \frac{1}{2} \right), \tag{2.1}$$

where $\hbar$ is the reduced Planck constant and $\hat{a}^\dagger$ and $\hat{a}$ are the raising and lowering operators normalized such that $\hat{n} = \hat{a}^\dagger \hat{a}$ is the photon number operator of the optical cavity. From the Hamiltonian the Heisenberg equations of motions can be found,

$$\dot{\hat{a}} = -i\omega_0 \hat{a} \tag{2.2}$$

$$\dot{\hat{a}}^\dagger = i\omega_0 \hat{a}^\dagger, \tag{2.3}$$

giving two uncoupled first-order time-dependent differential equations for $\hat{a}$ and $\hat{a}^\dagger$. While these equations are simplistic and don't contain much of the optical resonance behavior we wish to describe, they provide a starting point for further analysis.

At this point, we will drop the quantum-mechanical description and treat $a(t) = \langle \hat{a}(t) \rangle$, and $a^\dagger(t) = \langle \hat{a}^\dagger(t) \rangle$, as classical, unitless, complex field amplitudes for the optical resonator, normalized such that $|a(t)|^2$ represents the number of photons in the resonator. Doing so we can quickly identify $a(t) = |a|e^{-i\omega_0 t}$ and $a^\dagger(t) = |a^\dagger|e^{i\omega_0 t}$ as solutions to equations (2.2) and (2.3), identifying $a(t)$ and $a^\dagger(t)$ as the negative and positive frequency modes, corresponding in the whispering-gallery mode resonator as clockwise and counter-clockwise propagating solutions.

2.1.1 Coupling to an optical resonator

Following the treatment of coupled resonators developed by H.A. Haus [34], we will add coupling terms to the differential equation for $a(t)$. We will focus on only one of these solutions, $a(t)$, from which we can find the energy in the resonator as $|a(t)|^2 = a^*(t)a(t)$, where $a^*(t)$ the complex conjugate of $a(t)$.

First, we will introduce the intrinsic loss rate of the resonator, κ_0:

$$\dot{a}(t) = -i\omega_0 a(t) - \kappa_0 a(t). \tag{2.4}$$

This equation can be solved to find the solution for the field, $a(t) = a_0 e^{-\kappa_0 t + i\omega_0 t}$, such that the energy (number of photons) in the resonator is $|a(t)|^2 = a_0^2 e^{-2\kappa_0 t}$, starting from the initial energy of a_0^2 and decaying at a rate of $2\kappa_0$. From here we can define the quality factor of a resonator as

$$Q \equiv \omega_0 \frac{W}{P_\mathrm{d}}, \tag{2.5}$$
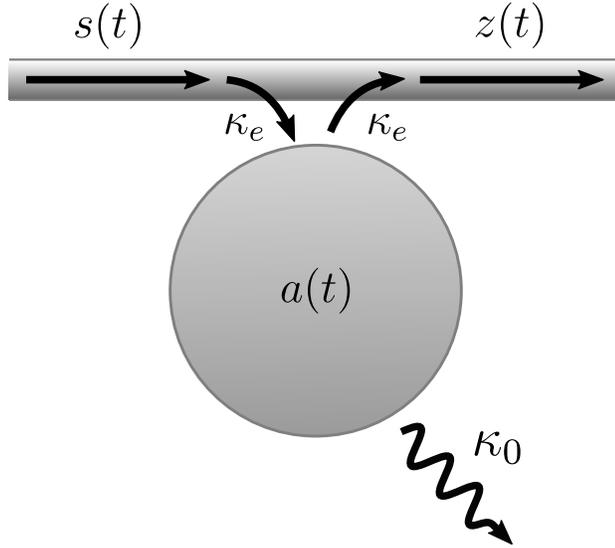
Figure 2.1: A schematic of the model used for coupling to the optical microdisk. An optical field with complex amplitude $s(t)$, carrying power $|s(t)|^2$, is incident on the microdisk coupling light to the disk at a rate κ_e, while an optical field with complex amplitude $z(t)$ takes light away from the microdisk. The microdisk supports an optical mode with energy $|a(t)|^2$, which is lost to the surroundings at a rate κ_0 and to the outgoing field at a rate κ_e such that the total losses from the microdisk are $\kappa = \kappa_0 + \kappa_e$. The field in the microdisk is modeled by equation (2.7) in the text, while the outgoing field $z(t)$ is modeled by equation (2.11).

where W is the energy stored in the resonator, and P_d is the power dissipated from the resonator [2]. Recognizing $W = |a(t)|^2$ and $P_\mathrm{d} = -d|a(t)|^2/dt = 2\kappa_0$, we find for an optical resonator described by equation (2.4),

$$Q_0 = \frac{\omega_0}{2\kappa_0}. \tag{2.6}$$

Next we add coupling to the microdisk. As illustrated in Figure 2.1, the optical microdisk is interfaced with a waveguide running adjacent the microdisk such that the evanescent field of the waveguide and the microdisk overlap, resulting in coupling. Incident towards the microdisk in the waveguide is a field $s(t) = \bar{s}e^{-i\omega t}$ generated by

a laser tuned to the optical frequency ω, and carrying power $|s(t)|^2 = \bar{s}^2$. Away from the microdisk, the waveguide carries field $z(t)$ with power $|z(t)|^2$.

Adding this interaction involves two modifications to equation (2.4), first an additional loss rate from the optical resonator to the waveguide at rate κ_e. This loss is in addition to the intrinsic loss rate κ_0, such that the total loss rate is $\kappa = \kappa_0 + \kappa_e$, resulting in a loaded Q of $Q = \omega_0/2\kappa$. Second, a coupling from the incoming waveguide to the optical mode is added, the magnitude of which can be related to κ_e through time-reversal symmetry (again, following the procedure of H.A. Haus [34]), such that the waveguide-coupled equations of motion are

$$\dot{a}(t) = -i\omega_0 a(t) - \kappa a(t) + \sqrt{2\kappa_e}s(t). \tag{2.7}$$

We can analyze this equation with complex sinusoids (effectively similar to a Fourier transform). If the driving field $s(t)$ is rotating with a complex phase $e^{-i\omega t}$, then the response, $a(t)$, will also occur at the same frequency, with a possible amplitude and phase shift, i.e., $a(t) = \bar{a}e^{-i\omega t}$, and $s(t) = \bar{s}e^{-i\omega t}$, where $\bar{a}$ and $\bar{s}$ are complex constants. Using these functional forms we find

$$a(t) = \frac{\sqrt{2\kappa_e}}{\kappa - i\Delta}s(t) \tag{2.8}$$

where we have introduced $\Delta = \omega - \omega_0$, the detuning of the laser frequency from the cavity resonance frequency.

2.1.2 Transmission from an optical resonator

Finally, we would like to solve for $z(t)$, the transmitted waveguide field travelling away from the optical cavity. We start by recognizing that in linear media, the solution should be a linear combination of $s(t)$ and $a(t)$: $z(t) = c_1 s(t) + c_2 a(t)$, where c_1 and c_2 are unknown complex constants. Using power conservation in the case of a perfect

cavity ($\kappa_0 = 0$), we can relate the incoming power, $|s(t)|^2$, the power loss from the cavity,

$$-\frac{d}{dt}|a(t)|^2 = 2\kappa_e|a(t)|^2 - \sqrt{2\kappa_e}(s^*(t)a(t) + a^*(t)s(t)),$$ (2.9)

and the power leaving the waveguide,

$$|z(t)|^2 = |c_1|^2|s(t)|^2 + c_1c_2(s^*(t)a(t) + a^*(t)s(t)) + |c_2|^2|a(t)|^2,$$ (2.10)

such that $|z(t)|^2$ - $|s(t)|^2 = -(d/dt)|a(t)|^2$. If we consider the case with no incident field—$s(t) = 0$, we find $|c_2|^2 = 2\kappa_e$ [34]. Then considering a nonzero $s(t)$, we find $c_1 = -1$, such that the transmitted field is

$$z(t) = -s(t) + \sqrt{2\kappa_e}a(t),$$ (2.11)

with an arbitrary phase-relation between $a(t)$ and $z(t)$ that corresponds to the choice of where the measurement of $z(t)$ is performed. The power transmitted to the outgoing waveguide is then be found to be

$$|z(t)|^2 = |s(t)|^2 - 2\kappa_0|a(t)|^2,$$ (2.12)

corresponding to the signal detected when incident on a photodiode.

2.2 Theory of mechanical resonators

A simple, yet powerful, model of a mechanical resonator is the mass on a spring. We will use this model to describe mechanical resonators that occupy distributed volumes of space, and will do this by attributing an effective mass to the resonator such that is can be described as a point mass with mass m_{eff} [21]. Basing ourselves in Newtonian physics, the position of the mass and the forces applied to it, F, are

linearly proportional and given by Hooke's law:

$$F_{\text{spring}} = -kx, \tag{2.13}$$

where k is the spring-constant, and x is displacement from the equilibrium position of the mass.

This equation describes the static case, but to describe the dynamic, time-dependent motion of the resonator, its mass (or effective mass), providing resistance to changes in motion must be considered. Using Newton's second law of motion, $F_{\text{accel}} = m_{\text{eff}}a$, where $a = \ddot{x}$ is the acceleration (second derivative) of the mass's position, we can equate the acceleration and spring forces to find the second-order differential equation

$$m_{\text{eff}}\ddot{x}(t) = -kx(t), \tag{2.14}$$

of which $x = \bar{x}\cos(\Omega_0 t)$ is quickly recognized as a solution. That is, the mass oscillates sinusoidally with amplitude $\bar{x}$ (determined by the condition $x(0) = \bar{x}$) at an angular frequency

$$\Omega_0 = \sqrt{\frac{k}{m_{\text{eff}}}}. \tag{2.15}$$

While this model illustrates an important characteristic of the mass-on-a-spring system—oscillation at a constant frequency—it can be further improved. As modelled so far, the mass will oscillate at the same amplitude indefinitely, but as we all know everything is impermanent.

To remedy this, we will add the phenomenological damping force opposing the velocity of the resonator,

$$F_{\text{damp}} = -m_{\text{eff}}\Gamma\dot{x}, \tag{2.16}$$

where Γ is the damping rate, such that equating the inertial, damping, and spring forces (recognizing $k = m_{\text{eff}}\Omega_0^2$) yields

$$m_{\text{eff}}\ddot{x} + m_{\text{eff}}\Gamma\dot{x} + m_{\text{eff}}\Omega_0^2 x = 0. \tag{2.17}$$

Solving this by substituting the complex ansatz $x(t) = \bar{x}e^{rt}$ we find two solutions, $x_+(t)$ and $x_-(t)$,

$$x_\pm(t) = \bar{x}e^{-\frac{\Gamma}{2}t \pm i\Omega_0\sqrt{(1-\Gamma^2/4\Omega_0^2)}t}, \tag{2.18}$$

where we are assuming $\Gamma/2 < \Omega_0$—well satisfied by the mechanical resonators studied later. This equation illustrates two important effects of the damping term Γ. First, the oscillating frequency of the resonator is slightly perturbed from the undamped situation, being reduced by a factor of $\sqrt{(1-\Gamma^2/4\Omega_0^2)}$. This effect is often neglected as, for instance, in the devices studied in Chapters 3–5, $\Gamma/\Omega_0 < 10^{-3}$, putting the frequency correction below the part-per-million level. In the limit of $\Gamma/\Omega_0 \ll 1$, we can and will ignore the second-order corrections. Second, and more importantly, the amplitude of the mechanical motion,

$$|x_\pm(t)| = \bar{x}e^{-\frac{\Gamma}{2}t}, \tag{2.19}$$

exponentially decays at the rate $\Gamma/2$.

As described in equation (2.18), $x_\pm(t)$ are complex variables. Since the position of the mechanical object should generally be a real number, we must use a linear combination of x_+ and x_- to achieve this. Two convenient and orthogonal choices are

$$\begin{aligned}
x_{\text{i}}(t) &= \frac{x_+(t) + x_-(t)}{2} \\
&= \bar{x}e^{-\Gamma t/2}\cos(\Omega_0 t)
\end{aligned} \tag{2.20}$$

and

$$x_q(t) = \frac{x_+(t) - x_-(t)}{2i}$$

$$= \bar{x}e^{-\Gamma t/2}\sin(\Omega_0 t) \tag{2.21}$$

which are labelled to refer to the *in-phase* and *quadrature* components of x_+; $x_i = \text{Re}(x_+)$ and $x_q = \text{Im}(x_+)$.

2.2.1 Energy and quality factor

The energy (E) of a mechanical resonator is the sum of its kinetic (T) and potential (U) energies:

$$E = \frac{p^2}{2m_{\text{eff}}} + \frac{m_{\text{eff}}\Omega_0^2}{2}x^2, \tag{2.22}$$

where $p = m_{\text{eff}}\dot{x}$ is the momentum of the mechanical object, and the left and right terms on the right-hand side of equation (2.22) are the kinetic and potential energies respectively [35]. Examining the potential energy, $U(t) = m_{\text{eff}}\Omega_0^2 x^2(t)/2$ for $x(t) = x_q(t)$, we find

$$U(t) = \frac{1}{2}m_{\text{eff}}\Omega_0^2 \bar{x}_{\text{rms}}^2 e^{-\Gamma t}\big(1 + \cos(2\Omega_0 t)\big), \tag{2.23}$$

where we have defined $\bar{x}_{\text{rms}} = \bar{x}/\sqrt{2}$. Typically we are not so concerned with the instantaneous value of the potential energy, and as such we will time-average (low-pass filter) it at a rate slower than Ω_0, yet quicker than Γ, to find

$$\langle U \rangle(t) = \frac{1}{2}m_{\text{eff}}\Omega_0^2 \bar{x}_{\text{rms}}^2 e^{-\Gamma t}. \tag{2.24}$$

We can repeat this exercise for the kinetic energy (taking the $\Gamma/\Omega_0 \ll 1$ limit), after which we find the exact same result for the potential energy, $\langle T \rangle(t) = \langle U \rangle(t)$, such

that the total energy of the mechanical resonator is

$$\langle E \rangle(t) = m_{\text{eff}} \Omega_0^2 \bar{x}_{\text{rms}}^2 e^{-\Gamma t}. \tag{2.25}$$

We see that whereas the amplitude of the mechanical oscillator decays at a rate of $\Gamma/2$, the energy in the mechanical oscillator decays at a rate of Γ.

Using the definition of quality factor introduced for optical resonators in section 2.1.1, and recognizing $W = \langle E \rangle$ and $P_{\text{d}} = -d\langle E \rangle/dt$, we find

$$Q_{\text{mech}} = \frac{\Omega_0}{\Gamma}. \tag{2.26}$$

In contrast to the case of the optical resonator, there is a factor of two difference. This difference is due to the mechanical loss rate, Γ, being given as the full-width half-max of the mechanical resonator, while the optical loss rate κ is the half-width half-max of the optical resonator. These definitions of optical and mechanical loss rates will be used throughout this document.

2.2.2 Effective mass

Throughout this discussion, we have been treating the mechanical resonator as a point-mass with mass m_{eff} located at a position $x(t)$. While this simplification is useful, there is an obvious disconnect with the three-dimensional nanofabricated mechanical objects we are modeling. To bridge this gap we will follow the method of integrating potential energies used by Hauer *et al.* to describe how m_{eff} and the coordinate $x(t)$ correlate to a real-world three-dimensional situation [21].

In the continuum limit, we can use the scalar field $\rho(\vec{r})$ to describe a solid object by describing the density of material throughout all space pointed to by $\vec{r}$. Coupled with the material properties $E(\vec{r})$ (Young's modulus) and $\nu(\vec{r})$ (Poisson's ratio), an eigenvalue problem can be set up to determine the vibrational modes of the solid, each

mode occurring at an angular frequency Ω_0 and with a deformation $\vec{u}(\vec{r})$ indicating the shape of the mode, such that the time dependent displacement of the solid at position $\vec{r}$ nominally follows $\vec{u}(\vec{r}, t) = \vec{u}(\vec{r}) \cos(\Omega_0 t)$.

To relate this vector description to the scalar position coordinate $x(t)$, we will choose a reference position $\vec{r_0}$ and normalize the entire displacement field to it such that we construct the time-dependent vector displacement

$$\vec{x}(\vec{r}, t) = \frac{\vec{u}(\vec{r})}{|\vec{u}(\vec{r_0})|} x(t), \tag{2.27}$$

where $x(t)$ is the mass on a spring position coordinate used throughout this chapter. Thus, if $x(t) = 1$ nm, it means the mechanical resonator, at the location $\vec{r_0}$, has displaced along the unit vector $\vec{u}(\vec{r_0})/|\vec{u}(\vec{r_0})|$ by 1 nm.

To determine the potential energy of the mechanical mode, we can divide the continuum structure into small parts of volume dV such that each part can be reasonable approximated by a mass on a spring oscillating about $\vec{x}(\vec{r})$. Each part then will have potential energy dU given by

$$dU(\vec{r}, t) = \frac{1}{2} \rho(\vec{r}) dV \, \Omega_0^2 \frac{|\vec{u}(\vec{r})|^2}{|\vec{u}(\vec{r_0})|^2} \, x^2(t) \tag{2.28}$$

such that the total potential energy found by integrating over all 3-dimensional space is

$$\begin{aligned} U(t) &= \frac{1}{2} \int_V dV \rho(\vec{r}) \frac{|\vec{u}(\vec{r})|^2}{|\vec{u}(\vec{r_0})|^2} \, \Omega_0^2 x^2(t) \\ &= \frac{1}{2} \, m_{\text{eff}} \, \Omega_0^2 \, x^2(t) \end{aligned} \tag{2.29}$$

where we have defined the effective mass as

$$m_{\text{eff}} = \int_V dV \rho(\vec{r}) \frac{|\vec{u}(\vec{r})|^2}{|\vec{u}(\vec{r_0})|^2}. \tag{2.30}$$

Thus we see that both the position coordinate, $x(t)$, and the effective mass are related and depend upon the choice of reference position $\vec{r_0}$. A common choice of $\vec{r_0}$ is the location where $|\vec{u}(\vec{r_0})|$ is maximized, minimizing the effective mass.

2.2.3 Response to external drive

So far, the motion of a mechanical resonator has been investigated in response to the internal acceleration, damping, and spring forces. To describe the resonator's response to arbitrary external forces we will use the mathematical properties of the Fourier transform to simplify the equations of motion. In response to an external force $F(t)$ acting on the resonator mass, we can write the equation of motion for the mechanical resonator:

$$\ddot{x}(t) + \Gamma\dot{x}(t) + \Omega_0^2 x(t) = \frac{1}{m_{\text{eff}}}F(t). \tag{2.31}$$

To aid in mathematical analysis, we will perform the Fourier transform on x to find its frequency-domain description, $X(\omega) = \mathcal{F}\{x(t)\}$, such that $X(\omega)$ is linearly related to the driving forces $F(\omega) = \mathcal{F}\{F(t)\}$. We find

$$X(\omega) = \frac{F(\omega)}{m_{\text{eff}}[\Omega_0^2 - \omega^2 + i\Gamma\omega]}, \tag{2.32}$$

or simply

$$X(\omega) = \chi_{\text{mech}}(\omega)F(\omega), \tag{2.33}$$

where we have introduced the frequency-dependent mechanical susceptibility

$$\chi_{\text{mech}}(\omega) = \frac{1}{m_{\text{eff}}[\Omega_0^2 - \omega^2 + i\Gamma\omega]}. \tag{2.34}$$

2.2.4 Thermal noise

The generalized equipartition theorem gives the thermal contribution to the energy (E) of a system in contact with a heat bath at temperature T as

$$\left\langle q_i \frac{\partial E}{\partial q_i} \right\rangle = k_B T, \tag{2.35}$$

where q_i is a degree of freedom in the energy and k_B is the Boltzmann constant [36]. Applying this expression to the energy of the mechanical resonator given in equation (2.22) by using the degree of freedom $q_i = x$, we find

$$\langle x_{\text{th}}^2 \rangle = \frac{k_B T}{m_{\text{eff}} \Omega_0^2}. \tag{2.36}$$

That is, the thermal bath in contact with the mechanical resonator drives the mechanics to have a mean-squared displacement given by equation (2.36). We can treat this thermal drive as a random thermal force, $F_{\text{th}}(t)$ acting on the resonator via equation (2.31). However, because the thermal forces are stochastic, we can only describe them by their statistical behavior and cannot explicitly write down the time-series functional form of $F_{\text{th}}(t)$. Instead, we can describe $F_{\text{th}}(t)$ through its autocorrelation function, and in the frequency domain by its spectral density.

Because the thermal forces are random and therefore uncorrelated in time, they can be described by an autocorrelation of $F_{\text{th}}(t)$, $R_F^{\text{th}}(\tau)$, that takes the form

$$R_F^{\text{th}}(\tau) = \frac{S_{\text{th}}}{2} \delta(\tau), \tag{2.37}$$

where S_{th} is a constant and $\delta(\tau)$ is the Dirac delta function. Note that this is valid for the case of damping proportional to velocity, which is the damping model used throughout this thesis, however for alternate damping models the force noise will not be flat in frequency [37].

Using the delta correlated autocorrelation presented in equation (2.37), the single-sided spectral density of $F_{\text{th}}(t)$—twice the Fourier transform of $R_F^{\text{th}}(\tau)$—is then constant across frequencies and equal to

$$S_F^{\text{th}}(\omega) = S_{\text{th}}. \tag{2.38}$$

From equation (2.33), we can relate the single-sided spectral densities of the thermally driven motion and the thermal forces by the mechanical susceptibility,

$$S_x^{\text{th}}(\omega) = S_{\text{th}} \, |\chi_{\text{mech}}(\omega)|^2, \tag{2.39}$$

where $S_x^{\text{th}}(\omega)$ is the spectral density of $x_{\text{th}}(t)$ and $S_F^{\text{th}}(\omega) = S_{\text{th}}$ is the spectral density of $F_{\text{th}}(t)$. This equation can be integrated to relate the mean squared displacement of x to the thermal power S_{th}. To do this we integrate both sides of equation (2.39):

$$\begin{aligned}
\frac{1}{2\pi} \int_0^\infty S_x^{\text{th}}(\omega) d\omega &= \langle x_{\text{th}}^2 \rangle \\
&= \frac{k_B T}{m_{\text{eff}} \Omega_0^2}.
\end{aligned} \tag{2.40}$$

and

$$\frac{S_{\text{th}}}{2\pi} \int_0^\infty |\chi_{\text{mech}}(\omega)|^2 d\omega = \frac{S_{\text{th}}}{4\Omega_0^2 m_{\text{eff}}^2 \Gamma}, \tag{2.41}$$

where the solution to the integral in equation equation (2.41) is given in reference [38]. Equating equations (2.40) and (2.41) and solving for S_{th}, we find

$$S_{\text{th}} = 4k_B T m_{\text{eff}} \Gamma, \tag{2.42}$$

the well-known equation for thermal forces acting on a mechanical resonator. For the use of mechanical resonators as force sensors, S_{th} represents a fundamental limit on

the force sensing ability of a mechanical resonator, which will be further explored in Chapter 3.

2.2.5 Thermomechanical calibration

We can use the thermal forces acting on the cantilever to calibrate the measurement system of mechanical motion in a way that is completely agnostic to the measurement technique. All we require is that the measurement technique operates linearly and is able to resolve the thermomechanical motion of the mechanical device.

For this exercise we will assume the measurement system is outputting a voltage proportional to the mechanical resonator's position, that is

$$v(t) = \alpha_{\mathrm{tm}} x(t), \tag{2.43}$$

where α_{tm} is the gain of the measurement system with units of V/m. The goal of thermomechanical calibration is to determine α_{tm} such that a voltage reading can be converted to a position reading of the mechanical resonator.

To perform the calibration, we will measure the thermomechanical motion of the mechanical resonator and compute the power spectral density of the voltage signal to investigate in the frequency domain. We will assume the measured voltage PSD to be the addition of white noise from the measurement system and the transduced mechanical signal:

$$S_v(\omega) = S_v^{\mathrm{nf}} + \alpha_{\mathrm{tm}}^2 S_x^{\mathrm{th}}(\omega), \tag{2.44}$$

where S_v^{nf} is the voltage noise floor density, which can be approximated as constant across frequency for a small frequency range of measurement. Substituting in the thermal displacement noise from equation (2.39), we get

$$S_v(\omega) = S_v^{\mathrm{nf}} + \alpha_{\mathrm{tm}}^2 S_F^{\mathrm{th}} |\chi_{\mathrm{mech}}(\omega)|^2, \tag{2.45}$$

or more explicitly,

$$S_v(\omega) = S_v^{\text{nf}} + \alpha_{\text{tm}}^2 \frac{4k_{\text{B}}T\Gamma}{m_{\text{eff}}} \frac{1}{(\Omega_0^2 - \omega^2)^2 + \Gamma^2\omega^2}. \tag{2.46}$$

This equation can be fit to the measured voltage PSD of thermomechanical motion to extract the resonator frequency (Ω_0), dissipation (Γ), voltage noise-floor (S_v^{nf}), and combination of $\alpha_{\text{tm}}^2 T/m_{\text{eff}}$. Provided the temperature (T) of the device is known, and the effective mass (m_{eff}) has been determined as described in Section 2.2.2, this fitting procedure provides determination of the measurement gain α_{tm}.

2.3   Theory of optomechanical systems

Now that we have developed a theory for how optical and mechanical resonators both can be modelled independently, we will begin discussing the combination of optical and mechanical resonators together as a coupled optomechanical system. Combining the optical Hamiltonian from equation (2.1) with the mechanical resonator energy from equation (2.22), we find the combined (and still uncoupled) system Hamiltonian

$$H = \hbar\omega_0 \left(\hat{a}^\dagger \hat{a} + \frac{1}{2} \right) + \frac{p^2}{2m_{\text{eff}}} + \frac{m_{\text{eff}}\Omega_0^2}{2}x^2. \tag{2.47}$$

The coupling of mechanical systems to optical systems is expressed as a modification of the optical resonance frequency to depend on the position of the mechanical resonator x:

$$\omega_0 \to \omega_0(x), \tag{2.48}$$

where we are assuming the mechanical oscillator moves much slower than the frequency of the optics such that the optical resonance frequency smoothly follows the mechanical resonators position. Without loss of generality, this dependence on x can

19

be expanded around $x = 0$ to find

$$\omega_0(x) = \omega_0(0) + \left(\frac{\partial}{\partial x}\omega_0(x)\right)x + \left(\frac{1}{2}\frac{\partial^2}{\partial x^2}\omega_0(x)\right)x^2 + ... + \left(\frac{1}{n!}\frac{\partial^n}{\partial x^n}\omega_0(x)\right)x^n. \quad (2.49)$$

We can group these coefficients such that

$$\omega_0(x) = \omega_0(0) - G_1 x - G_2 x^2 - ... - G_n x^n, \quad (2.50)$$

where we call G_n the nth order optomechanical coupling coefficient. Most commonly, the expansion is truncated after the first coefficient and G_1 (or just G) is referred to as the optomechanical coupling coefficient. In Chapter 4 we will further explore the effect of second-order optomechanical coupling using the same basic theory developed here.

Keeping only the linear optomechanical coupling, *i.e.* $\omega_0 \to \omega_0 - G_1 x$, the Hamiltonian in equation (2.47) becomes

$$H_{\text{om}} = \hbar(\omega_0 - G_1 x)\left(\hat{a}^\dagger \hat{a} + \frac{1}{2}\right) + \frac{p^2}{2m} + \frac{m_{\text{eff}}\Omega_0^2}{2}x^2. \quad (2.51)$$

And further retaining only terms that depend on both the optical and mechanical resonator, we can find the interaction Hamiltonian,

$$H_{\text{int}} = -\hbar G_1 x \hat{a}^\dagger \hat{a}. \quad (2.52)$$

Although we won't explore it further, it is worth pointing out that if we express x in terms of its raising and lowering operators, $x = x_{\text{zpf}}(\hat{b}^\dagger + \hat{b})$, where $x_{\text{zpf}} = \sqrt{\hbar/2m_{\text{eff}}\Omega_0}$, the interaction Hamiltonian becomes

$$\begin{aligned} H_{\text{int}} &= \hbar G_1 x_{\text{zpf}}(\hat{b}^\dagger + \hat{b})\hat{a}^\dagger \hat{a} \\ &= \hbar g_0(\hat{b}^\dagger + \hat{b})\hat{a}^\dagger \hat{a}, \end{aligned} \quad (2.53)$$

where we have introduced $g_0 = x_{\text{zpf}} G_1$ as the fist-order optomechanical coupling rate. This rate, expressed in units of Hz—as opposed to G_1, which has units of Hz/m— expresses a more fundamental coupling between single phonons and single photons in the mechanical and optical resonators, and it helps normalize the comparison of optomechanical coupling between mechanical devices which can differ in effective mass and frequency by many orders of magnitude.

2.3.1 Optical transduction in the bad-cavity limit

Here we will develop a theory of the optical transduction of mechanical motion that is mediated via the optomechanical interaction. Rather than perform the standard optomechanical linearization of the interaction Hamiltonian about small fluctuations in the cavity field [39], we will develop an approximation to the optical equations of motion that relies upon the optomechanical device being in the bad cavity limit, where the mechanical resonance frequency is much smaller than the optical loss rate, or $\Omega_0/\kappa \ll 1$. In the devices studied in this thesis, $\Omega_0/2\pi \sim 10^6$ and $\kappa/2\pi \sim 10^9$, such that $\Omega_0/\kappa \sim 10^{-3}$, well within this limit.

To begin, we will restate the optical equations of motion determined in equation (2.7). However, we will do so in the rotating-wave frame of reference, effectively multiplying the entire equation by $e^{i\omega t}$, such that the drive and response both happen at DC ($s(t) \to \bar{s}$). In doing so, we also must change the ω_0 dependency to $\Delta(x) = \omega - \omega_0(x)$, explicitly noting that it is a function of the mechanical resonator position, x, due to the optomechanical coupling. After these transformations we find

$$\dot{a} = -\kappa a + i\Delta(x)a + \sqrt{2\kappa_e}\bar{s}. \tag{2.54}$$

Now, we will make the approximation $\dot{a} = 0$. This approximation is motivated by the fact that since $\bar{s}$ is constant in the rotating frame, the only time-varying driving

21

term in the above equation is $\Delta(x)$. However, we know $\Delta(x)$ changes on a time-scale of $1/\Omega_0$, while the optical resonator will relax into its steady state at a time scale of $1/\kappa$. Due to being in the bad-cavity limit ($\Omega_0/\kappa \ll 1$), we can therefore treat the optical resonator as always being relaxed to its steady state solution. In this case we find

$$a(x) = \frac{\sqrt{2\kappa_e}\bar{s}}{\kappa} \frac{1}{1 - i\delta(x)}, \qquad (2.55)$$

and equivalently for the energy (mean photon number) in the resonator, $n = |a|^2$,

$$|a|^2(x) = \frac{2\kappa_e \bar{s}^2}{\kappa^2} \frac{1}{1 + \delta^2(x)}. \qquad (2.56)$$

In these equations, we have introduced the normalized detuning, $\delta(x) = \Delta(x)/\kappa$, which we can explicitly include first-order optomechanical coupling from equation (2.50) as

$$\delta(x) = \delta_0 + \frac{G_1}{\kappa}x, \qquad (2.57)$$

where $\delta_0 = (\omega - \omega_0)/\kappa$ is the low-frequency normalized detuning due to the drive laser frequency.

We can now linearize $|a|^2(x)$ by treating the optomechanical modulations to $\delta(x)$ as small perturbations. If we define the unitless Lorentzian dependence in equation (2.56) as $c_0(\delta) = (1 + \delta^2)^{-1}$, we can approximate for small modulations u around δ_0:

$$c_0(\delta_0 + u) = \frac{1}{1 + (\delta_0 + u)^2} \qquad (2.58)$$

$$c_0(\delta_0 + u) = c_0(\delta_0) + c_1(\delta_0)u + O(u^2) \qquad (2.59)$$

where

$$c_0(\delta) = \frac{1}{1 + \delta^2}, \tag{2.60}$$

$$c_1(\delta) = -\frac{2\delta}{(1 + \delta^2)^2}, \tag{2.61}$$

$$c_i(\delta) = \frac{1}{i!} \frac{\mathrm{d}^i}{\mathrm{d}\delta^i} c_0(\delta). \tag{2.62}$$

In Chapter 4 we will explore the effect of higher order terms, however for now we will focus on the linear transduction of x. Treating $u = G_1 x/\kappa$ and expanding equation (2.56) for small u, we find the cavity energy dependence on x as

$$|a|^2(x) = \frac{2\kappa_e \bar{s}^2}{\kappa^2}\left(c_0(\delta_0) + \frac{G_1}{\kappa}c_1(\delta_0)x\right), \tag{2.63}$$

where the $c_i(\delta_0)$ are unitless functions of the DC laser detuning, δ_0.

We can substitute the results of equation (2.63) into equation (2.12), the signal detected by direct detection of the transmitted light on a photodetector, to find

$$|z(x)|^2 = \bar{s}^2 - \frac{4\kappa_e\kappa_0\bar{s}^2}{\kappa^2}c_0(\delta_0) - \frac{4\kappa_e\kappa_0\bar{s}^2 G_1}{\kappa^3}c_1(\delta_0)\ x. \tag{2.64}$$

We can see the detected signal exhibits the laser-detuning-dependent, Lorentzian-shaped dip in transmission expected for an optical resonator, but with an additional term proportional to the mechanical resonator's position. We will call this linear dependence on x the optomechanical gain, or

$$\alpha(\delta_0) = \frac{4\kappa_e\kappa_0\bar{s}^2 G_1}{\kappa^3}c_1(\delta_0). \tag{2.65}$$

2.3.2 Extraction of G_1

In Section 2.2.5, we described how to use thermomechanical calibration to find the gain of an arbitrary mechanical measurement system. If the measurement system is a directly detected optomechanical transducer as described in the previous section (which reads optical watts instead of a voltage), the measurement gain determined through thermomechanical calibration is the same as the optomechanical gain given in equation (2.65). Therefore if the optical resonance is characterized such that the optical loss rates κ_e and κ are known, as well as the detuning of the laser during measurement, $\delta = \Delta/\kappa$, the thermomechanically determined gain and equation (2.65) can be equated to extract G_1.

Alternatively, we can express this procedure in slightly more general terms. Going back to assuming a voltage output from our measurement system, thermomechanical calibration will find the displacement-voltage gain, $\alpha_{\mathrm{tm}} = dv/dx$. Examining the optomechanical detection mechanism, the displacement to voltage transduction can be divided into two steps, displacement to optical cavity frequency (ω_0) shifts, and ω_0 to transmission (voltage) transduction. Therefore, with help of the chain rule, $dv/dx = (dv/d\omega_0)(d\omega_0/dx)$. Here $d\omega_0/dx$ is the optomechanical coupling coefficient G_1. By calculating the slope of optical transmission *vs.* laser frequency at the frequency of light used to detect the mechanical signal, $dv/d\omega_0$ can be determined, enabling calculation of G_1.

2.3.3 Optical effects on mechanics

In addition to the mechanical motion affecting the optical field, the optical field also affects the motion of the mechanical resonator. We can find the optomechanical force applied to the mechanical resonator from the optomechanical interaction Hamiltonian

in equation (2.52). The force, $F_{\mathrm{om}} = -\partial H_{\mathrm{int}}/\partial x$, is

$$F_{\mathrm{om}} = \hbar G_1 |a(x)|^2. \tag{2.66}$$

We can use our approximation in equation (2.63) for the cavity energy in the bad-cavity limit, however with one slight addition: we will use the cavity energy based on the mechanical resonator's position delayed in time by some small amount $\tau \sim 1/\kappa$,

$$F_{\mathrm{om}}(t) = \frac{2\hbar\kappa_e G_1 \bar{s}^2}{\kappa^2} c_0(\delta_0) + \frac{2\hbar\kappa_e G_1^2 \bar{s}^2}{\kappa^3} c_1(\delta_0) \; x(t-\tau). \tag{2.67}$$

This optomechanical force contains a DC component—manifesting as a constant offset to the mechanical resonator's position—and the term proportional to the slightly delayed mechanical position. Since we are concerned with the dynamical behavior of the cantilever, we will neglect the constant force (for the devices studied in this thesis this force is on the order of nanonewtons, resulting in static displacements of less than a nanometer), and introduce

$$\beta(\delta_0) = \frac{2\hbar\kappa_e G_1^2 \bar{s}^2}{\kappa^3} c_1(\delta_0) \tag{2.68}$$

as the optomechanically induced force, having units of N/m. We can introduce this optomechanical force into the mechanical equations of motion from equation (2.31) to find

$$\ddot{x}(t) + \Gamma\dot{x}(t) + \Omega^2 x(t) = \frac{\beta(\delta_0)}{m_{\mathrm{eff}}} x(t-\tau) + \frac{F(t)}{m_{\mathrm{eff}}}, \tag{2.69}$$

where $F(t)$ is an additional driving term which will at least include the uncorrelated thermal forces. We will Fourier transform this equation, but first let us inspect the Fourier transform of $x(t-\tau)$. Using properties of the Fourier transform, a time delay

will result in

$$\mathcal{F}\{x(t-\tau)\} = e^{-i\omega\tau}X(\omega) \tag{2.70}$$

$$= \cos(\omega\tau)X(\omega) - i\sin(\omega\tau)X(\omega). \tag{2.71}$$

We can make two approximations. First, since $X(\omega)$ is centered around Ω_0 to a fairly narrow bandwidth of Γ, we will take $\omega \to \Omega_0$. Then, since $\tau \sim 1/\kappa$, small angle approximations to the sine and cosine terms simplify to

$$\mathcal{F}\{x(t-\tau)\} \approx X(\omega) - i\Omega_0\tau X(\omega). \tag{2.72}$$

Thus we can see the effect of adding a small delay of τ to the forcing term: the in-phase component of $X(\Omega)$ remains unchanged, but a small out-of-phase term appears.

With this result we can Fourier transform equation (2.69), collecting all the terms proportional to $X(\omega)$ on the left-hand side, to find

$$\left[\Omega_0^2 - \frac{\beta(\delta_0)}{m_{\text{eff}}} - \omega^2 + i\left(\Gamma + \frac{\Omega_0\tau\beta(\delta_0)}{m_{\text{eff}}}\right)\right]X(\omega) = \frac{F(\omega)}{m_{\text{eff}}}. \tag{2.73}$$

From this equation we can see that the optomechanical back-action terms can be treated as an effective shift in mechanical resonance frequency and damping:

$$\Omega_{\text{eff}}^2 = \Omega_0^2 - \frac{\beta(\delta_0)}{m_{\text{eff}}}, \tag{2.74}$$

or for small perturbations,

$$\Omega_{\text{eff}} = \Omega_0 - \frac{\hbar\kappa_e G_1^2 \bar{s}^2}{m_{\text{eff}}\Omega_0\kappa^3}c_1(\delta_0), \tag{2.75}$$

and

$$\Gamma_{\text{eff}} = \Gamma + \frac{2\hbar\kappa_e G_1^2 \bar{s}^2 \Omega_0\tau}{m_{\text{eff}}\kappa^3}c_1(\delta_0). \tag{2.76}$$

26

In Chapter 4, we will revisit the optomechanical spring effect and include higher-order effects resulting from G_2 optomechanical coupling and further expansions to equation (2.63) to include additional $c_2(\delta)$ dependence.

Chapter 3

Multidimensional optomechanical cantilevers for high frequency force sensing [1]

3.1 Introduction

The atomic force microscope (AFM) [40], has become an indispensable tool for probing the physical characteristics of microscopic systems. Working by Hooke's Law, $F = -kx$, the tip of the AFM (measured at position x) is displaced proportional to an applied force, F, transducing forces into a detectable signal. This effect has been used to great effect for surface imaging, where interatomic forces between an AFM tip and substrate are measured as raster images of the surface structures down to the atomic scale [41] and beyond [42]. The ability to use AFMs in liquid environments [43] has led to their widespread use in biological applications [44], such as live imaging of biological specimens [45], and non-scanning applications like studying receptor-ligand binding of surface proteins [46] and deciphering the mechanics of proteins through

---

[1]This chapter has appeared in "Multidimensional optomechanical cantilevers for high frequency force sensing" [22]

unfolding experiments [47, 48]. For applications such as these where it is desirable to monitor the dynamics of the system with great time resolution, the bandwidth of the measurement process becomes critical.

High-speed AFM, the use of MHz frequency resonators [49], has enabled the dynamics of molecular systems to be visualized at speeds of up to 80 ms for a 50×100 pixel image [50]. This technology has permitted the real-time imaging of individual motor proteins [50], proteins diffusing and interacting in lipid bilayers [51], and the folding of synthetic DNA origami structures [52]. When operated dynamically [53], the maximum time resolution of the measurement is limited by the frequencies of the structural modes of the cantilever. In the simple harmonic approximation, these frequencies are $\Omega_0 = \sqrt{k/m_{\text{eff}}}$, where k and m_{eff} are the spring constant and effective mass of a particular mode, as described in Section 2.2.2 [21]. Therefore AFMs with small masses, or large spring constants, grant access to the regime of large bandwidth and exceptional time resolution through increased mechanical frequencies.

The force sensitivity of a mechanical resonator is limited by the thermal forces acting on the resonator. From the fluctuation-dissipation theorem these forces have spectral densities

$$S_F^{\text{th}} = 4k_B T m_{\text{eff}} \Gamma \tag{3.1}$$

$$= 4k_B T \frac{m_{\text{eff}} \Omega}{Q} \tag{3.2}$$

$$= 4k_B T \frac{k}{\Omega Q}, \tag{3.3}$$

where k_B is the Boltzmann constant, T is the bath temperature, and $Q = \Omega_0/\Gamma$ is the mechanical quality factor [54]. With this equation in mind, the thermal noise on a force sensor can be minimized in two general ways: by reducing the spring constants of the devices, or by reducing the effective masses. Single-crystal silicon cantilevers with low spring constants (10^{-6} N/m) have long since demonstrated aN $\text{Hz}^{-1/2}$ force

sensitivities at cryogenic temperatures [55]. However, the small k results in lowered mechanical frequencies, limiting the time resolution of the measurements. On the other hand, reducing the effective masses of resonators typically increases their mechanical frequencies. Further, small dimensions lessen the effect viscous damping has on the reduction of the mechanical Q [56], and thus reduce thermal forces. Therefore minimizing the dimensions, and m_{eff}, grants access to the regime of both delicate force sensing and exceptional time resolution through increased mechanical frequencies.

Today's nanofabrication tools, in particular electron beam lithography (EBL), allow for the design of mechanical resonators with nanometer dimensions and effective masses of picograms or less. Nanomechanical resonators described by Li *et al.* have demonstrated room temperature force sensitivities of 510 aN Hz$^{-1/2}$ in vacuum and 1300 aN Hz$^{-1/2}$ in air [26]. Using a stressed silicon nitride resonator to provide large mechanical quality factors, Gavartin *et al.* have demonstrated a vacuum room temperature force sensitivity of 74 aN Hz$^{-1/2}$ [54]. Deserving special mention are bottom-up fabricated force sensors using carbon nanotube resonators [57, 58], and silicon nanowires [59], which owing to their tiny effective masses ($\sim 10^{-20}$ kg) have demonstrated unprecedented force sensitivity approaching the zN Hz$^{-1/2}$ level at cryogenic temperatures [58]. Since the original preparation of this chapter, SiN trampoline resonators have demonstrated force noise to below 20 aN Hz$^{-1/2}$ [60], while top-down fabricated graphene resonators have shown force noise to 16 aN Hz$^{-1/2}$ [61].

The force sensing ability of an AFM is dependent on the properties—m_{eff}, Ω_0, Q_{mech} (geometry, material)—of its mechanical resonator. However, to perform measurements with the AFM, a detection method is required to observe the motion of the resonator. While AFMs generally gain better force sensitivity as dimensions are decreased, the task of detecting the displacement of the resonator becomes more challenging. Two common methods to detect the displacement of a cantilever are reflecting a laser beam off the cantilever onto a position sensitive photodetector, termed

optical beam deflection (OBD), or recombining the reflected beam interferometrically. However, as mentioned in Chapter 1, these detection methods scale poorly as the dimensions of the nanomechanical devices fall below the spot size of the laser beam ($\geq$ 1 μm) [62], creating an effective limit on detectable cantilever sizes (and frequencies) that has already been reached by modern nanomechanical resonators.

Cavity optomechanics [63, 64, 32] offers excellent displacement sensitivity while being well suited for nanoscale devices. By spatially localizing optical cavity modes with a mechanical resonator, motional degrees of freedom are coupled to frequency (or phase) shifts of the optical modes. These frequency shifts can be carefully monitored, demonstrated by experiments measuring the imprecision in the motion of nanomechanical resonators to the standard quantum limit (SQL)—the theoretical noise floor of a continuous measurement determined from dynamical back-action and photodetector shot noise [65].

3.2   Results and discussion

Here, three sizes of low mass, MHz frequency, optomechanical devices suited to AFM applications are presented. They consist of cantilever-style nanomechanical resonators coupled to the whispering gallery modes of optical microdisks and are commercially fabricated from a 215 nm thick silicon layer of a silicon-on-insulator (SOI) wafer, ensuring simple fabrication with automatic and reproducible optomechanical cavity formation. For fabrication details see Appendix A.1. The cantilevers have lengths of 8, 4, and 2 μm, and are on average 400 nm wide, broadening towards the end to allow functionalization without compromising the optical cavity quality ($Q_{\mathrm{opt}} \sim 3 \times 10^4$ for 20 μm diameter disk). They couple to disks of 20, 10 and 5 μm diameter, respectively. Scanning electron microscopy (SEM) images and finite element method (FEM) simulations of the first three structural modes of the 8 μm long cantilever are
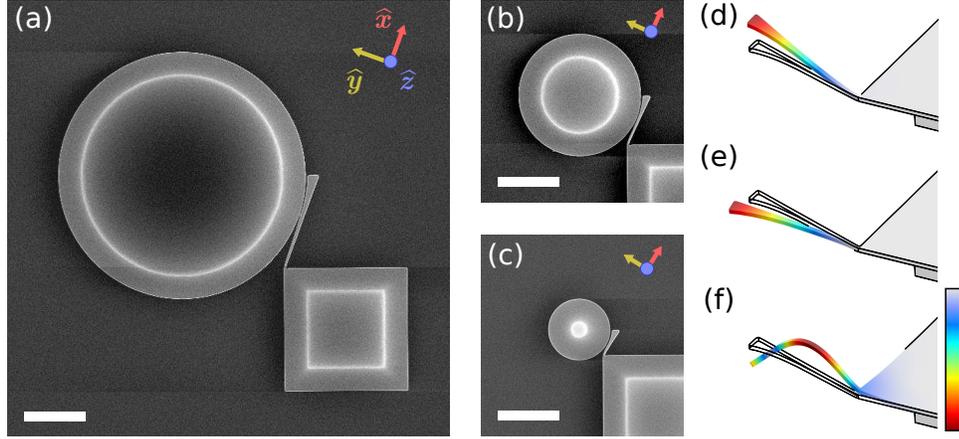
Figure 3.1: (a) SEM image of the optomechanical device with a 20 μm diameter optical microdisk evanescently coupled to an 8 μm long cantilever. Coordinates are aligned such that $\hat{x}$ is parallel to the axis of the cantilever, $\hat{y}$ points along in-plane motion of the cantilever, and $\hat{z}$ points out-of-plane. (b) 10 μm disk, 4 μm cantilever and (c) 5 μm disk, 2 μm cantilever; scale bars 5 μm on all panels. (d)-(f) FEM simulations reveal the first three modes of the 8 μm long cantilever as an example: an out-of-plane mode, an in-plane mode and a second out-of-plane mode. Mechanical modes of the shorter cantilevers are similar. Color scale indicates relative displacement.

shown in Figure 3.1. Devices are measured both in vacuum (10^{-5} torr) and air to investigate force sensitivities in different environments. We envision single-molecule force (folding/unfolding) experiments as the ideal AFM application for these devices, as this would not degrade the optical Q of micro disk due to a sample, nor would a separate tip need to be attached.

To measure the motion of our device's cantilever, single-mode light from a tunable diode laser (New Focus TLB-6330, 1550-1630 nm) is passed through a dimpled, tapered optical fiber [66] placed on the top edge of the optical microdisk opposite to the mechanical device using three-axis nanopositioning stages (Figure 3.2b). By slightly detuning the laser from an optical resonance of the disk, modulations in the frequency of the optical modes induced by the movement of the mechanical resonator are transduced to a voltage signal from a photodetector (PD) measuring the transmission through the tapered fiber. A lock-in amplifier (Zurich H2FLI) is used to measure the high-frequency spectral density of the PD voltage (S_V), which is then thermome-
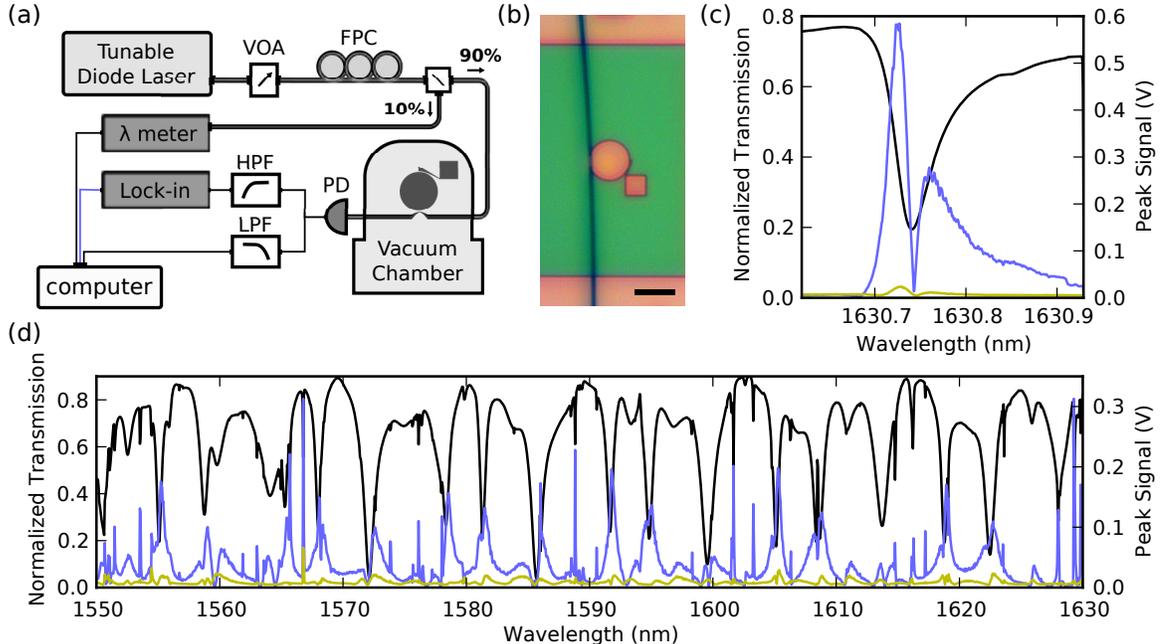
Figure 3.2: (a) Schematic of experimental setup (VOA - variable optical attenuator, FPC - fiber polarization controller, HPF - high pass filter, LPF - low pass filter, PD - photodiode). (b) Optical image of a dimpled, tapered fiber placed on a 10 μm diameter disk opposite an 8 μm long cantilever; scale bar 20 μm. (c) Transmission (normalized to transmission in the absence of coupling) through the tapered fiber (black), while simultaneously locked-on to the out-of-plane mode (light blue) and the in-plane mode (yellow), reveals the maximum peak signal occurs slightly detuned from the optical resonance, approximately corresponding to the maximum slope of the transmission [33]. (d) Scanning the entire frequency range of the tunable laser reveals optical resonances that provide maximum signal.

chanically calibrated to displacements of the cantilever's tip using m_{eff} determined from FEM simulations [21].

In all cases, peaks in the voltage spectral density corresponding to thermodynamic actuation of the fundamental out-of-plane mode were visible, but when measured in vacuum the in-plane modes, and the second out-of-plane mode of the 8 μm cantilever (Figure 3.1f), were additionally visible. Actuation using a broadband longitudinal piezo buzzer revealed that the lowest-frequency mode was more efficiently actuated, resulting in its identification as the out-of-plane mode. However, as piezo buzzers will shake the entire mechanical system, potentially activating orthogonally moving modes, we cannot be completely sure of mode identification.

When calculating the effective mass of the cantilevers through FEM simulation, dimensions where extracted from SEM images of the cantilevers. For the most critical dimensions—the thinnest widths of the cantilevers—we estimate maximum errors in dimension of 30%. When comparing frequencies estimated from FEM simulations to frequencies of the measured modes, we find less an average error of 28%. From this we can limit the error in effective mass, and therefore the displacement noise floor and force noise sensitivity, to 30%.

With this estimation of error in mind, displacement noise floors of 2.0 ± 0.6 fm Hz$^{-1/2}$ were observed for the out-of-plane motion of the 4 μm cantilever, equivalent to the best noise floors observed using traditional AFM detection methods [30, 31], yet for these radically smaller, lighter, and higher-frequency cantilevers.

The small displacement noise floors achieved with these devices are a result of the efficiency with which displacements of the cantilever are transduced into frequency changes in the optical disk, coupled with the narrow line-widths of the optical resonances. This efficiency can be described to first order by the optomechanical coupling coefficient, $G_1 = d\omega_0/dz$, where ω_0 is the optical cavity frequency. The small gap between the cantilever and the optical microdisk (≈ 130 nm) enables good optomechanical coupling. In addition, the cantilevers curve with the microdisk to optimize G_1 by increasing overlap between the optical whispering gallery modes and the cantilever's motion (Table 3.1). In all devices, the out-of-plane motion of the cantilever had considerably better optomechanical coupling than the in-plane motion, resulting in the difference in displacement noise floors between Figures 3.3a and 3.3c, the spectral densities of the 8 μm cantilever's two first modes. The apparent symmetry of the out-of-plane motion might suggest a small linear optomechanical coupling for the out-of-plane mode, however slanted sidewalls of the devices due to fabrication (Figures 3.4a, 3.4b), the placement of the dimpled fiber touching the top

34
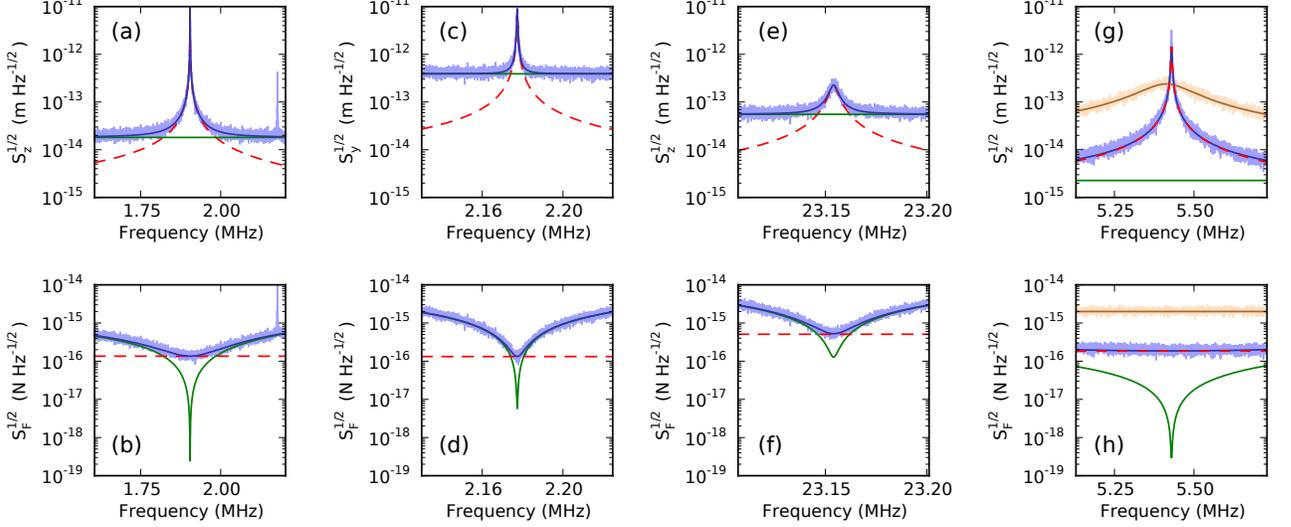
Figure 3.3: (a) A peak in the displacement noise density, $\sqrt{S_z}$, corresponding to out-of-plane motion of the 8 μm cantilever. The peak at higher frequency is the in-plane mode. $\sqrt{S_z}$ is fit to a superposition (blue) of the thermal noise of the cantilever ($\sqrt{S_z^{\text{th}}}$, red dashed) and a constant measurement noise, the displacement noise floor ($\sqrt{S_z^{\text{nf}}}$, green). (b) By dividing $\sqrt{S_z}$ by the force susceptibility, $|\chi(\omega)|$, the measured force noise density, $\sqrt{S_F}$, can be obtained. (c) $\sqrt{S_y}$ and (d) $\sqrt{S_F}$, corresponding to the 8 μm cantilever's in-plane plane mode, and (e), (f) second out-of-plane mode. In all cases $\sqrt{S_F}$ is limited by thermal forces when at the cantilever resonance frequency and limited by detector noise off-resonance. (g) $\sqrt{S_z}$, and (h) $\sqrt{S_F}$ of the 4 μm device's out-of-plane mode are dominated by thermal noise across a wide frequency range due to the low optomechanical detection noise floor. Shown in light brown are $\sqrt{S_z}$ and $\sqrt{S_F}$ in air, with corresponding fits in dark brown. $\sqrt{S_z^{\text{nf}}}$ in air agrees with that in vacuum, but $\sqrt{S_F^{\text{th}}}$ is limited to 2 fN Hz$^{-1/2}$ due to the viscous damping, compared with 180 aN Hz$^{-1/2}$.

of the optical disk introduce sufficient asymmetries, or even incorrect identification of mechanical modes explain the large linear optomechanical coupling observed [33].

The linear susceptibility, $\chi(\omega) = z(\omega)/F(\omega)$, relates displacements of the cantilever's tip, $z(\omega)$, to applied forces, $F(\omega)$. By dividing the measured displacement spectral density by $|\chi(\omega)|^2$, the observed force spectral density can be found (Figure 3.3b, d, f, and h). The thermal forces on the cantilever impose a minimum force sensitivity, and in all cases in which the thermomechanical motion of the cantilever was detected, the total force noise reached a minimum at the cantilever resonant frequency equal to the thermal noise, S_F^{th}. In vacuum, both the in-plane and out-of-

35
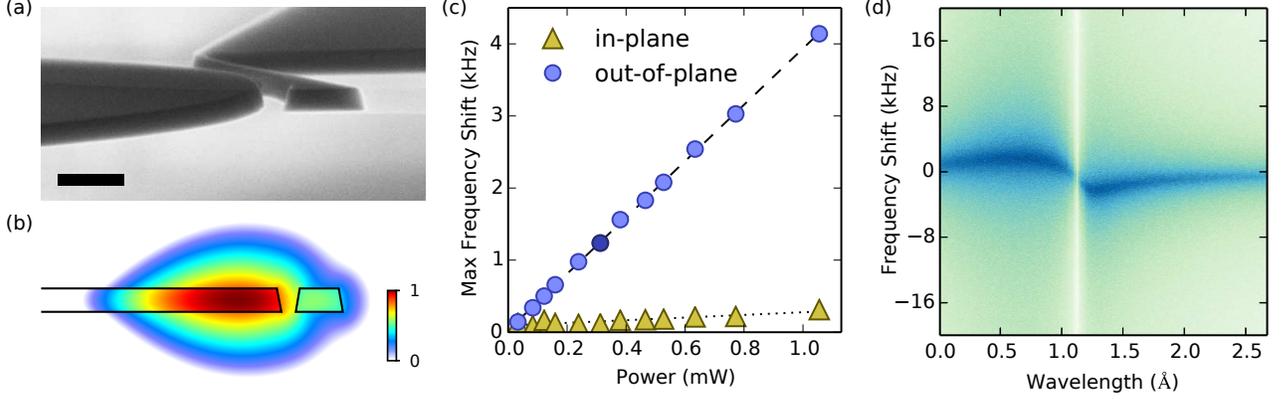
Figure 3.4: (a) Tilted SEM image of a device with a 4 μm cantilever; scale bar 500 nm. Side walls have a slope of approximately 10° from vertical, creating asymmetries in the optomechanical coupling. (b) FEM simulation of an optical mode in cylindrically symmetric coordinates. Color bar indicates the relative log magnitude of the electric field. (c) The blue-detuned laser power going into the tapered fiber to detect the 4 μm device causes stiffening of the cantilever. The frequency of the out-of-plane motion increased by $\sim 0.1\%$, while the in-plane motion showed negligible effect due to its $\sim 100\times$ smaller G_1, Table 3.1. Errors in Power and Frequency shift are similar to the marker size. The optomechanically induced frequency shift of the cantilever is dependent on the wavelength of light used to detect the device's motion and the maximum positive frequency shift is plotted. (d) An example measurement of the voltage spectral density measured as the laser is scanned towards larger wavelengths. Darker colors indicate larger spectral density (log scaled). The darkened data point in (c) corresponds to the data shown in (d).

plane modes of the 8 μm cantilever, exhibited the best observed force sensitivity of 130 ± 40 aN Hz$^{-1/2}$, Figures 3.3b, 3.3d. However in air, the situation was reversed and the 2 μm cantilever presented best force sensitivity of 1500 aN Hz$^{-1/2}$.

While the devices presented here don't set a record for any individual metric, we believe they provide an excellent candidate for carrying out force measurements in certain regimes, namely the sensitive measurement of forces at room temperature and atmospheric pressures. The smallest ($m_{\text{eff}} = 50$ ag) piezoresistively detected nanomechanical resonator of Li *et al.* [26] achieves a force sensitivity of 1300 aN Hz$^{-1/2}$, not much smaller then the 1500 aN Hz$^{-1/2}$ achieved with our smallest device, but with slightly less displacement resolution (39 fm Hz$^{-1/2}$) than with our optomechanical detection mechanism (18 fm Hz$^{-1/2}$). Alternatively, the in-air, optomechanically de-

tected, doubly clamped beam geometry of Srinivasan *et al.* [67] and Liu *et al.* [68] achieve 10x better displacement noise floors, but fall short on force sensitivity (4400 aN Hz$^{-1/2}$ vs. 1500 aN Hz$^{-1/2}$).

Optomechanically detected silicon nitride resonators represent the best micromachined (*i.e.* not grown like carbon nanotubes [58] or silicon nanowires [59]) room-temperature force-sensors reported in the literature [54, 60, 69, 70]. However, these devices gain their force sensing ability from the high intrinsic (*i.e.* in vacuum) quality factors of high-stress silicon nitride strings [56]. Since viscous dissipation mechanisms present in air would likely dominate over the intrinsic vacuum dissipation mechanisms, we imagine that at atmospheric pressure nanostrings would lose their quality factor advantage, and because of the much larger m_{eff} of the strings (9 pg) versus the devices presented here (0.14 pg), our devices may well achieve better force sensitivity. Further, all three of the above compared force sensors were fabricated using electron beam lithography. Devices presented in this chapter were fabricated at a commercial foundry (IMEC) using deep UV lithography, a process much better suited to the commercial fabrication of many such devices. We imagine EBL could be used to produce optomechanically detected cantilevers similar to those presented here, but with m_{eff} similar to those presented by Li *et al.*, providing equivalent force sensitivities, but with possibly better displacement noise floors.

While S_F^{th} was reached regardless of detector noise, low displacement noise floors broadened the frequency range over which thermally limited force noise was observed (*e.g.* Figure 3.3b vs. 3.3h). Therefore small displacement noise floors, while not reducing the minimum force sensitivity, allow for larger bandwidth (faster) force measurements.

Operating an AFM at low bath temperatures would reduce thermal noise on the cantilevers, as described by the fluctuation-dissipation theorem. Accordingly, the best force sensitivities have been reached on devices at cryogenic temperatures. Assuming

Cantilever Length	m_{eff}	k	$\Omega_0/2\pi$	Q (air)	$\sqrt{S_{z,y}^{\text{nf}}}$ (air)	$\sqrt{S_F^{\text{th}}}$ (air)	G_1
[μm]	[fg]	[N/m]	[MHz]		[fm Hz$^{-1/2}$]	[aN Hz$^{-1/2}$]	[MHz / nm]
2 out-of-plane	140	2.2	20.1	3,600 (120)	20 (18)	290 (1,500)	2,000
2 in-plane	180	3.3	21.4	5,000	120	280	340
4 out-of-plane	240	0.30	5.43	4,300 (35)	2 (3)	180 (2,000)	720
4 in-plane	260	0.48	7.04	4,400	300	200	6
8 out-of-plane	610	0.087	1.90	6,500 (22)	18 (17)	135 (2,300)	150
8 in-plane	610	0.11	2.18	7,800	390	132	7
8 2$^{\text{nd}}$ out-of-plane	610	13	23.2	5,600	55	510	57

Table 3.1: Measured parameters of investigated devices. Data is presented for three optomechanical devices of varying size, but similar geometry (Figure 3.1), with cantilevers approximately 2, 4, and 8 μm long. For each device at least two different mechanical modes were detected. Effective masses (m_{eff}) for each mode were computed from dimensions measured with SEM, using FEM to determine the mode shape [21]. Peaks were thermomechanically calibrated to extract Ω_0, the cantilever's resonance frequency, Q, the mechanical quality factor in vacuum, and S_z^{nf}, the displacement noise floor. From these parameters we compute k, the mode's spring constant, and S_F^{th}, the spectral density of thermal forces on the cantilever imposing a force sensing limit. When measured in air, the quality factors of the cantilevers were reduced by viscous damping and only the out-of plane motion could be detected thermomechanically. Smaller cantilevers exhibited the larger quality factors in air, and smaller thermal forces, resulting in better force sensing ability—opposite to the case in vacuum.

device parameters (m_{eff}, Ω, Q_{vac}) remain constant across temperatures, a thermal force noise of 3 aN Hz$^{-1/2}$ at 100 mK is expected to be detectable above the room temperature displacement noise floors of the 8 μm cantilever's out-of-plane motion. This is comparable with the 0.5 aN Hz$^{-1/2}$ force sensitivity detectable by a conceptually similar superconducting microwave resonator [20], or the 0.8 aN Hz$^{-1/2}$ sensitivity of kHz frequency cantilevers used for magnetic resonance force microscopy (MRFM) [55]. Thus we propose optomechanically detected nanomechanical resonators are also good candidates for low-temperature, high-frequency, precision force measurements.

While the optomechanical coupling allows readout of the cantilever's position by monitoring the optical resonator, the optical resonator provides radiation pressure back-action on the mechanical device affecting its dynamics. Because the time scale of optical cavity relaxation is much quicker than the mechanical response time $\tau \sim 2\pi/\Omega$

(*i.e.* quite unresolved sideband regime), the radiation pressure forces provide only an optical spring effect, allowing the tuning of k to within $\sim 0.1\%$ (Figure 3.4c), as opposed to any optomechanical heating or cooling [71].

3.3   Conclusion

Optomechanical AFMs provide the path to ultra-sensitive molecular force probe spectroscopy, HS-AFM, and other AFM applications. By comparing three different sized force sensing devices, we have demonstrated a trade off in force sensing ability between low spring constant and low effective mass devices depending on the application of interest: the larger, low spring constant device provided best force sensing in vacuum, but the smaller devices excelled in a viscous environment. We have demonstrated optomechanical detection of sub-picogram effective mass multidimensional AFM cantilevers that are commercially fabricated, with displacement noise floors down to $2.0 \pm 0.6 \, \mathrm{fm\,Hz^{-1/2}}$, and $130 \pm 40 \, \mathrm{aN\,Hz^{-1/2}}$ force sensitivity in vacuum at room temperature. Challenges remain, including selective attachment of relevant molecules, yet we envision that extension of the devices presented here to aqueous environments will open new doors in high-speed, high-resolution molecular force measurements.

Chapter 4

Nonlinear optomechanics in the stationary regime [1]

4.1 Introduction

Cavity optomechanics has resulted in new levels of extremely precise displacement transduction of nanomechanical resonators [73, 64, 74]. This precision has reawakened interest in exploring the quantum limits of measurements of mechanical harmonic oscillators [75, 76, 77], first discussed in the context of gravitational-wave antennas [78, 79, 80]. Recent quantum measurements of cavity optomechanical resonators include dynamical back-action cooling to their quantum ground state [81, 82], quantum state preparation and read-out [83], observation of motional sideband asymmetry [84, 85], and entanglement of an itinerant photon with a cavity phonon [86].

One of the most fundamental, and as of yet unattained, quantum measurements of a nanomechanical resonator that could be performed is that of the quantized energy eigenstates (as has been demonstrated with an electron in a cyclotron orbit [87]). To achieve this measurement, one cannot measure the displacement of the resonator,

---

[1]This chapter has appeared in "Nonlinear optomechanics in the stationary regime" [72]

but instead must measure the energy directly – without affecting subsequent measurements of the energy – a so-called quantum non-demolition (QND) measurement [19]. QND measurement of phonon number has applications in thermometry [87], preparation and readout of states for quantum information processing, and macroscopic studies of quantum decoherence [88, 89].

The accuracy in continuously measuring two conjugate quantities is limited by the Heisenberg uncertainty principle to the standard quantum limit (SQL) [19, 90]. However, performing a measurement on only one conjugate observable that commutes with itself at later times imposes no such limit on measurement precision [18, 91, 92, 93, 94]. In the case of a harmonic oscillator, position and momentum do not commute with themselves at all later points in time and continuous measurements are therefore limited to the SQL, however resonator energy and the real or imaginary part of the complex amplitude are QND compatible observables at all times [18, 19].

Here our interest lies in continuous QND measurement of the energy, or the number of phonons, in a mechanical resonator [95]. In an optomechanical system, this measurement is expected to be possible by having strong second-order optomechanical coupling in the interaction Hamiltonian [96, 97, 98, 99]. Second-order coupling has been demonstrated in membrane-in-the-middle Fabry-Pérot cavities [100, 101, 102], however it has been pointed out there remains first order coupling between the two optical modes, possibly preventing QND measurements [103]. Exceptionally strong second-order coupling has been observed in a double disk optomechanical system [104]. Since the original preparation of this work, nonlinear optomechanical coupling has been observed in optomechanical "paddle" resonators [105], tunable optomechanical photonic crystal cavities [106] and levitated nanoparticles [107].

Signal from second-order optomechanical coupling, hence measurement of x^2, will display mechanical peaks at twice the fundamental frequency. However, we would also expect that nonlinear transduction of the displacement of a mechanical resonator from

a nonlinear optical transfer function would also appear at harmonics of the mechanical resonance frequency, as has been observed [108, 109, 110].

In this chapter, we report observation of peaks in the mechanical power spectra at exactly twice the fundamental mechanical frequency, as shown in Figure 4.1. We derive a model for the origin of the harmonic signal, as well as the optical spring effect, from both linear and quadratic optomechanical couplings as a function of laser detuning from the cavity resonance. We develop a framework for understanding non-linear optomechanical transduction mechanisms by using the detuning dependance of the linear and quadratic mechanical signals.

Using this framework, we are thus able to determine the coupling contributions to the nonlinear optical transfer function and find second-order optomechanical coupling of $\sim$MHz/nm^2, comparable to initial membrane-in-the-middle systems [100], although second-order coupling up to GHz/nm^2 has since been observed [101].

4.2   The optomechanical system

The optomechanical cavity being measured is a nanocantilever with effective mass $m = 240$ fg and frequency $\Omega_0/2\pi = 6$ MHz, as described in Chapter 3, fabricated on-chip to be in the evanescent field of an optical microdisk. The Hamiltonian for independent optical and mechanical cavities can be written $\hat{H} = \hat{H}_{\mathrm{opt}} + \hat{H}_{\mathrm{m}}$, where $\hat{H}_{\mathrm{opt}} = \hbar\omega_0\left(\hat{a}^\dagger\hat{a} + 1/2\right)$ and $\hat{H}_{\mathrm{m}} = \hbar\Omega_0\left(\hat{b}^\dagger\hat{b} + 1/2\right)$ are the Hamiltonians of the optical and mechanical resonators. Here we denote ω_0 and Ω_0 as the optical and mechanical cavity resonance frequencies, and $\hat{a}^\dagger$ $(\hat{b}^\dagger)$ and $\hat{a}$ $(\hat{b})$ are the creation and annihilation operators for photons (phonons). We note that since we will be extending our discussion to the classical regime where the number of quanta in the resonator is large, we will ignore the ground state contribution to the resonators' energies.

Being within the optical mode volume, the mechanical resonator's motion is coupled to the optical cavity resonance frequency through shifts in the effective index of refraction. As described in Section 2.3, this coupling can be described to second order as

$$\omega_0 \rightarrow \omega_0 - G_1 \hat{x} - G_2 \hat{x}^2, \tag{4.1}$$

where $G_1 = -\partial \omega_0 / \partial x$ and $G_2 = -(1/2)\partial^2 \omega_0 / \partial x^2$ are the first and second-order optomechanical coupling constants. Therefore,

$$\hat{H}_{\text{int}} = -\hbar \left(G_1 \hat{x} + G_2 \hat{x}^2 \right) \hat{a}^\dagger \hat{a} \tag{4.2}$$

is the interaction Hamiltonian to second-order. For a device with symmetric out-of-plane motion in a symmetric evanescent optical field, one anticipates second-order optomechanical coupling, with first order coupling arising from asymmetries in the motion or optical field [22].

4.3 Optical transduction

We measure the optical transmission through a tapered optical fiber coupled to the optical resonator, Figure 4.1b, in the "tuned-to-slope" regime. As such, the classical field in an optical cavity, $a = \langle \hat{a} \rangle$, coupled to one input waveguide carrying field $\bar{s}e^{-i\omega t}$ and one output waveguide carrying away field z, when written in a frame rotating at the source frequency ω, can be modeled with equation (2.54) as

$$\dot{a} = -\kappa a + i\Delta a + \sqrt{2\kappa_{\text{e}}}\,\bar{s}, \tag{4.3}$$

where a is normalized such that $a^*a = \langle \hat{n} \rangle = n$ is the number of photons in the cavity, $\kappa = \kappa_0 + \kappa_{\text{e}}$ describes the total loss rate from the optical resonator both to the output waveguide (κ_{e}) and elsewhere (κ_0) [39], $\Delta = \omega - \omega_0$ is the detuning of the source
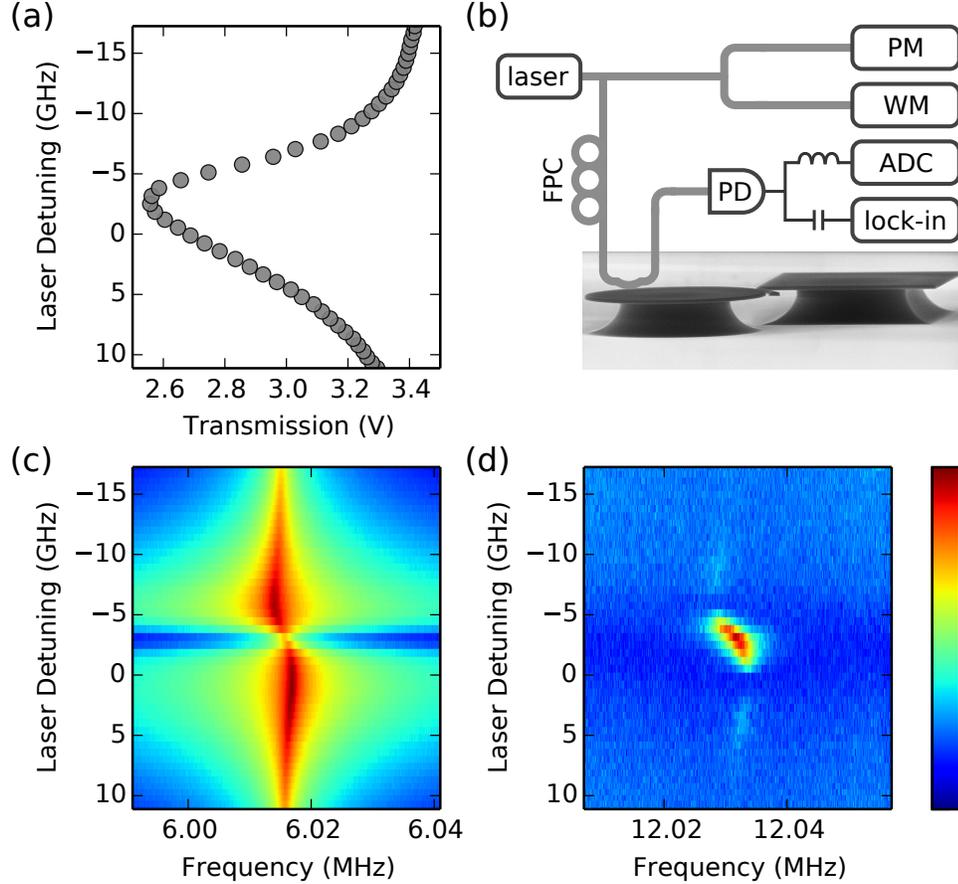
Figure 4.1: (a) The low frequency transmission (< 1 kHz) through the optical cavity reveals the optical resonance as a tunable laser is scanned over the optical resonance frequency. The line-shape is distorted due to nonlinear frequency shifts of the optical resonance as described in the text. (b) A schematic of the experiment above a tilted scanning electron microscope (SEM) image of the optomechanical device being measured. PM - power meter, WM - wavelength meter, ADC - low frequency analog-to-digital converter. PD - photodetector, FPC - fiber polarization controller. Scale bar 5 μm. Transmission power spectral densities normalized to maximum signal around (c) 1Ω and (d) 2Ω. Frequency doubling indicates nonlinear transduction. Log-scaled color bar spans from the minimum noise floor (10^0 in both) up to (c) $10^{5.4}$ and (d) 10^1.

laser frequency (ω) from the cavity frequency (ω_0), and $\bar{s}^2$ is the incoming power in photons per second. Remember that we have defined κ as the half width at half max of the optical power resonance, such that the cavity energy rings down as $e^{-2\kappa t}$.

We restrict our analysis to the bad-cavity limit, or sideband unresolved regime where $\kappa \gg \Omega_0$ (for the device presented here $\kappa/\Omega_0 \approx 10^3$), hence the optical fields in the cavity reach steady state in a characteristic time $\tau_{\mathrm{opt}} = 1/\kappa$ much faster than the time scale of the mechanical motion ($\tau_{\mathrm{m}} = 1/\Omega_0$) [111, 112]. Following the approximation made in Section 2.3.1 in which we set $\dot{a} = 0$, we find the number of cavity photons, $n = |a|^2$, as

$$n = \frac{2\kappa_e \bar{s}^2}{\kappa^2} \frac{1}{1+\delta^2}, \tag{4.4}$$

where $\delta = \Delta/\kappa$ is the normalized laser detuning from the cavity resonance in units of κ.

Again, as done in Chapter 2, we will Taylor expand the Lorentzian detuning dependence of n, $c_0(\delta) = (1+\delta^2)^{-1}$, for small perturbations u around δ, except this time keeping terms up to u^2. We find

$$c_0(\delta) = \frac{1}{1+\delta^2}, \tag{4.5}$$

$$c_1(\delta) = -\frac{2\delta}{(1+\delta^2)^2}, \tag{4.6}$$

$$c_2(\delta) = \frac{3\delta^2 - 1}{(1+\delta^2)^3}, \tag{4.7}$$

$$c_i(\delta) = \frac{1}{i!} \frac{\mathrm{d}^i}{\mathrm{d}\delta^i} c_0(\delta), \tag{4.8}$$

plotted in Figure 4.2a, such that

$$n(\delta + u) \approx n_{\mathrm{max}}[c_0(\delta) + c_1(\delta)u + c_2(\delta)u^2], \tag{4.9}$$
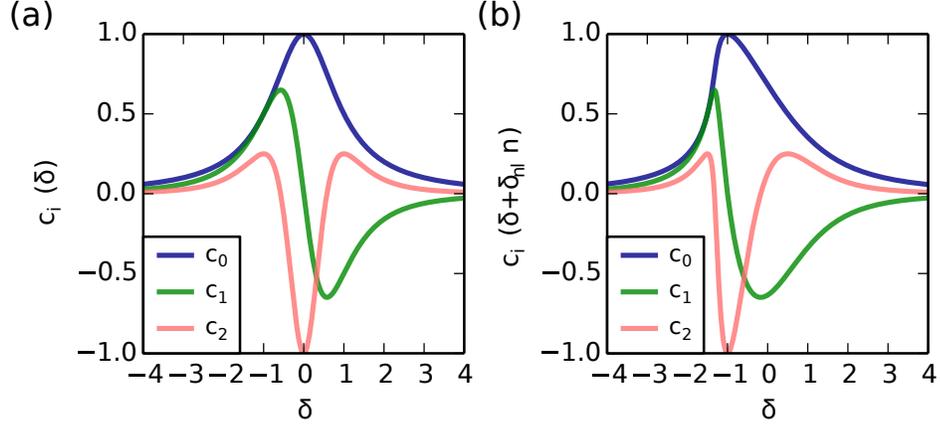
Figure 4.2: (a) The c_i coefficients are unitless, normalized functions which describe the detuning dependence of the various optomechanical parameters. By comparing the observed detuning dependence of mechanical spectra with the shape of these c_i's, the origin of the effects can be determined. (b) Nonlinear effects due to large optical power in the resonances create asymmetries in the detuning dependence. By adding an additional power dependent detuning these nonlinear effects can be accurately modeled [113], as described in the text.

where $n_{max} = 2\kappa_e \bar{s}^2/\kappa^2$. Explicitly substituting the coupling of the mechanical motion to the cavity detuning, as given by (4.1),

$$\delta \to \delta + \frac{G_1}{\kappa}x + \frac{G_2}{\kappa}x^2, \tag{4.10}$$

and $G_1 x/\kappa + G_2 x^2/\kappa$ as u (keeping terms to second-order in x) we find

$$n \approx \frac{2\kappa_e \bar{s}^2}{\kappa^2}\left[c_0 + c_1\frac{G_1}{\kappa}x + \left(c_1\frac{G_2}{\kappa} + c_2\frac{G_1^2}{\kappa^2}\right)x^2\right], \tag{4.11}$$

remembering c_i are implicit functions of detuning. Substituting this approximation for $n = |a|^2$ into equation (2.12), the signal detectable on a photodetector is

$$Z \approx \bar{s}^2 - \frac{4\kappa_e \kappa_0 \bar{s}^2}{\kappa^2}\left[c_0 + c_1\frac{G_1}{\kappa}x + \left(c_1\frac{G_2}{\kappa} + c_2\frac{G_1^2}{\kappa^2}\right)x^2\right]. \tag{4.12}$$

Equation (4.12) is the time-series representation of the optical transfer function up to order x^2, with three parts: one DC, one oscillating at 1Ω, and one oscillating at 2Ω. This behavior can be seen by noting the DC dependence is simply

$$Z_{DC} = \bar{s}^2 - \frac{4\kappa_e\kappa_0\bar{s}^2}{\kappa^2}c_0. \tag{4.13}$$

This equation describes the optical resonance as a function of detuning, as seen in Figure 4.1a which includes nonlinear effects distorting the symmetry of the resonance that will be further discussed in Section 4.5. Fourier transforming equation (4.12) to linear x and neglecting DC components, we find

$$Z_{1\Omega}(\Omega) = -4\bar{s}^2\frac{\kappa_e\kappa_0}{\kappa^2}\frac{G_1}{\kappa}c_1 x(\Omega), \tag{4.14}$$

such that $-4\bar{s}^2\kappa_e\kappa_0 G_1 c_1/\kappa^3$ is the linear, time-invariant part of the optical transfer function—*i.e.* the optomechanical gain given in equation (2.65). Equation (4.14) describes a typical optomechanical transduction of mechanical signal, as seen in Figure 4.1c.

The remaining nonlinear terms arise from the x^2 dependence:

$$Z_{2\Omega}(t) = -\frac{4\kappa_e\kappa_0\bar{s}^2}{\kappa^2}\left(c_1\frac{G_2}{\kappa} + c_2\frac{G_1^2}{\kappa^2}\right)x^2(t). \tag{4.15}$$

Examining $x(t)$ for the case of sinusoidal motion (*i.e.* taking $\Gamma \to 0$ such that there is no damping) demonstrates the quadratic nature of the spectra: $x^2(t) \approx x_0^2\cos^2\Omega t = x_0^2/2\,(1 + \cos 2\Omega t)$, mixing the x^2 signal to $\Omega + \Omega$ and $\Omega - \Omega$ (DC). Here we neglect the DC signal from the nonlinear transduction, as it will be much smaller than the DC signal from the optical resonance. These three parts of the optomechanical transduction will be fit to the experimental data to determine the linear and nonlinear optomechanical couplings, G_1 and G_2.

4.4   Mechanical back-action

While the optical cavity is interacting with the motion of the mechanical resonator, radiation-pressure forces provide back action on the resonator's momentum. These forces can be found classically from the interaction Hamiltonian,

$$F = -\frac{\partial}{\partial x} H_{\text{int}} = \hbar G_1 n + 2\hbar G_2 n\, x, \tag{4.16}$$

equivalent to the forcing term found in equation (2.66) but including an additional G_2 term. Substituting in our perturbation for n from equation (4.11) and putting these forces into the equations of motion for a thermally driven damped harmonic oscillator while retaining only force components up to linear in x, we find

$$
\begin{aligned}
m\ddot{x} + m\Gamma\dot{x} \quad + \quad & m\Omega_0^2 x = F_{\text{th}} + \hbar n_{\max} G_1 c_0 \\
+ \quad & \frac{2\hbar\kappa_e \bar{s}^2}{\kappa}\left(\frac{G_1^2}{\kappa^2}c_1 + 2\frac{G_2}{\kappa}c_0\right) x,
\end{aligned}
\tag{4.17}
$$

where Γ is the mechanical damping rate and F_{th} represents uncorrelated thermal forces actuating the resonator. Collecting terms proportional to x, we see the radiation pressure-forces shift the effective oscillating frequency of the resonator, Ω_{eff}:

$$m\Omega_{\text{eff}}^2 = m\Omega_0^2 - \frac{2\hbar\kappa_e \bar{s}^2}{\kappa}\left(\frac{G_1^2}{\kappa^2}c_1 + 2\frac{G_2}{\kappa}c_0\right), \tag{4.18}$$

or

$$\Omega_{\text{eff}} - \Omega_0 \approx -\frac{\hbar\kappa_e \bar{s}^2}{m\Omega_0\kappa}\left(\frac{G_1^2}{\kappa^2}c_1 + 2\frac{G_2}{\kappa}c_0\right). \tag{4.19}$$

Importantly, this optomechanical spring effect has dependence on both G_1 and G_2 – similar to the optomechanical transduction – yet has different dependence on detuning, δ, providing a complementary determination of G_1 and G_2 (Figure 4.1c and Figure 4.3d).

4.5 Nonlinear effects on the optical resonator

The displacement transduction and optical spring equations given so far have detuning dependence derived from the c_i functions defined above, equations (4.5)–(4.8), which have symmetric (c_0, c_2) or antisymmetric (c_1) dependence on laser detuning. However, the observed detuning dependencies (Figure 4.1a, c, d) are stretched towards negative detuning as compared with c_i. This effect can be described by a nonlinearity in the optical resonance, whereby the cavity resonance frequency depends on the number of circulating photons [113]. This effect can arise from the optical Kerr effect, or from heating of the microdisk resonator causing changes in the index of refraction. Following the work of Barclay *et al.* [113], only one additional parameter is needed, δ_{nl}, which is a power dependent shift to the detuning. This nonlinear effect can be described mathematically as

$$n = \frac{2\kappa_e \bar{s}^2}{\kappa^2} \frac{1}{1 + (\delta + \delta_{\mathrm{nl}} n)^2},$$ (4.20)

which can be numerically solved at each detuning for n. This shift in resonance frequency, $\delta_{\mathrm{nl}} n$, is added to the laser detuning to compensate for the asymmetric shifts in resonance frequency. In Figure 4.2b we show example $c_i(\delta + \delta_{\mathrm{nl}} n)$ functions.

4.6 The experiment

To collect data, 1590 nm light from a tunable diode laser is transmitted through the optomechanical cavity, coupled via a tapered-dimpled fiber [114, 115] touching the microdisk, and collected on a photodetector. The photodetector signal was simultaneously measured with a low frequency analog-to-digital converter and a 50 MHz digital lock-in amplifier performing heterodyne downconversion to allow low sample rate measurements of the signal within a ~ 60 kHz bandwidth of both the 1Ω and
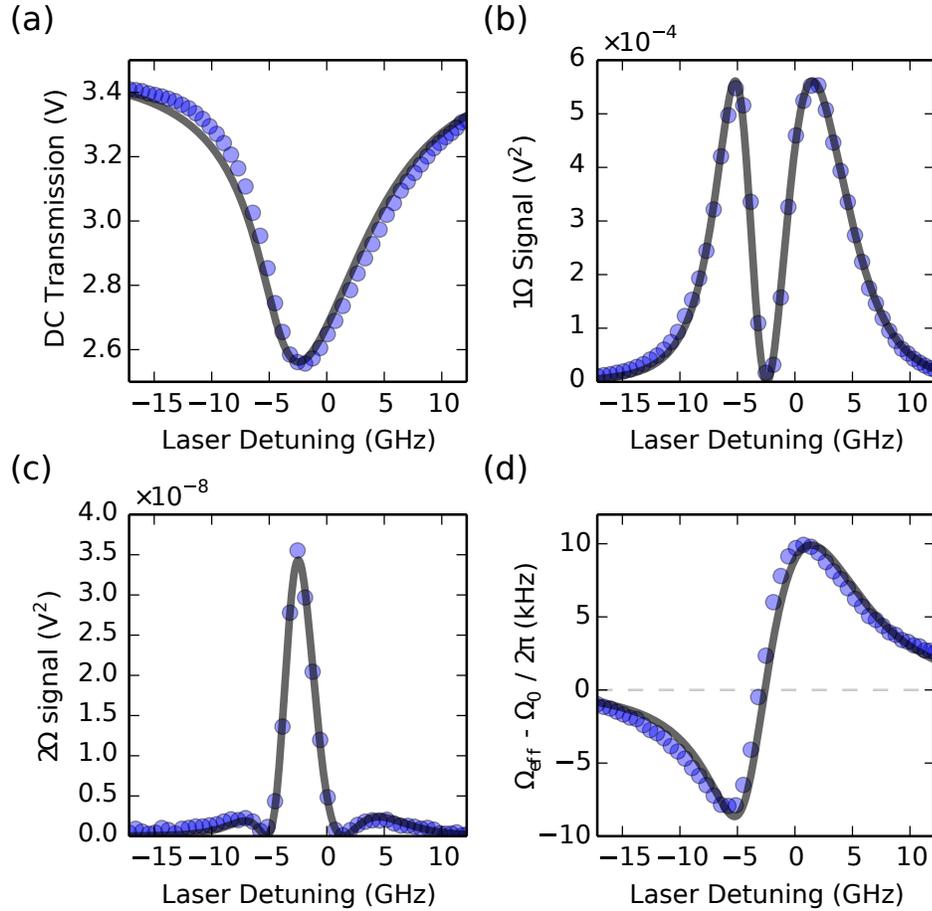
Figure 4.3: Quantitative signals extracted from Figure 4.1a, c and d, with respect to laser detuning, δ: (a) DC optical resonance, (b) 1Ω signal, (c) 2Ω signal, and (d) optical spring effect. Blue points in (b and c) are found by summing across the mechanical bandwidth. Grey curves are simultaneous least squares fits to all four signals as explained in the text.

2Ω signals. The tunable laser was scanned across the optical resonance with ≈ 3.6 s of high frequency transmission data recorded for each detuning, while calibrating laser drive frequency with an external wavelength meter. The power spectral densities (PSDs) [21] of the 1Ω and 2Ω signals were estimated from Fourier-transforming the time-series data [116], as shown in Figures 4.1c and 4.1d.

The signals at 1Ω and 2Ω were measured by integrating across the measured PSD bandwidth and subtracting the contribution from the noise floor. The spectrally white off-resonance noise floor was detuning-dependent, and extracted across both the 1Ω and 2Ω signals. The 1Ω PSD was fit with a damped harmonic oscillator spectrum [21], extracting values for Ω_{eff} (Figure 4.1d) and Γ (Figure 4.5a) at each detuning.

The power going into the optomechanical cavity, 540 µW, was calibrated by measuring the laser power before the tapered fiber with a power meter. The tapered fiber was measured to have near-100% transmission when not coupling, and scattering losses of 36% from touching the optical microdisk. These losses gave excellent agreement to the photodetector's received power and were used to determine $\bar{s}^2 = 2.8 \times 10^{15}$ photons per second.

A nonlinear least-squares fit was performed simultaneously to all four datasets presented in Figure 4.3, that is, the three parts of the optomechanical transfer function – DC optical resonance, mechanical signal at 1Ω and at 2Ω – as well as the optical spring effect. From the fit, the following parameters were extracted: $\kappa = 5.82 \pm 0.02$ GHz, $\kappa_e = 0.42 \pm 0.01$ GHz, $\delta_{\text{nl}}\kappa = 5.2 \pm 0.6$ kHz/photon, $G_1 = 458 \pm 2$ MHz/nm, $G_2 = -1.0 \pm 0.6$ MHz/nm^2, and $\Omega_0/2\pi = 6015.3 \pm 0.3$ kHz. Errors are standard deviations estimated from the fit covariance across a range of initial parameter configurations. The least squares algorithm used is only guaranteed to have found a local minimum, however it provides representative numbers and is in reasonable agreement with the calculations for G_1 done in Chapter 3 which found $G_1 = 720$ MHz/nm [22].
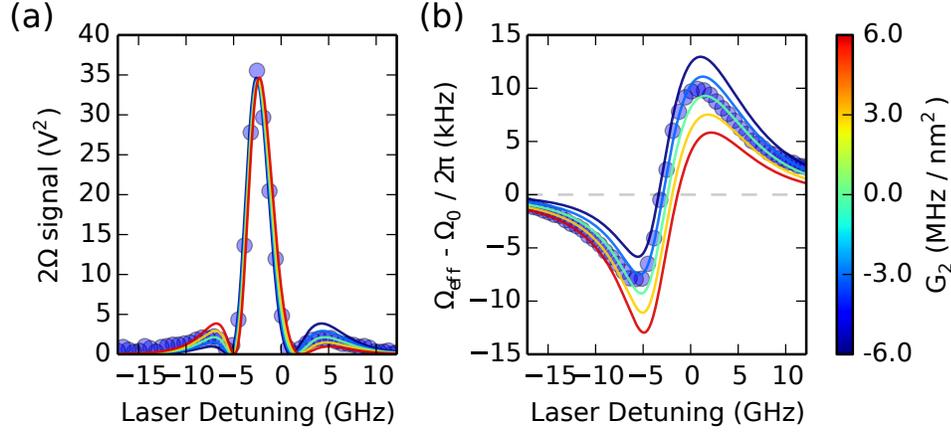
Figure 4.4: Dependence of the (a) 2Ω and (b) optical spring effect signals on the second-order optomechanical coupling, G_2. Here G_2 transfers spectral weight between detunings.
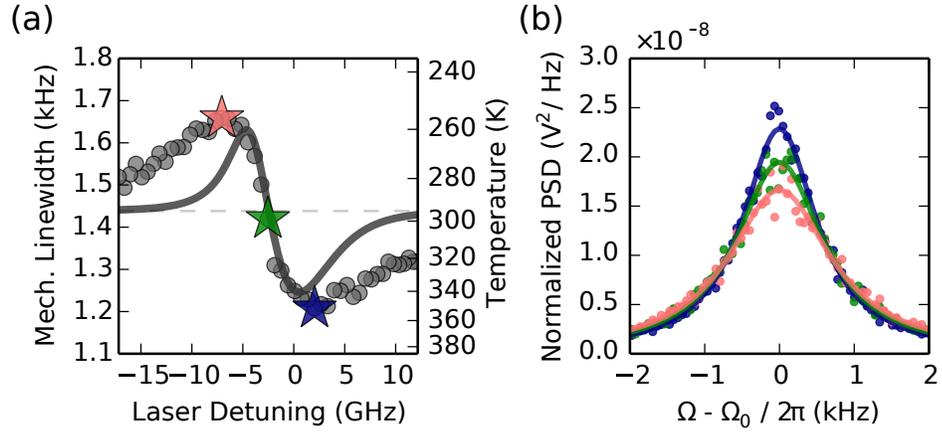
Figure 4.5: Dynamical effects on the mechanical resonator from the optical cavity. (a) The linewidth of the mechanical resonator is damped and then amplified as the optical detuning is varied from negative (red detuning) to positive (blue detuning). Curve is the theoretical mechanical linewidth using the parameters derived from the nonlinear least squares fit. (b) The corresponding power spectral densities at three detunings. The colors of the data correspond to the stars in panel (a), and are 349 K (red), 297 K (green) and 254 K (blue) [117].

In the present device, the signal at 2Ω is dominated by the contribution to the optomechanical transfer function from the curvature of the optical resonance, that is the term proportional to $c_2 G_1^2/\kappa^2$. While this signal is a measurement of x^2, it is not appropriate for a QND measurement as the optical resonator continuously introduces back action into the phase, creating uncertainty in $\hat{x}$ at future times. Only the contribution from G_2 is pertinent to a QND measurement of the energy, and in order to elucidate this contribution we show in Figure 4.4 the 2Ω signal and the optical spring effect data with varying G_2 while keeping all other parameters fixed. It is interesting to note that while the sign of G_1 is irrelevant, the sign of G_2 is important. Specifically, moving from negative to positive values of G_2 shifts spectral weight as a function of detuning.

We note that our optomechanical coupling constants G_1 and G_2 correspond respectively to a single photon to single phonon coupling rate $(G_1 x_{\mathrm{zpf}})$ of 35 kHz, and a single photon to two phonon coupling rate $|G_2 x_{\mathrm{zpf}}^2|$ of 6 mHz, where $x_{\mathrm{zpf}} = \sqrt{\hbar/2m\Omega_0} = 76.2$ fm. As a minimum requirement, we expect that the single photon - two phonon coupling rate should be larger than Γ (~ 1.44 kHz) to make a continuous measurement of the quantized energy states before decoherence—not satisfied with the present device—although measurements of phonon shot noise may be possible with weaker coupling [118]. Further requirements, such as minimizing thermal noise by requiring the thermal phonon occupancy $n_{\mathrm{th}} \ll 1$, would need to be met. This requirement could be achieved through the combination of cryostat cooling of the thermal bath, coupled with optomechanical cooling—which would require devices with a second optical mode in the sideband-resolved regime [118]. Finally, the first-order optomechanical coupling would have to be minimized [119], and although not explored here, dissipative coupling of the mechanical motion to the optical cavity loss rate κ would prevent QND measurements of phonon number and therefore need to be minimized as well [100].

4.7 Dynamical backaction

Finally, our stationary regime model does not account for dynamical back-action to the mechanical spectrum [120, 121], as the optical resonance is always in its steady state. Nonetheless, back-action from light-induced forces in the sideband unresolved regime is expected [117, 39]. Analysis of the mechanical linewidth as a function of detuning from the 1Ω signal (from Figure 4.1c) reveals non-negligible optomechanical damping and amplification, presented in Figure 4.5. The theoretical curve for optomechanical damping, using the fit parameters determined in Figure 4.3, is given in Figure 4.5 with reasonable agreement [117, 39]. As a result the mechanical mode is heated (cooled) from 297 K to 349 K (254 K).

4.8 Conclusion

Motivated by the search for experimentally realizable approaches to continuous QND measurements of a nanomechanical resonator's energy, we have developed a method to separate nonlinear transduction of first order optomechanical coupling from second-order optomechanical coupling. Both transduction mechanisms give rise to frequency doubling in the mechanical spectrum, however the detuning dependence in both the 2Ω power spectrum and the optomechanical spring effect allow determination of the optomechanical coupling constants. Fitting our experimental data to these models reveals a second-order coupling, G_2, of MHz/nm^2. Future improvements – including extension of this framework to the sideband resolved (non-stationary) regime, and enhancing this second-order coupling, while eliminating the first order optomechanical coupling, through fabricating a fully symmetric device in both mechanical motion and evanescent optical field – provide a route towards QND measurements of phonon number, as well as exotic phenomena such as quantum superpositions of nanomechanical resonators [122].

Chapter 5

Silicon nitride nanostrings at cryogenic temperatures

5.1   Introduction

Mechanical resonators fabricated from silicon nitride (SiN) have generated significant interest as their intrinsic tensile stress results in abnormally high-quality factors when operated in vacuum [56]. Silicon nitride membranes at cryogenic temperatures have demonstrated quality factors of over 10^8 [123], while at room temperature SiN trampoline resonators have demonstrated quality factors exceeding 10^7 [60, 69], and more recently phononically engineered SiN nanobeams have demonstrated quality factors of almost 10^9 at room temperatures [70]. These devices surpass the room-temperature "quantum coherent" limit of $Q \times f > 6 \times 10^{12}$, suggesting SiN mechanical resonators may find use in quantum applications without necessitating cryogenic cooling [69, 70, 39].

At cryogenic temperatures, optomechanical cavities have been used with much success to demonstrate quantum interactions such as entanglement [86, 124], optical and mechanical squeezing [125, 126, 127, 128], and single phonon measurements [129,

130]. Integrating high-Q SiN mechanical elements in optomechanical cavities [64, 131] has obvious upsides for quantum experiments [126], as well for low-noise force [54, 60] and acceleration [132, 133] sensors.

Recent measurements of silicon [134, 135] and gallium arsenide [136] optomechanical cavities at sub-Kelvin temperatures have demonstrated considerable heating of the mechanics resulting from the optical measurement. Due to the large optical band gap of SiN, we predict SiN optomechanical devices may produce less heating and therefore be well-suited to optical measurements at these low temperatures. We present measurements of optically induced heating at sub-Kelvin temperatures in an integrated optomechanical cavity with the optical and mechanical resonator fabricated from a single layer of high-stress silicon nitride.

5.2   Device and methods

The mechanical device studied here is a silicon nitride nanostring 16 μm long and 170 nm in width, fabricated from a 220 nm thick film of high-stress stoichiometric LPCVD silicon nitride—for fabrication details see Appendix A.2. The string exhibits two mechanical modes, an in-plane mode and an out-of-plane mode, both vibrating at ~ 14 MHz and having effective masses of 1.3 pg, as determined through finite-element method (FEM) modeling of the mechanical modes. FEM modeling indicates the in-plane mode exhibits a higher resonance frequency, which we used to provide identification of the modes.

To enable optomechanical readout of the nanostring's motion, the mechanical resonator is fabricated 240 nm away from a 30 μm diameter optical microdisk ($Q_{\mathrm{opt}} \sim 3.8 \times 10^5$), such that the mechanical motion is optomechanically transduced into frequency modulations of the microdisk as described theoretically in Chapter 2, and similar to the silicon cantilevers described in Chapter 3. To encourage optomechanical
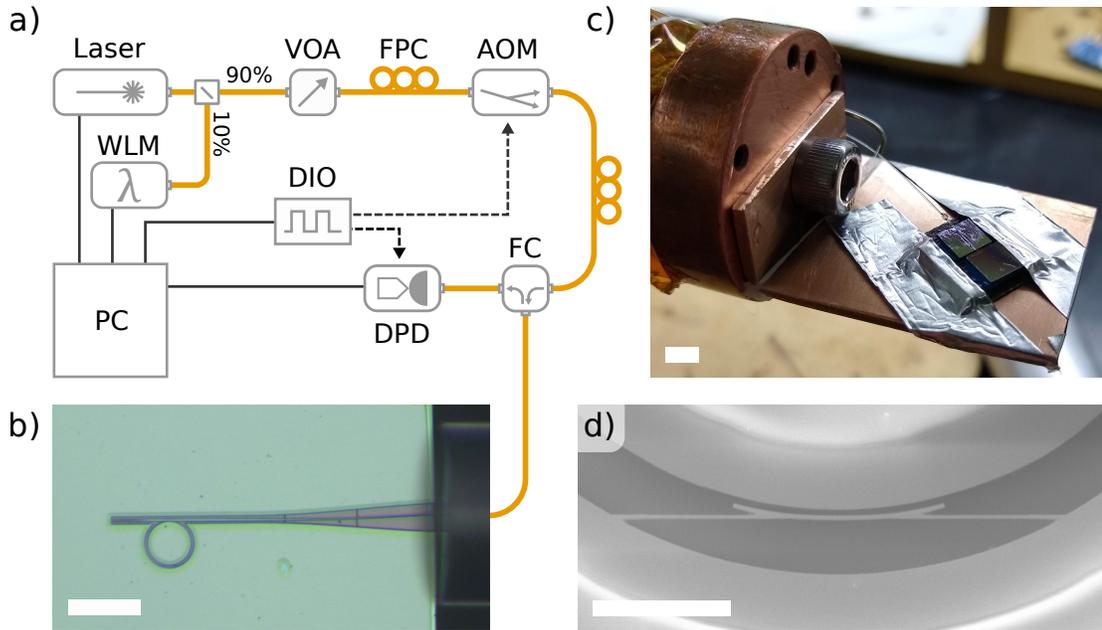
Figure 5.1: a) Schematic of the experimental setup used to take measurements. Nominally 1550 nm laser light is conditioned with a variable optical attenuator (VOA) and fiber polarization controller (FPC) before being modulated with an acousto-optic modulator (AOM) to control on and off times of the laser with microsecond switching times. A fiber circulator (FC) is used to collect the reflected signal from the device which is measured on a digitizing photodetector (DPD). A digital waveform generator (DIO) is used to send a digital waveform to the AOM and DPD for programming pulse times and synchronization with data collection. b) An optical microscope image of the fiber-coupled optomechanical device. Scalebar 50 μm. c) An image of the fiber-coupled device mounted on the cold-head of a 400 mK 3He probe. d) and scanning electron microscope (SEM) image of the mechanical resonator positioned next the the optical microdisk. Scalebar 5 μm.

coupling between the nanostring and the microdisk, the mechanical resonator was designed with an arc following $\pi/6$ radians of the microdisk circumference to increase overlap of the optical mode's evanescent field with the nanostring, as can be seen in Figure 5.1d.

The nanostring and microdisk are fabricated 200 μm from the cleaved edge of the wafer (see Appendix A.2 for details on how this was achieved), with a 1200 nm wide waveguide coupled to the microdisk opposite the nanostring. The waveguide tapers down to a width of 550 nm at the edge of the chip to provide matching of the

waveguide mode's effective index of refraction to the that of an optical fiber [131, 137], such that a cleaved optical fiber can be positioned in-line with the waveguide to provide coupling with the on-chip optics. Past the optical microdisk, the waveguide is terminated with a photonic crystal mirror such that the waveguide light is reflected and returned back to the same coupling fiber. This reflection from the mirror causes the light to interact with the optical cavity a second time, but in a counter-clockwise direction. Coupling between the clockwise and counter-clockwise modes, enhanced by the waveguide mirror, results in hybridization and splitting in the frequencies of the optical modes [138]. This results in a second optical mode being visible in the transmission spectrum—slightly visible in Figure 5.2a. Throughout this work the optical mode was treated as a single optical mode, however a more advanced treatment considering the coupling between the two optical modes could be considered [138]. By comparing input optical power to the chip with collected power, a total coupling efficiency of 10% was measured, or assuming equal loss coupling in-to and out-of of the waveguide, a 32% coupling efficiency in each direction. An optical microscope image of the fiber-coupled device is shown in Figure 5.1b.

As diagramed in Figure 5.1, measurements were taken by sending light from a 1550 nm tunable diode laser (NewFocus TLB-6330) through an acousto-optic modulator (Gooch & Housego) to enable microsecond-timescale switching of the optical power to enable the pulsed measurement scheme described later. A wavelength meter picking up 10% of the laser output was used to provide low-frequency, Hz-rate feedback to the tunable laser to stabilize the tunable laser over the time-scale of days. By using a fiber circulator, reflected light from the device is isolated and detected with a low-noise digitizing photodetector (Resolved Instruments DPD80).

To investigate the low-temperature behavior of the nanostrings, the device was fixed to the cold-head of a ^{3}He cryostat capable of cooling to temperatures below 400 mK. By using a fixed fiber-coupling technique, the device is able to attach to low-

temperature probes with minimal space, negating the need for any low-temperature positioning stages to perform alignment at cryogenic temperatures, such as done in [139, 140]. However, during cooldown temperature-induced contractions reduced total coupling to about 55% of initial value, reducing one-way coupling efficiency to $\sim 24\%$. A photographic image of the fiber-chip assembly attached to the cold-head is shown in Figure 5.1c.

For heat-sensitive measurements at fridge temperatures, a pulsing scheme is used that will be further described in Section 5.4. A digital waveform generator (DIO) is used to supply logic signals to the AOM and the digitizing photodetector (DPD) such that data collection of the second pulse is well synchronized. To perform time-resolved measurements of the mechanical resonator's motion, the time-series optical signal collected with the DPD is demodulated at Ω and filtered to perform a lock-in type measurement to extract amplitude (see Section 7.3.3). A 2 kHz linear-phase filter is used such that no delay is introduced to the processed amplitude signal, allowing precise calibration of pulse turn-on time, however also restricting time-resolution to ~ 500 µs. To reduce noise, the amplitude signal from 100 pulses are averaged together to perform a measurement of one pulse—such as the curves in Figure 5.3a. Identical lock-in measurements are performed off resonance to estimate imprecision noise from photon shot-noise and measurement electronics and subtracted.

We quickly note that given the frequency of the mechanical resonator ($\Omega \sim 14$ MHz) and the temperatures studied here (T > 400 mK), we expect at least 600 phonons to occupy the mechanical mode. In this limit ($n \gg 1$), we can neglect the zero-point motion of the mechanical resonator and treat the number of phonons, n, mean squared displacement of the mechanical mode, $\langle x^2 \rangle$, and the effective mode temperature T as linearly proportional measurements of the same quantity—the mode energy: $E = \hbar\Omega n = m_{\text{eff}}\Omega^2\langle x^2 \rangle = k_{\text{B}}T$. Thus even though notation implies phonon number, it may be given in units of temperature and is interchangeable.
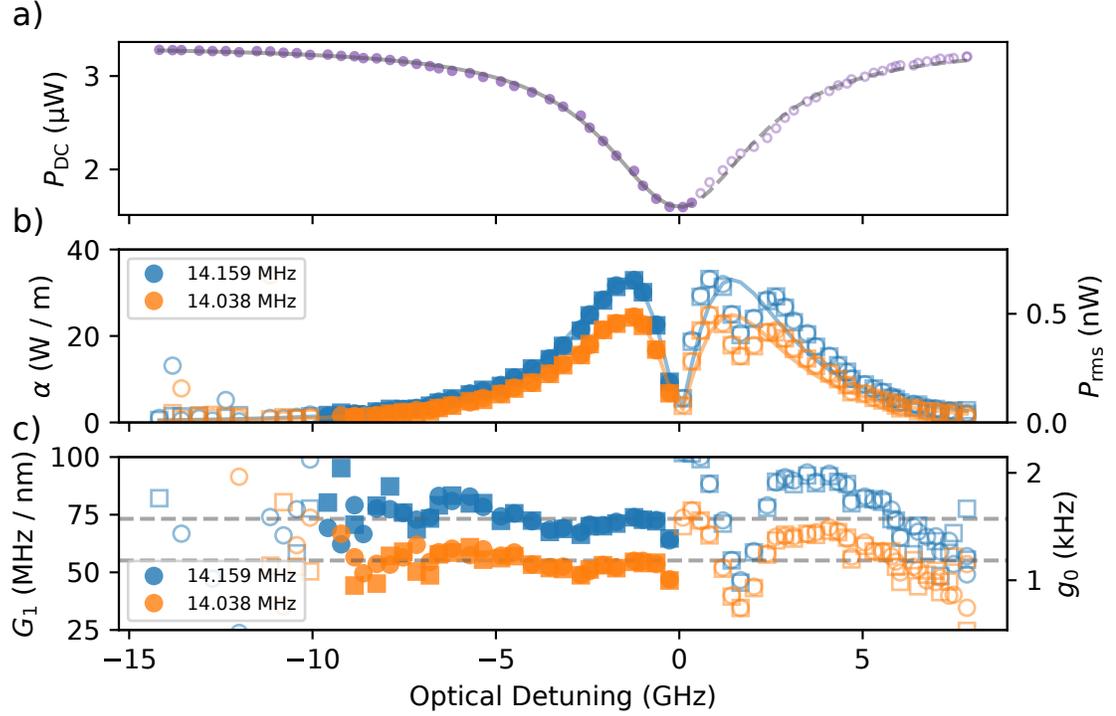
Figure 5.2: a) DC photodetector signal of the optical transmission as the laser is scanned over an optical resonance at 1572 nm. Due to asymmetries in the optical resonance, only datapoints red-detuned from cavity resonance were used to extract optical parameters (filled purple dots). X-axis is the same across all three subplots. b) The optomechanical gain and AC optical power measured around 14.159 MHz (blue–out-of-plane) and 14.038 MHz (orange–in-plane). Circles represent AC power determined through fitting the mechanical power spectra, while squares indicate AC power determined from direct integration of band-passed power. c) From the optical resonance parameters and the optomechanical gain (α), the optomechanical coupling coefficient, G_1 can be determined at each optical detuning. The average of the filled in markers was used to extract $G_1/2\pi$ of 73 MHz/nm and 55 MHz/nm for the out-of-plane and in-plane modes respectively.

5.3   Room-temperature characterization

At room temperature, the optomechanical nanostring-microdisk device was characterized to extract the optomechanical coupling coefficient. Measurements of the thermomechanical motion of the nanostring were taken as the tunable laser was stepped across the optical resonance. In agreement with the tuned-to-the-slope coupling theory presented in Chapter 2, the most effective amplification of the mechanical motion was observed slightly off resonance where the slope of the optical resonance is steepest–Figure 5.2. Although the blue-detuned side of the optical resonance disagreed with simple theory due to the presence of the counter-propagating optical mode, the optomechanical gain ($\alpha_{\mathrm{max}} \sim 30$ W/m) was fit on the red-detuned side of the optical resonance to determine the first-order optomechanical coupling coefficient ($G_1 = \partial\omega/\partial x$) to find $G_1/2\pi = 73 \pm 5$ MHz/nm and $G_1/2\pi = 55 \pm 4$ MHz/nm for the in-plane and out-of-plane modes, respectively. Errors in coupling rates are the standard deviations of the coupling rates due to their slight optical tuning dependance—illustrated by the filled markers in Figure 5.2c. With zero-point motions of $x_{\mathrm{zpf}} = 21$ fm, these coefficients result in optomechanical coupling rates ($g_0 = x_{\mathrm{zpf}}G_1$) of $g_0/2\pi = 1.6 \pm 0.1$ kHz and $g_0/2\pi = 1.2 \pm 0.1$ kHz.

Although this coupling was strong enough to observe thermomechanical motion with a sensitivity of 70 fm/$\sqrt{\mathrm{Hz}}$, we were unable to observe shifts in frequency as a result of the optomechanical spring effect, or changes in mechanical line-width from optomechanical heating or cooling. Compared with the measurements in Chapter 4, the optomechanical coupling is approximately 10 times smaller. This smaller coupling may be explained by the relatively large gap between the mechanics and optical disk of 240 nm, and the larger index of refraction of silicon over silicon nitride. Improvements to the device geometry, fine-tuning the fabrication process and implementation of stress-induced gap-narrowing process [141] should lead to similar devices with improved optomechanical coupling.

As the device is under tension, we do not anticipate any significant changes to the device geometry during cooling to low temperatures and therefore expect the optomechanical coupling to remain constant. Therefore by using the optomechanical coupling coefficient extracted at room temperature and optical resonance parameters extracted at low temperatures, the mean-squared displacement–and thus temperature of the mechanical mode–can be calculated without necessitating calibration with fridge thermometry. In the following sections and figures, whenever number of phonons is reported as a temperature, these are determined through this absolute optomechanical calibration, not through reference with fridge thermometry.

5.4   Low-temperature pulsed measurements

As has been previously demonstrated in optomechanical devices fabricated in silicon [134, 135] and gallium arsenide [136], optical losses at the resonator can contribute significant heating to the mechanical modes. These photons lost from the optical resonator are absorbed, creating a hot phonon bath that couples to and causes heating of the mechanical mode. These previous studies have implemented a pulsed measurement scheme to investigate this heating, whereby the optical drive signal is turned on for a short period and a time-resolved measurement of the mechanical resonator's energy, $n(t)$, is performed.

Following the previous work, this heating process can be modeled as coupling of the nanomechanical mode to two baths: to the hot photon-induced bath n_p with coupling rate Γ_p, and to the cold bath at the base temperature of the fridge n_{th} with rate Γ_i. This process can be modeled as a first-order differential equation:

$$\dot{n}(t) = -\Gamma n(t) + \Gamma_i n_{th} + \Gamma_p n_p, \tag{5.1}$$

where Γ is the total coupling, $\Gamma = \Gamma_i + \Gamma_p$. We can solve this equation requiring one known boundary condition, $n(t_0) = n_0$, to find:

$$n_{\text{heat}}(t) = n_{\text{eq}} + (n_0 - n_{\text{eq}})\, e^{-\Gamma(t-t_0)}, \qquad (5.2)$$

where we have introduced n_{eq} as the steady-state solution to equation (5.1),

$$n_{\text{eq}} = \frac{\Gamma_i n_{\text{th}} + \Gamma_p n_p}{\Gamma}. \qquad (5.3)$$

That is, given the resonator's energy at a point in time, $n(t_0) = n_0$, $n(t - t_0)$ will exponentially decay towards the steady-state energy over a characteristic time $\tau = 1/\Gamma$.

During the optical measurement, the hot phonon bath described above is present and will act to heat the mechanical mode to n_{eq}. However, when the optical measurement is turned off, the hot phonon bath and coupling to it, Γ_p, will go to zero. In this case, the steady-state occupancy of the mode reduces to the fridge's base temperature n_{th}, while the total loss rate from the resonator reduces to the intrinsic damping rate Γ_i, such that if the resonator starts with $n(t_0) = n_{\text{eq}}$, it follows

$$n_{\text{cool}}(t) = n_{\text{th}} + (n_{\text{eq}} - n_{\text{th}})e^{-\Gamma_i(t-t_0)}, \qquad (5.4)$$

such that the mechanical mode cools to the fridge temperature on a time scale of $\tau_i = 1/\Gamma_i$.

To measure the intrinsic and hot-bath induced damping rates, a double-pulse measurement is used to implement a pump/probe scheme [134, 135]. For the pump pulse, the optical measurement is turned on for a period $t_{\text{on}} = 15$ ms such that the mechanical mode heats up to steady-state conditions. The measurement laser is then switched off for a ring-down time period t_{off}, after which a second 15 ms measurement–
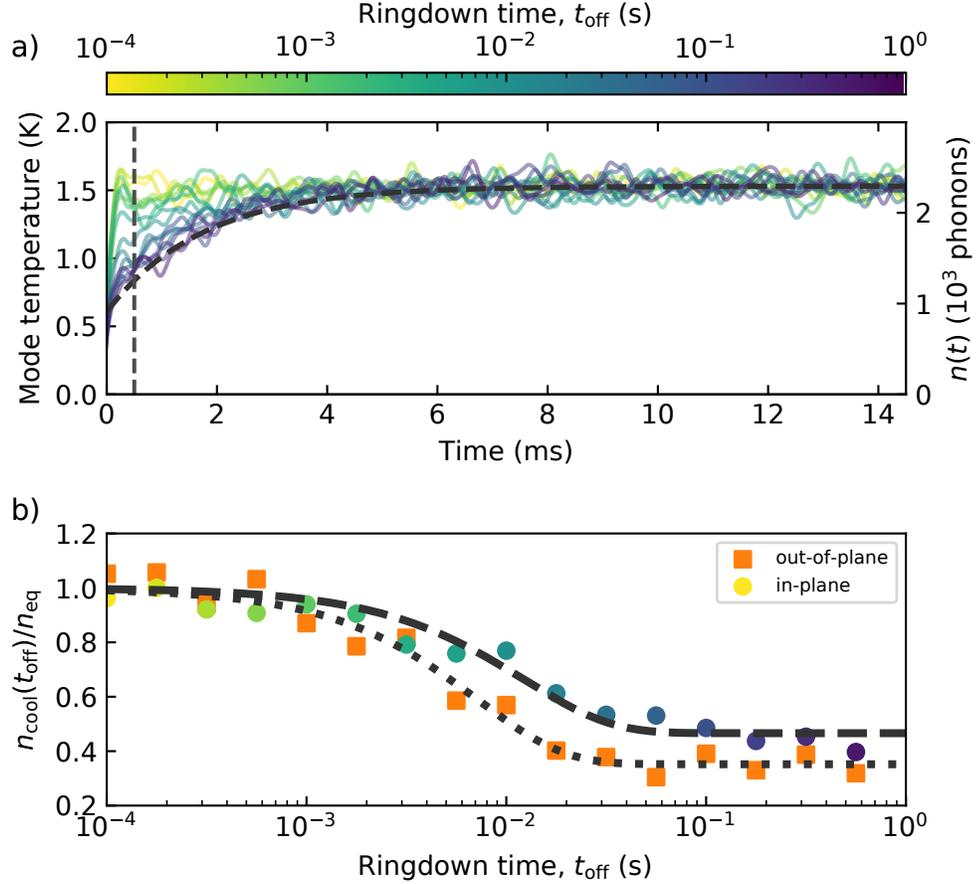
Figure 5.3: a) An example measurement of the probe pulse in the two-pulse measurement scheme described in the text. In-plane mode signal is converted to an effective mode temperature, and number of phonons, using the optomechanical coupling coefficient determined at room temperature. Pulses measured at varying ringdown times are color coded according to the colorbar. Fridge temperature is stabilized to 420 mK. An example fit to equation (5.3) for the pulse with a ringdown time of 0.56 s is overlaid (dashed line). The pulse is fit from 0.5 ms $< t <$ 14.5 ms corresponding to the filter time-constant (vertical dashed line), and $n(t)$ is extrapolated back to $t = 0$ to determine $n_{\mathrm{cool}}(t_{\mathrm{off}})$. b) Fitting the exponential decay found from extracting $n_{\mathrm{cool}}(t_{\mathrm{off}})$ and n_{eq} extracted from the probe measurements, the intrinsic damping Γ_{i} can be determined. Colored circles correspond to the pulses in a). Orange squares correspond to the out-of-plane mode measured simultaneously with the in-plane mode.

the probe pulse–is performed and recorded. Finally, the optical measurement is then turned off again for a much longer period such that the average laser power into the fridge is 2% of the peak power, and the pump/probe measurement repeated. A set of probe measurements across a range of ringdown times t_{off} between pump and probe pulses is shown in Figure 5.3a.

After the pump pulse is turned off, and before the probe pulse measures the mechanics again, the mechanical mode decays from n_{eq} towards n_{th} at a rate Γ_{i} following equation (5.4). Then during the probe pulse, the mechanical mode heats up from the temperature when the pulse turns on, $n_0 = n_{\text{cool}}(t_{\text{off}})$, to the steady state temperature n_{eq}. By fitting the probe pulse to equation (5.3), the temperature of the mechanics at the beginning of the probe, $n_0 = n_{\text{cool}}(t_{\text{off}})$, and the steady state temperature n_{eq}, can be found.

By repeating this measurement for a range of t_{off}, the ringdown behavior of $n_{\text{cool}}(t_{\text{off}})$ can be mapped out and fit to equation (5.4) to extract the cold-bath temperature n_{th} and the intrinsic dissipation rate of the mechanical resonator, Γ_{i}. Figure 5.3b plots the ratio of $n_{\text{cool}}(t_{\text{off}})$ to n_{eq} for the in-plane mode (corresponding to the pulse measurements shown in Figure 5.3a) measured at a fridge temperature of 420 mK. The intrinsic dissipation for the in-plane mode was found to be $\Gamma_{\text{i}}/2\pi = 13$ Hz ($Q = 1.1 \times 10^6$) and cold-bath temperature to be $n_{\text{th}} = 710$ mK. Note that based on our uncertainty in optomechanical coupling rate due to detuning, we expect an uncertainty level at about 10% in these values.

5.5   Discussion

Although the cold-bath temperature of 710 mK measured in Figure 5.3 does not agree precisely with fridge thermometry (420 mK), the measured temperature is determined completely through calibration of the optomechanical transduction and not
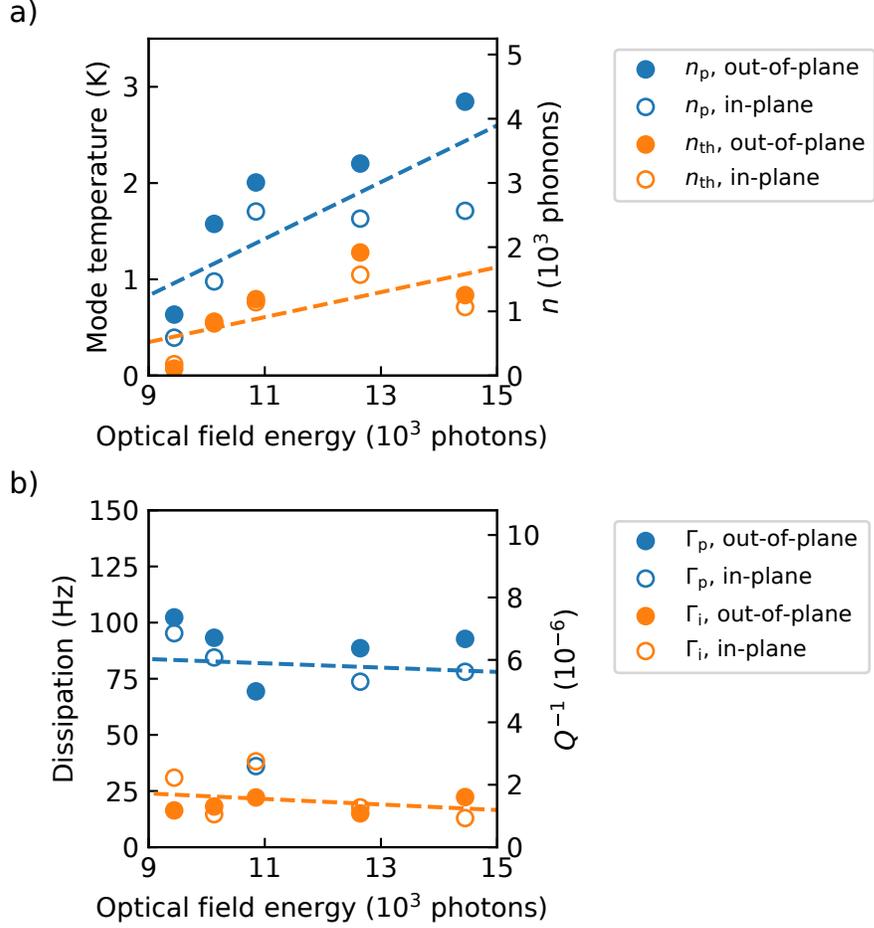
Figure 5.4: a) The cold-bath temperatures, n_{th}–orange, and hot photon-induced bath temperature, n_{p}–blue, plotted against intracavity photon number. Mode temperature is determined using room-temperature optomechanical coupling with low-temperature optical resonance fits to determine optomechanical gain to provide absolute calibration of the mechanical resonators displacement, and via the equipartition theorem, the mode's energy. Fridge temperature was at 420 mK for all measurements. Filled circles represent the out-of-plane mode, while open circles represent the in-plane mode. Dashed lines are linear fits to both in-plane and out-of-plane points for guides to the eye. b) The dissipation from the mechanical mode to hot photon-induced bath (blue) and to the cold fridge bath (orange). Again dashed lines are linear fits to both in-plane and out-of-plane datapoints.

based off fridge thermometry. The only external temperature reference used is the room temperature (295 K) used during the thermomechanical calibration illustrated in Figure 5.2. Despite temperature discrepancies, the device is able to maintain reasonable temperature accuracy over two orders of magnitude of temperature change. We attribute this to the monolithic fabrication of waveguide, optical resonator, and mechanical resonator providing relatively-fixed optomechanical parameters.

The mismatch of the mechanical mode temperature with the fridge thermometry may be an indication the mechanical device is not well thermalized to the cold plate of the fridge, inaccuracies in the optomechanical calibration, or a combination of the two. To further investigate this, measurements were taken while the laser was set to a variety of detunings on the red-side of the optical resonance to monitor how intra-cavity photon number in the microdisk affected heating of the nanostring. Measurements of the cold and hot phonon bath temperatures, n_{th} and n_{p}, and coupling to those baths, Γ_{i} and Γ_{p}, as a function of intracavity phonon number are shown in Figure 5.4.

We found both the hot-bath temperature n_{p} and cold bath temperature n_{th} showed positive correlations to intracavity photon number, indicating the cold phonon bath was not fully thermalized to the fridge temperatures. Interestingly, the in-plane and out-of-plane modes exhibited consistently different hot-bath temperatures (cold-bath temperatures remained in agreement), with the out-of-plane mode exhibiting an n_{p} 1.5 times that of the in-plane mode despite exhibiting an optomechanical coupling 1.3 times smaller than the in-plane mode. This implies that material properties and geometry play a dominant role in hot-bath temperatures compared with optomechanical coupling. Cold-bath temperatures remained consistent between in-plane and out-of-plane modes, and as shown in Figure 5.4b, there did not seem to be a significant correlation between intracavity phonon number and bath coupling rates.

Next, we explored the fridge temperature dependence by stabilizing the fridge to several temperature set-points up to 700 mK, maintaining $\sim$ 11000 intracavity photons—Figure 5.5. The intrinsic mechanical dissipation rate Γ_i (Figure 5.5b), of which measurement does not depend on absolute optomechanical calibration, does show a trend of decreasing with temperature, however as measurement is restricted to a temperature range of only a few hundred mK, measurements over a larger temperature range will be required to make definitive claims of the physical mechanism.

Contrary to what is expected, the measured cold-bath phonon mode temperatures displayed an inverse correlation to measured fridge temperatures (Figure 5.5a). While this may indicate improper thermalization to the fridge, because the 500 mK, 600 mK, and 700 mK cold-phonon bath temperatures are all measured to be less than the fridge temperatures, this indicates that the optomechanical gain calibration is inaccurate.

The optomechanical gain α, given by equation (2.65) and typically on the order of $\alpha \approx 30$ W/m for these measurements, depends on a number of device parameters:

$$\alpha = \frac{4\kappa_e \kappa_0 G_1 \bar{s}^2}{\kappa^3} \frac{2\Delta/\kappa}{(1 + (\Delta/\kappa)^2)^2}. \tag{5.5}$$

Here $\bar{s}^2 = 67 \times 10^{12}$ photons/s (8.5 μW) is the off-resonance optical power travelling through the waveguide, κ_e and κ_0 are the waveguide coupling and intrinsic loss rates of the microdisk ($\kappa_e/2\pi = 0.6$ GHz), $\kappa = \kappa_e + \kappa_0$ is the total microdisk loss rate ($\kappa/2\pi = 2.3$ GHz), and Δ is the laser detuning from the optical resonance frequency. Because each set of ringdown measurements were taken over a couple day time period, that provides ample time for drift in these parameters, skewing calculation of α. By better characterizing the optical resonance, carefully keeping track of parameter drifts by interweaving optical disk characterization with the pulse measurements, we expect to be able to better accurately determine α and therefore n_{th} to improve the optomechanical thermometry. Further, using a homodyne detection scheme where the
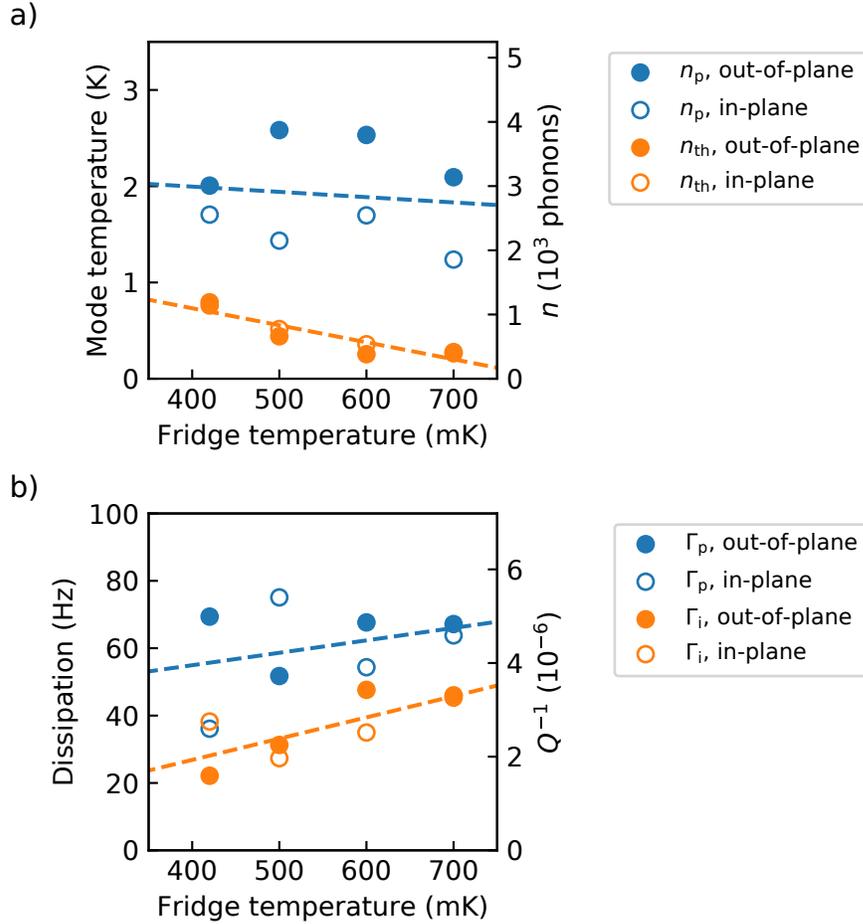
Figure 5.5: a) The cold-bath temperatures, n_{th}–orange, and hot photon-induced bath temperature, n_{p}–blue, plotted against fridge temperature. Mode temperature is determined using room-temperature optomechanical coupling with low-temperature optical resonance fits to determine optomechanical gain to provide absolute calibration of the mechanical resonators displacement, and via the equipartition theorem, the mode's energy. Filled circles represent the out-of-plane mode, while open circles represent the in-plane mode. Dashed lines are linear fits to both in-plane and out-of-plane points for guides to the eye. b) The dissipation from the mechanical mode to hot photon-induced bath (blue) and to the cold fridge bath (orange). Dashed lines are linear fits to both in-plane and out-of-plane datapoints.

laser is locked to optical resonance may also help eliminate drift in optomechanical transduction.

5.6 Conclusion

The picogram-scale silicon nitride nanostrings described in this chapter display a number of desirable characteristics that warrant further interest in high-stress silicon nitride optomechanical devices at sub Kelvin temperatures. With an optical power of a 8.5 μW coupling to the microdisk, heating of the mechanical resonator only reaches a couple Kelvin (a couple thousand phonons) in mode temperature. Compared with the similar frequency and geometry silicon devices characterized by Hauer *et al.* which heat up to ~ 80 K (8×10^4 phonons) [135], these devices present an noticeable improvement in optically-induced heating. We suggest this is due to the larger optical bandgap of silicon nitride [142], although the much lower optomechanical coupling of our devices may also play a large role–although in the modes studied here, optomechanical coupling did not correspond to the degree of optically-induced heating.

Quality factor wise, the best $Q = 10^6$ observed for the strings measured here match or exceed those of the silicon devices measured by Hauer *et al.* at similar fridge temperatures [135]. For the silicon nitride membranes measured at sub Kelvin temperatures by Yuan *et al*, they report a sharp increase in quality factor below 200 mK [123], suggesting lower temperatures may improve quality factors further–although device dimensions and mass differ by a factor of about 1000. By expanding the temperature range of measurements over from mK to 10s of K, the quality factor dependence of these pg-scale nanostrings could better be characterized.

Chapter 6

Refractometric sensing of Li salt with Si_3N_4 microdisk resonators [1]

6.1 Introduction

While in the previous Chapters we have used whisper-gallery mode (WGM) resonators for sensitive detection of mechanical displacement, optical WGM resonators are also under avid research for their promise of fast, sensitive and label-free detection of chemical and biological samples [144, 145, 146]. Sensors based on whispering-gallery mode resonators have been used for the label-free detection of single viruses [8, 9], nanoparticles [10, 11, 12, 13], single proteins [14], nucleotides [15, 16], and are even used commercially [17]. Many geometries have been used for bulk refractometric sensing. For example, glass whispering gallery mode resonators such as microspheres [147, 148] and toroids [14, 11, 149] exhibit ultra-high quality factors (Qs) of $> 10^9$ allowing precise readout of optical mode wavelengths, and with tens of nm/RIU sensitivity achieve detection limits of 10^{-7} refractive index units (RIU) [5, 147]. Glass WGMs with a hollow core, dubbed liquid core optical ring resonators (LCORRs), have

---

been shown to achieve gigantic sensitivities of 570 nm/RIU when carefully engineered such that the optical mode sits largely in the liquid core instead of the glass [150]. With Qs of 10^5 these represent the best bulk refractive index sensors in the literature, achieving a limit of detection of 3.8×10^{-8} RIU.

LCORRs are remarkably impressive, but for the purposes of integration - such as into lab-on-a-chip devices - it may be more useful to have WGM resonators fabricated on CMOS compatible chips. The commercially proven silicon-on-insulator platform has been used to fabricate optical resonators in planar geometries, which allows for full integration. Simple planar WGM geometries such as disk [151, 152] or ring [153, 154, 155] resonators have demonstrated sensitivities up to 160 nm/RIU with Qs up to 10^5. Slot WGM resonators are of significant interest, due to their ability to be engineered such that the optical mode lies mostly within the slot and outside the resonator medium [156, 157, 158] demonstrating up to 298 nm/RIU [157] but with Qs reaching only a couple thousand; photonic crystal resonators utilize photonic bandgaps to highly localize the optical mode [159, 10] and have demonstrated 490 nm/RIU sensitivities with similar Qs.

Here we demonstrate an attractive permutation of an on-chip WGM resonator to be used for refractive index sensing: a thin silicon nitride microdisk resonator [7, 160]. Si_3N_4 is a desirable material for optical sensing due to its CMOS compatibility [161], transparency to visible light, and lower refractive index than silicon resulting in less mode confinement [162]. Si_3N_4 refractometric sensors have been described previously in optical ring and slot geometries [163, 156, 158], and with optimization have achieved sensitivities of 246 nm/RIU and detection limits of 5×10^{-6} RIU [158]. Here we exploit silicon nitride's transparency to 780 nm laser light to enable large portions of the optical field to be in water, negating much of the optical absorption caused by water at longer wavelengths. Using thin (< 150 nm) on-chip Si_3N_4 microdisks and an under-cut geometry to lower mode confinement, sensitivities of > 200 nm/RIU and
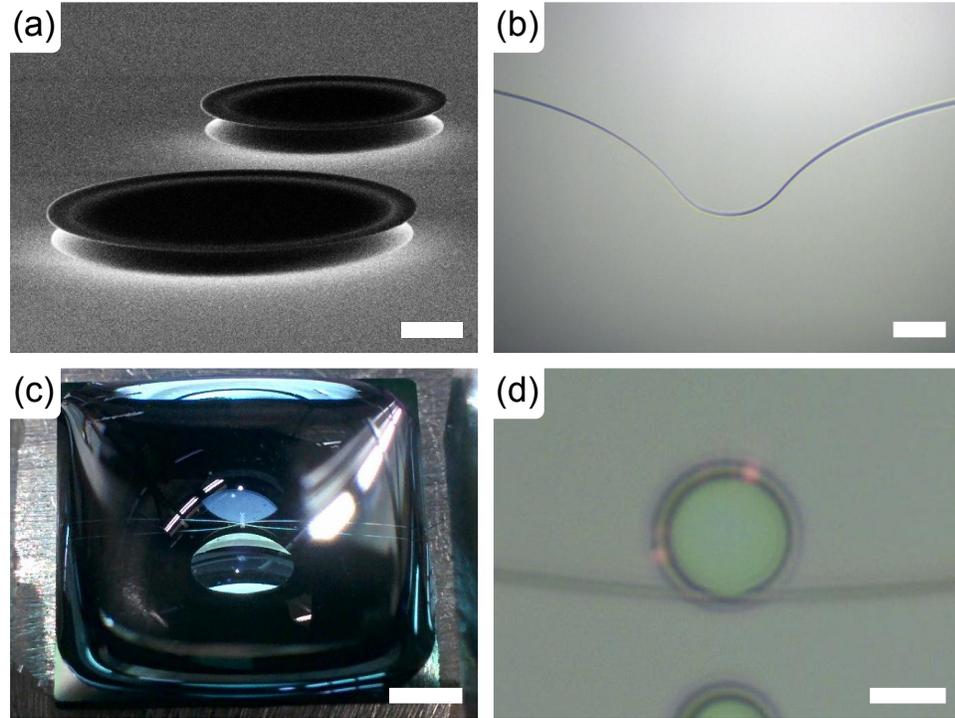
Figure 6.1: (a) Scanning electron microscope image of 20 μm and 30 μm microdisks. Scale bar 5 μm. (b) Side view of a dimpled-tapered fiber for visible light used to couple to individual microdisks. Scale bar 100 μm. (c) A representative ~140 μL water droplet deposited on a chip of microdisks. The tapered fiber is visible in the droplet touching the chip. Scale bar 2 mm. (d) The dimpled-tapered fiber is used to selectively couple light into a 20 μm microdisk. On resonance, light in the mode is visible due to surface scattering. Scale bar 10 μm.

a limit of detection of $\sim 1 \times 10^{-6}$ RIU are measured. This responsiveness results from extending the evanescent field into the aqueous solution, similar to photonic crystal or slot resonators, yet with less stringent fabrication requirements.

6.2   Experiment and methods

Si_3N_4 microdisks with diameters of 15, 20, 25 and 30 μm were fabricated and characterized for their bulk index of refraction sensitivity. Devices were fabricated with electron beam lithography (EBL) from silicon wafers with 3 μm of oxide beneath a 150 nm LPCVD deposited stoichiometric Si_3N_4 film (Rogue Valley Microdevices).

73

Further fabrication details are given in Appendix A.3. Although EBL was used to fabricate the current devices, the large minimum feature size of the microdisks would allow these devices to be fabricated with standard photolithographic processes.

To couple the 780 nm light into and out of the microdisks a dimpled-tapered fiber was used [114]. It was fabricated by tapering an optical fiber (Thorlabs SM600) to $\lesssim$ 1000 nm, the single-mode cutoff diameter for 780 nm light in air [115], and then molded to produce a section of the tapered fiber out-of-plane to the rest of the fiber - the dimple - as pictured in Figure 6.1b. The fiber was affixed to a pronged mount with the dimple extending downwards towards the chip, which was secured to a 3-axis nanopositioning system, allowing coupling to individual devices fabricated within a planar array [115]. An optical camera was used to monitor the coupling procedure and by varying the placement of the fiber, coupling to the microdisk can be tuned. The dimpled-tapered fiber allows operation over a large wavelength range, achieving > 50 % transmission through the taper over the entire range of our tunable laser (765–781 nm). Losses in transmission are primarily from non-adiabatic tapering of the optical fiber. To our knowledge, this was the first time coupling to a planar device with a dimpled-tapered fiber has been demonstrated with visible light in a liquid environment.

To conduct experiments in aqueous solution, a sample cell was created by depositing $\sim$ 140 µL of deionized water on top of the 10×10 mm wafer, creating a droplet, such as the one demonstrated in Figure 6.1c, in which the tapered fiber can be submerged. The system was housed in a closed chamber containing a water reservoir to increase humidity and minimize evaporation of the sample droplet. A micropipette was used to add small volumes of solution to the droplet and induce mixing to homogeneously distribute the solution. Introducing and removing the pipette tip from the water creates large mechanical oscillations of the droplet which were often enough to move the dimpled fiber a few µm, altering the coupling to the target resonator.
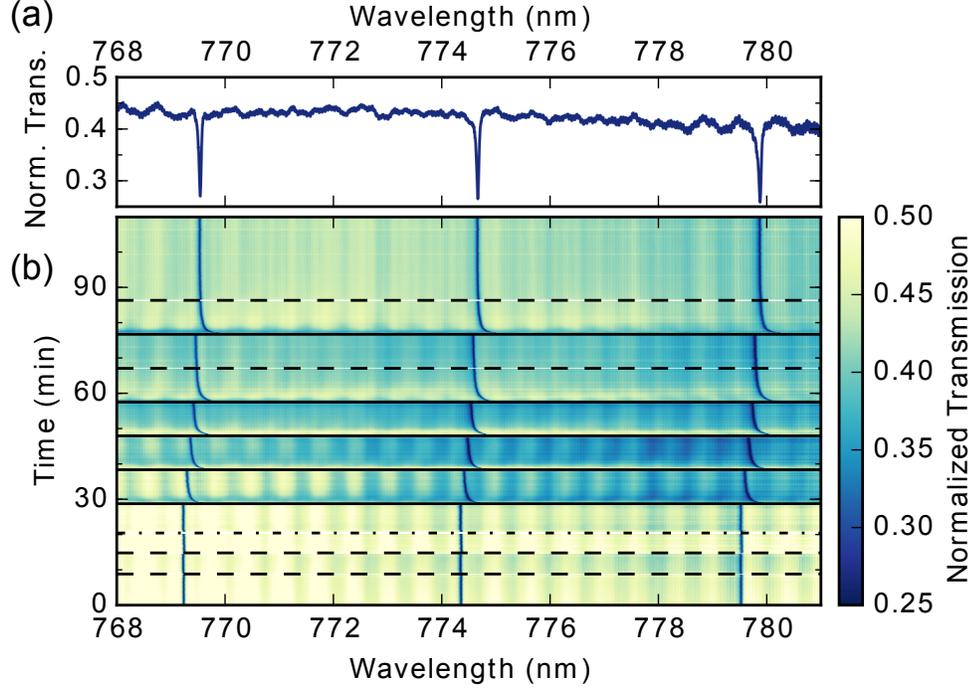
Figure 6.2: (a) The transmission spectra of visible laser light through a dimpled-tapered fiber coupled to a 20 μm diameter Si_3N_4 resonator. (b) By repeatedly scanning a tunable diode laser over its wavelength range, the time dependence of three $TE_{n=1}$ modes can be tracked as LiCl was added to the environment. Transmission spectra are normalized to uncoupled fiber transmission. Events, described in the text, are indicated by white lines. Spectrum in (a) was taken at 110 minutes.

This movement was minimized by attaching the fiber to the microdisk to provide mechanical stability during the experiment. This attachment has the disadvantage of lowering quality factors and obscuring detection of the $n > 1$ modes, where n is the radial mode number, in all but the 30 μm disk as well as inducing an additional scattering loss ($\sim 50\ \%$). Nonetheless, sufficient signal was retained to easily resolve the $TE_{n=1}$ modes [2].

Once coupled to a microdisk, the transmission spectra of light from a tunable diode laser (NewFocus TLB-6712) can be measured to determine the wavelengths and quality factors of the coupled whispering gallery modes. Before reaching the disk, the light was attenuated to $\lesssim 1$ mW to ensure linear behavior of the optical resonances and the polarization was controlled with a three-paddle polarization con-
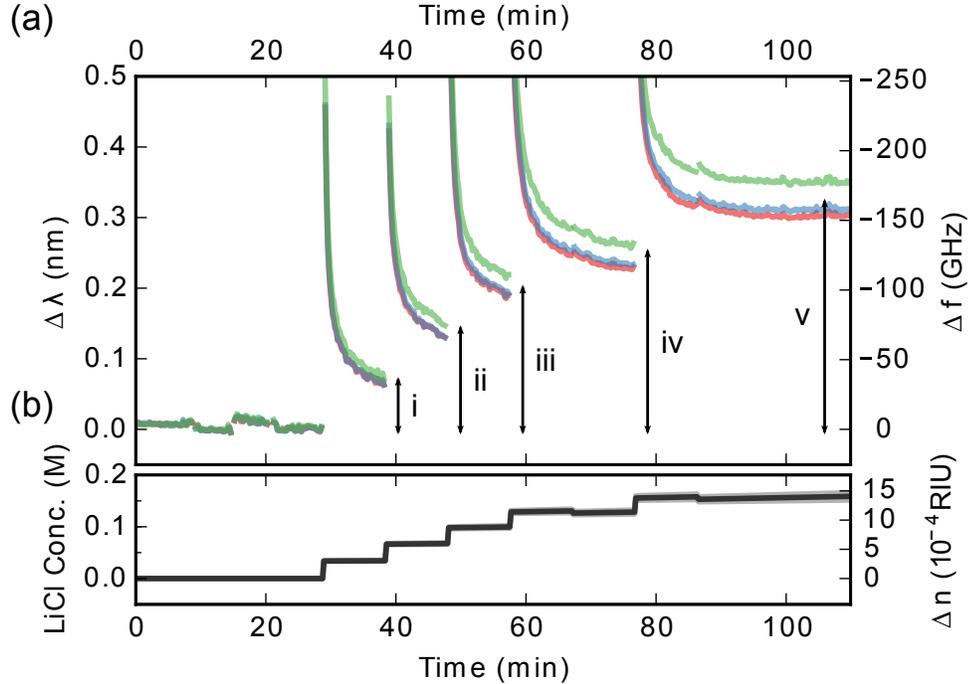
Figure 6.3:   (a) Fitting the transmission data in Figure 6.2b to Lorentzian line-shapes provides readout of wavelength (or frequency) shifts of the whispering gallery modes. The wavelength shifts marked i through v correspond to bulk refractive index sensitivities of 227, 238, 226, 221, and 229 nm/RIU respectively. Red, blue and green curves correspond to the wavelength shifts produced by the three optical modes visible in the range of the tunable laser. (b) Small amounts of concentrated Li salt solutions are periodically added to the sample cell increasing the LiCl concentration. These correspond to refractive index shifts above pure water (1.330 RIU) of 0.00886 RIU/M. Gray lines indicate concentration error limits, chiefly due to uncertainty in the water evaporation rate.

troller to optimize coupling to TE modes. Wavelengths are calibrated to the internal wavelength reference of the tunable laser, outputted as a voltage and collected synchronously with the fiber transmission. A wavelength scan while coupled to a 20 μm diameter microdisk is shown in Figure 6.2a. By automating repeated scanning of the laser, time resolved spectroscopy of the optical disk can be performed, allowing the wavelength of multiple whispering gallery modes to be simultaneously tracked, as visualized in Figure 6.2b.

To measure the bulk refractive index sensitivity of the microdisks, LiCl solutions with concentrations of 1 mol/L (1 M) were added to the sample cell in 5 μL vol-

umes, increasing the refractive index from pure water (1.330) linearly proportional to salt concentration with a slope of 0.00886 RIU/M [164]. This refractive index change caused wavelength shifts of the optical modes that, by automated fitting of Lorentzians to the resonances, provide quantitative readout of the wavelength change of each mode. Extracted wavelength shifts for the run in Figure 6.2b are plotted in Figure 6.3a. At 9, 15, 67 and 87 minutes, 5 μL of deionized water was added and mixed to the droplet, and at 21 minutes the droplet was mixed without adding or removing water. During these events the wavelength of each mode remained relatively unchanged. At 29, 39, 58, and 77 minutes 5 μL of 1 M LiCl was added to the droplets, causing large positive shifts of mode wavelengths. Interestingly, these events display transient behavior due to diffusion of the ions inside the droplet. The known times for Li^+ and Cl^- ions to diffuse a root-mean-square distance of 1 mm is 4 and 8 minutes respectively—similar to the time scales observed [164].

By tracking the volumes of deionized water and LiCl solution added to the sample cell, the concentration—and therefore the index of refraction of the environment—was determined. Uncertainty in the rate of evaporation of water from the droplet gave uncertainties in LiCl concentration as indicated in Figure 6.3b. Knowing the wavelength shift and index of refraction of the water allowed the bulk refractive index sensitivities of the whispering gallery modes to be determined and are plotted in Figure 6.4a, with errors representing standard deviations coming from a combination of variance between addition events (*e.g.* Figure 6.3a i–v), and wavelength and concentration uncertainties.

Axisymmetric simulations of the whispering gallery modes were performed to determine the theoretical refractive index sensitivity of the whispering gallery modes [165], as well as the mode quality factors due to radiative losses. Measured sensitivities for the disks were larger than expected for 150 nm thick disks, Figure 6.4b, however thinning of the disks during fabrication may explain the enhanced sensitivities. A
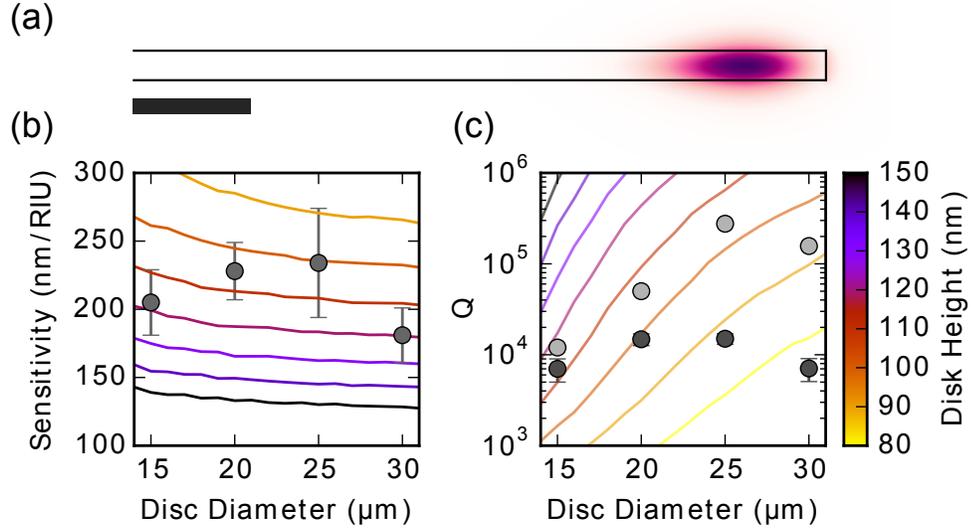
Figure 6.4: (a) The $TE_{n=1,m=121}$ mode shape of a 20 μm diameter, 130 nm thick, resonator determined through FEM simulations. Darker colors indicate larger magnitude electric field. Scale bar 1 μm. (b) Measured sensitivities plotted on-top of simulated sensitivities for a range of disk thicknesses. (c) Measured loaded (dark) and unloaded (light) quality factors (Qs) plotted on top of simulated radiative loss quality factors.

Si_3N_4 etch rate of only 0.3 nm/min would result in 120 nm thick discs. As expected, observed Qs are less than simulated (Figure 6.2b), as simulations neglect most loss mechanisms. With the tapered fiber attached to the microdisks, Qs of $\sim 10^4$ are observed, however hovering the tapered fiber away from the disks reduces fiber-induced losses and reveals unloaded Qs of $> 10^5$ for the 25 and 30 μm diameter disks, Figure 6.4c, as well as mode-splitting of a few pm—which could be used as an additional sensing mechanism [11]. Simulations also predict large radiative losses for TM modes, incompatible with the measured Qs and therefore provide mode identification as TE, visualized in Figure 6.4a.

6.3 Conclusion and future work

Evaluating the wavelength stability of the microdisks allows us to estimate the refractive index limit of detection of the microdisks. Taking repeated wavelength scans

provides a direct method to estimate the uncertainty in mode wavelength by computing the variance between multiple scans. Further, averaging successive scans with a low-pass filter provides a method to reduce the uncertainty in wavelength measurement by removing the high-frequency stochastic error in each wavelength sweep. The wavelength stability can be improved upon by using the piezo-scan functionality of the tunable laser, sacrificing scan range, but increasing wavelength repeatability and allowing calibration with an external wavelength meter. Scanning a single mode of a 20 μm disk, as shown in Figure 6.5, allows wavelengths to be determined with a standard deviation of 0.1 pm over 20 minutes with a filter time constant of 30 s (33 mHz bandwidth). With a 20 μm disk sensitivity of 230 ± 20 nm/RIU, this sensitivity corresponds to a three-standard-deviation[166] detection limit of $(1.3 \pm 0.1) \times 10^{-6}$ RIU, or a LiCl concentration difference of $(1.5 \pm 0.1) \times 10^{-4}$ M.

Further work is required before these devices can be realized as useful sensors. In particular, we have not addressed specificity towards a particular molecule. Functionalization of the nitride surface [167] may provide a solution, but it is unknown how it will affect optical Qs or how the bulk index sensitivity will translate into attached molecule sensitivity. Nonetheless, extension of aqueous sensing into the visible regime, through the use of thin silicon nitride microdisks and visible-light dimpled-tapered fibers, may allow for easing of the technical requirements in sensing applications, such as the use of cheap diodes and spectrometers for visible wavelengths.

Future improvements should focus on fluid handling. Currently, non-homogenous mixing of solute, long timescales for mixing, and solvent evaporation create uncertainty in solute concentration. Additionally, mechanical disturbances of the pipette breaking the water surface may contribute to uncertainty in the mode wavelength. Therefore integration into a fluid-handling system, such as by using microfluidic devices [158], will be beneficial.
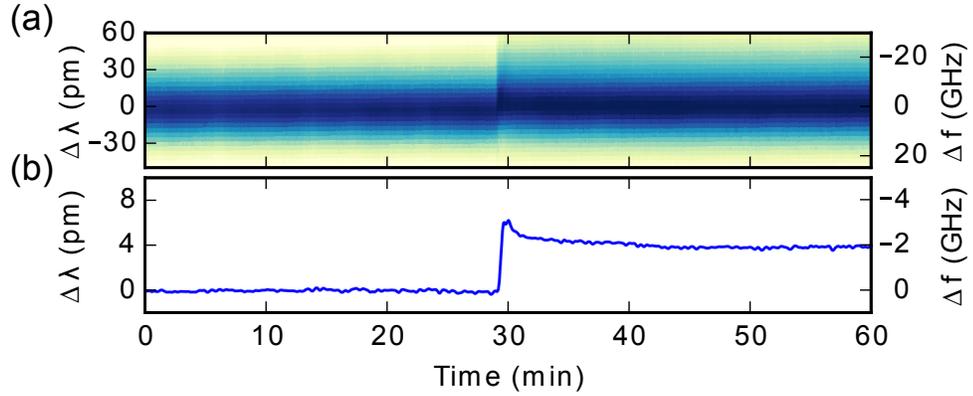
Figure 6.5: (a) Using the piezo scan functionality of the laser allows for better spectral resolution at the expense of scanning range. (b) After subtraction of a constant background slope, the wavelength of a mode can be tracked with a standard deviation of 0.1 pm. At 30 minutes LiCl was added to the sample cell resulting in a 1.5×10^{-5} RIU change, with large signal to noise.

The thin Si_3N_4 microdisks we have presented are an attractive option for future whispering gallery mode sensors. The planar configuration allows for mass fabrication and the possibility of integration with lab-on-a-chip technologies. Sensitivities of > 200 nm/RIU are observed, comparable with previously described slot resonators but with lessened fabrication requirements, while maintaining loaded Qs of $> 10^4$.

Chapter 7

Digital signal processing for experimental physics

7.1 Introduction

Experimental physics has evolved a lot over the past decades. When Dr. John Davis first joined his lab as a graduate student in 2001, recording charts were still in use. Now graduate students can easily fill up terabytes of disk space recording what is now considered low-bandwidth data over moderate time periods. Consider recording a 100 MHz bandwidth signal at a sample size of 2 bytes/sample. That is 400 MB of data every second, and 1.4 TB of data for an hour of data collection.

The upside to this is a completely configurable analysis chain. Even months after running the experiment, fundamental analysis parameters such as frequencies of interest, bandwidths of measurements, or recovering phase information in a signal can be extracted from the original data. Conversely, the sheer amount of data and possible operations on it are enough to overwhelm any analyzer of the data, and a relatively fixed signal processing pathway providing low bandwidth, but more easily read and interpreted feedback, can be indispensable.

In either case, the standard is to record all measurements as digital data stored on computers, which will be analyzed later using the preferred programming language such as MATLAB, Python or R. Unfortunately, methods to process these data are not taught to general physics students and instead remains a somewhat obscure subject somewhere between engineering and computer science.

For instance, intuitively a student may know they want to "smooth" the data, however the programming language and numerical analysis package used may not provide a `smooth` function. What is in fact desired is to apply a digital low-pass filter to the data to remove signal power at high-frequencies.

Throughout my graduate degree, I have found much benefit from learning about digital signal processing techniques and believe many physics students would likewise benefit from a quick introduction to various basic concepts. I attempt do that here, starting with a brief introduction to the theory behind digital signal processing without getting bogged down on the mathematical rigor. Hopefully this will help explain the use of signal processing software packages without getting too far into the gritty details.

Most of this information I have learned from two excellent books on digital signal processing, *Digital Signal Processing: Principles, Algorithms and Applications* by John G. Proakis and Dimitri G. Manolakis, and *Digital Signal Processing* (later re-titled *Discrete-Time Signal Processing*) by Alan V. Oppenheim and Ronald W. Schafer [168, 169]. Although much of this chapter is a summarized review of existing material, Section 7.4.2 presents original work on the design of quadratic-phase FIR filters.

7.2 Digital signal processing theory

7.2.1 Digital signals

As physicists, we model physical processes occurring in the world as continuous functions of time that can take on all numbers, even irrational ones. Pi is one of our favorite numbers. We call such a continuous function an analog signal. However, when storing these numbers on a computer, they must be discretized in both time and value to some finite representation.

If we have some continuous physical quantity $x(t)$, we can digitize the signal with an analog-to-digital converter—sampling at evenly spaced samples spaced T_s seconds apart—to find the digital signal

$$x[n] = Q\big\{x(T_s n)\big\}. \tag{7.1}$$

Here Q here refers to a quantization operation, truncating the value $x(T_s n)$ to some finite value that can be stored in a handful of bytes on a computer. Additionally, we use square brackets as an allusion to the array indexing notation used in most popular programming languages, reminding us $x[n]$ is a digital signal, and n can take on only integer values. Since computers have finite memory, $x[n]$ will only have non-zero values for a finite range of n, and for all other values of n we set $x[n] = 0$.

7.2.2 Linear time-invariant systems

Given we have a signal $x[n]$, we wish to perform some operation on it to produce a new digital signal $y[n]$. In a very general manner, we say a system $\mathcal{T}$ operates on $x[n]$ and produces $y[n]$. This operation can be represented mathematically as

$$y[n] = \mathcal{T}\big\{x[n]\big\}. \tag{7.2}$$

In general, $\mathcal{T}$ can perform any operation imaginable, as long as its output is a quantized, digital signal. However, from here on we are going to restrict $\mathcal{T}$ to a class of systems called linear time-invariant (LTI) systems. That is, $\mathcal{T}$ is both linear,

$$\mathcal{T}\{a_1 x_1[n] + a_2 x_2[n]\} = a_1 \mathcal{T}\{x_1[n]\} + a_2 \mathcal{T}\{x_2[n]\}, \qquad (7.3)$$

and time-invariant,

$$y[n - k] = \mathcal{T}\{x[n - k]\}, \qquad (7.4)$$

for all integer values of k. This restriction still represents a broad class of systems that exhibit useful mathematical properties making their use convenient for digital signal processing applications.

Most often, this system will perform a form of spectral filtering, such as removing high-frequency components of a signal—a low-pass filter—or perhaps retaining only frequency information within a certain bandwidth—a band-pass filter. As such, the terms system and filter will be used interchangeably to refer to any LTI system.

To begin describing how to work with LTI systems, let us first introduce the discrete δ function,

$$\delta[n] = \begin{cases} 1 & \text{if } n = 0 \\ 0 & \text{otherwise.} \end{cases} \qquad (7.5)$$

Using the δ function, it is possible to express $x[n]$ as a linear combination of δ functions spaced in time,

$$x[n] = \sum_{k=-\infty}^{\infty} x[k]\delta[n - k], \qquad (7.6)$$

84

where the sum is over all integer values of k. Substituting this expansion of $x[n]$ into equation (7.2) and using the linear properties of $\mathcal{T}$, we find

$$
\begin{aligned}
y[n] &= \mathcal{T}\left\{ \sum_{k=-\infty}^{\infty} x[k]\delta[n-k] \right\} \\
&= \sum_{k=-\infty}^{\infty} x[k]\mathcal{T}\{\delta[n-k]\}.
\end{aligned}
\tag{7.7}
$$

Here we introduce the unit impulse response of the system $\mathcal{T}$,

$$
h[n] = \mathcal{T}\{\delta[n]\}, \tag{7.8}
$$

such that

$$
y[n] = \sum_{k=-\infty}^{\infty} x[k]h[n-k], \tag{7.9}
$$

or noting that the sum on the right hand side is the convolution of $x[n]$ and $h[n]$,

$$
y[n] = x[n] * h[n], \tag{7.10}
$$

where $*$ denotes the convolution operation. That is, the LTI system $\mathcal{T}$ can be completely described by the system's response to a unit impulse, $h[n]$, while the operation of applying the system $\mathcal{T}$ to the signal $x[n]$ can be done via a convolution of $x[n]$ with $h[n]$.

Causal systems

Although the idea of finding the impulse response $h[n]$ to completely describe any LTI system is simple and succinct, we run into two practical problems for many types of LTI systems described this way. The first is causality. When running a system in

real time, the most recent output of the system, $y[n]$, can only depend on values of $x[n]$ that have been measured. Therefore, for a system to be causal, $h[n]$ must be zero for all values of $n < 0$.

In the case of post-analysis of data, as often done in research environment, the requirement of causality is not that important, since future values of the input $x[n]$ have already been measured. This situation allows the use of acausal filters, which can exhibit desirable properties, to be designed and used. However, for the most part we restrict our analysis of systems here to causal ones.

The second practical issue is the size of $h[n]$. In general, and for a wide class of useful LTI systems, the unit impulse response function can contain an infinite number of elements, presenting obvious problems when trying to represent the filter on a finite-memory computer. Therefore, we can broadly classify LTI systems into two categories: infinite impulse response (IIR) systems, in which $h[n]$ contains an infinite number of elements, and finite impulse response (FIR) systems that have finite-length $h[n]$. IIR systems are typically digital models of analog filter systems, and despite the infinite length of $h[n]$, can often be numerically more efficient to realize as explained in the next section. However, FIR filters can be digitally designed to conform to strict requirements, such as linear phase, or exact frequency cutoff characteristics.

7.2.3 The finite-difference equation

We will now introduce a further formalism for describing LTI systems: the finite-difference equation. A slightly smaller class of LTI systems can be described in the following manner:

$$\sum_{j=0}^{N} a_j y[n-j] = \sum_{k=0}^{M} b_k x[n-k]. \tag{7.11}$$

Here with have restricted ourselves to causal systems, *ie.* $y[n]$ only depends on $x[n-k]$, $k \geq 0$, and for systems that can be expressed with a finite number of a_j and b_k coefficients.

If we further restrict $a_0 = 1$, which can be obtained by renormalization of the other coefficients, a recipe for the computation of $y[n]$ can be found:

$$y[n] = b_0 x[n] + b_1 x[n-1] + ... + b_M x[n-M]$$
$$- a_1 y[n-1] - ... - a_N y[n-N]. \tag{7.12}$$

This equation is the foundation for digital signal processing on the computer, whereby a huge variety of causal filters can be represented through a set of a_j and b_k coefficients.

To illustrate an important effect of the a_j and b_k components, let us consider a simple example system with $b_0 = 1$, $a_0 = 1$, $a_1 = A$, and all other coefficients set to 0. That is

$$y[n] = x[n] + Ay[n-1]. \tag{7.13}$$

Further, we set $x[n] = \delta[n]$, and we assume $y[n] = 0$ for all values of $n < 0$. Then we proceed iteratively,

$$y[0] = x[0]$$
$$y[1] = Ax[0]$$
$$y[2] = A^2 x[0] \tag{7.14}$$
$$...$$
$$y[n] = A^n x[n].$$

Since we are computing the response to the unit impulse, $y[n]$ is $h[n]$—the unit impulse response—and as we can see, it contains an infinite number of elements. Which leads

us to the first important fact: systems that can be expressed as a finite-difference equation containing at least one non-zero a_j term, besides a_0, are IIR systems.

As can be seen in the above example, despite having an infinitely long unit impulse response, IIR systems can be succinctly described by just a small number of unique coefficients. Additionally, they can be computationally quite efficient: computation of $y[n]$ in the example above requires just two multiplications and an addition.

However, because of their recursive nature, numerical instabilities and errors can result as terms approach the machine epsilon—the smallest representable number in the computer. Additionally, the recursive nature of the algorithm prevents much parallelization of filter computation: $y[n-1]$ must be determined before $y[n]$ can be computed. This requirement is not a problem when run on basic microcontrollers, but modern processors contain vector math units able to perform many operations at once. For example, the AVX2 instructions present in most modern desktop processors manufactured since about 2014 are able to multiply eight 32-bit floating point numbers simultaneously [170], yet are generally unable to speed up computation of the finite-difference equation expressed above.

In contrast to the situation of IIR systems described above, we can conversely state that an LTI system that can be expressed with a finite-difference equation in which all a_js are zero, except $a_0 = 1$, is a finite impulse response system.

Applying the unit impulse function to equation (7.12), it is easy to see that the unit impulse response is

$$h[n] = \begin{cases} b_n & \text{if } 0 \leq n \leq M \\ 0 & \text{otherwise.} \end{cases} \tag{7.15}$$

That is, when describing a FIR filter, the unit impulse response *is* the b_k coefficients, and the computation of the finite-difference equation as in equation (7.12) is a convolution sum.

Although, in general, many more coefficients are required for a given filter cutoff response characteristic, FIR filters are useful in many situations. Not being recursive in nature, the numerical errors in filter computation can be much better estimated, and as mentioned previously exact filter characteristics can be designed. Further, because each calculation of $y[n]$ is independent of $y[m], m \neq n$, the computation of $y[n]$ can be easily parallelized. If $y[n]$ is only required to be calculated for a small set of n, such as in downsampling applications, FIR filters can be numerically more efficient for certain cases.

7.2.4 The Z-transform

An important tool in digital signal processing is the Z-transform. The Z-transform is analogous to the Laplace transform in continuous systems, but for discrete signals, and it provides a method for visualizing and thinking about discrete LTI systems along with some mathematically useful tools for analysis of discrete signals [168, 169]. Perhaps most relevant, the Z-transform is a generalization of the discrete Fourier transform, so all the tools learned will apply when working with the frequency-space representation of a discrete signal.

The Z-transform of a digital signal $x[n]$, $X(z) = \mathcal{Z}\{x[n]\}$, is a continuous complex-valued function of a complex variable z:

$$X(z) = \mathcal{Z}\{x[n]\} = \sum_{n=-\infty}^{\infty} x[n]z^{-n}. \tag{7.16}$$

The first thing to note is that $X(z)$ is not defined on the entire imaginary plane. If $x[n]$ is nonzero for any $n > 0$, $X(z)$ will be undefined at $z = 0$. Similarly, if $x[n]$ is nonzero for any $n < 0$, $X(z)$ will become non-finite as $z \to \infty$. The area on the imaginary plane that the z-transform is finite valued in is called the region of convergence—RoC.

For a finite-length signal, $z = 0$ and $|z| = \infty$ are the only two locations that may not converge. For an infinite length, let us examine the sequence in equation (7.14),

$$x[n] = \begin{cases} A^n & \text{if } n \geq 0 \\ 0 & \text{otherwise.} \end{cases} \tag{7.17}$$

Then the Z-transform of $x[n]$, $X(z)$ is

$$\begin{aligned} X(z) &= \sum_{n=0}^{\infty} A^n z^{-n} \\ &= \sum_{n=0}^{\infty} (Az^{-1})^n \\ X(z) &= \frac{1}{1 - Az^{-1}}, \end{aligned} \tag{7.18}$$

where we have used the infinite geometric series sum for the final simplification. This infinite sum, however, is only valid for $|Az^{-1}| < 1$. Thus the RoC of $X(z)$ is $|z| > |A|$.

Although we won't prove it here, it is possible to show that the Z-transform of the digital signal,

$$x_2[n] = \begin{cases} A^n & \text{if } n < 0 \\ 0 & \text{otherwise,} \end{cases} \tag{7.19}$$

is *also* $X_2(z) = 1/(1 - Az^{-1})$, however in this case the ROC is $|z| < |A|$. This illustrates two important facts of the Z-transform; the first: a digital signal is uniquely defined from its Z-transform only if both the Z-transform *and* the region of convergence is specified. Secondly, for a causal signal—$x[n] = 0, n < 0$—the region of convergence is exterior to some radius R, while for an acausal signal—$x[n] = 0, n \geq 0$—the RoC is interior to some radius R. For a signal $x[n]$ containing nonzero values for $n < 0$ and $n \geq 0$, there exists some ring on the imaginary plane, $R_1 < |z| < R_2$, where the Z-transform will converge.

Properties of the Z-transform

The Z-transform exhibits a number of mathematical properties worth describing. For proofs on these properties, see the textbooks on this subject recommended in the introduction [168, 169], or any other good reference on the Z-transform.

Linearity: If $x_1[n]$ has the Z-transform $\mathcal{Z}\{x_1[n]\} = X_1(z)$, and $x_2[n]$ has the Z-transform $\mathcal{Z}\{x_2[n]\} = X_2(z)$, then

$$\mathcal{Z}\{a_1 x_1[n] + a_2 x_2[n]\} = a_1 X_1(z) + a_2 X_2(z). \tag{7.20}$$

Time-shift: If $x[n]$ has the Z-transform $\mathcal{Z}\{x[n]\} = X(z)$, then

$$\mathcal{Z}\{x[n-k]\} = X(z)z^{-k}. \tag{7.21}$$

Scaling: If $x[n]$ has the Z-transform $\mathcal{Z}\{x[n]\} = X(z)$, then

$$\mathcal{Z}\{a^n x[n]\} = X(a^{-1}z). \tag{7.22}$$

Time-reversal: If $x[n]$ has the Z-transform $\mathcal{Z}\{x[n]\} = X(z)$, then

$$\mathcal{Z}\{x[-n]\} = X(z^{-1}). \tag{7.23}$$

Convolution: If $x_1[n]$ has the Z-transform $\mathcal{Z}\{x_1[n]\} = X_1(z)$, and $x_2[n]$ has the Z-transform $\mathcal{Z}\{x_2[n]\} = X_2(z)$, and $x_1[n] * x_2[n]$ denotes the convolution of $x_1[n]$ and $x_2[n]$, then

$$\mathcal{Z}\{x_1[n] * x_2[n]\} = X_1(z)X_2(z). \tag{7.24}$$

7.2.5   The system function

Recalling from equation (7.10) that the output of an LTI system can be found by the convolution of its unit impulse response with the input to the system, $y[n] = x[n] * h[n]$, we can use the convolution property of the Z-transform to find

$$Y(z) = X(z)H(z), \tag{7.25}$$

and therefore

$$H(z) = \frac{Y(z)}{X(z)}, \tag{7.26}$$

where $Y(z)$, $X(z)$, and $H(z)$ are the Z-transforms of $y[n]$, $x[n]$, and $h[n]$ respectively. Here, $H(z)$ is called the system function of the LTI system with unit impulse response $h[n]$.

Now, let us inspect the finite-difference equation given in equation (7.11), and apply the Z-transform to both sides,

$$\mathcal{Z}\left\{ \sum_{j=0}^{j=N} a_j y[n-j] \right\} = \mathcal{Z}\left\{ \sum_{k=0}^{k=M} b_k x[n-k] \right\}, \tag{7.27}$$

using the linearity and time-shift properties of the Z-transform we find

$$\sum_{j=0}^{j=N} a_j X(z) z^{-j} = \sum_{k=0}^{k=M} b_k X(z) z^{-k}, \tag{7.28}$$

which can be rearranged to find the system transfer function of the finite-difference equation:

$$H(z) = \frac{Y(z)}{X(z)} = \frac{\displaystyle\sum_{k=0}^{M} b_k z^{-k}}{\displaystyle\sum_{j=0}^{N} a_j z^{-j}}. \tag{7.29}$$

Thus, for LTI system defined as a finite-difference equation with a_j and b_k coefficients, we can easily construct its Z-transform. Conversely, and perhaps more important, if we are given an LTI system with a system function that can be written as in equation (7.29), we can extract the a_j and b_k coefficients to realize the LTI system using a finite-difference equation that is easily programmed.

Finally, for a system function that can be written as a fraction of two polynomials in z, it is possible to factor the polynomials to find the poles—locations which the function goes to infinity— and zeros—location which the function goes to zero—in a form such as

$$H(z) = G\frac{\displaystyle\prod_{k=0}^{M}(1 - z_k z^{-1})}{\displaystyle\prod_{j=0}^{N}(1 - p_j z^{-1})},\tag{7.30}$$

where z_k are the zeros and p_j are the poles of $H(z)$.

7.2.6 The discrete Fourier transform

We recall the Z-transform of the signal $x[n]$, $X(z)$, is given by equation (7.16),

$$X(z) = \mathcal{Z}\{x[n]\} = \sum_{n=-\infty}^{\infty} x[n]z^{-n}.\tag{7.31}$$

If we evaluate the Z-transform on the unit circle of the complex plane, that is for $z = e^{i\omega}$, and limit the sum to the N samples $x[n]$ is nonzero for, we find

$$X(e^{i\omega}) = \sum_{n=0}^{N-1} x[n]e^{-i\omega n}.\tag{7.32}$$

This equation is strikingly similar to the discrete Fourier transform, yet generalized for continuous values of ω along the unit circle of the Z-transform.

By sampling at N evenly spaced points around the unit circle, $\omega_k = 2\pi k/N$, we find the discrete Fourier transform (DFT):

$$X[k] = X(e^{i\omega_k}) = \sum_{n=0}^{N-1} x[n]e^{-i2\pi kn/N}. \qquad (7.33)$$

Here we have introduced the notation $X[k]$, referring to the DFT of $x[n]$, a digital signal sampled at the N points $z_k = e^{i2\pi k/N}$ from the continuous Z-transform of $x[n]$, $X(z)$.

Therefore, everything we have described for the Z-transform of $x[n]$ applies to the DFT of $x[n]$. The DFT *is* the Z-transform, but evaluated only at N discrete complex points on the unit circle, rather than valid throughout the entire region of convergence. As a corollary, once we claim the DFT of $x[n]$ exists, we automatically assume the RoC to contain the unit circle.

7.3 Some applications of digital signal processing

7.3.1 Spectral filtering

Now that we have laid the groundwork, we can discuss how we use digital filters for applications. The way we use filters in digital signal processing can be divided into three parts: filter design, parameter extraction and system abstraction, and filter realization—applying the filters.

Filter design and generalization

We will not attempt to describe filter design in any detail, however to illustrate the basics, we will describe two trivial filters that can be designed by intuition and used without any knowledge of digital signal processing—the box FIR filter, and the exponentially decaying IIR filter.

The box filter is a FIR low-pass filter made by averaging M sequential samples together. Practically everyone has designed and implemented this filter through averaging subsequent numbers together. In a more formal sense, the filter can be described by the unit impulse response:

$$h_{\text{box}}[n] = \begin{cases} 1/M & \text{if } 0 \leq n < M \\ 0 & \text{otherwise.} \end{cases} \tag{7.34}$$

To convert this filter into a_j and b_k representation, remember the b_k values are the unit impulse response, that is $b_k = h[k]$, and $a_0 = 1$, $a_j = 0$, when $j \neq 0$.

Next up is the exponentially decaying IIR filter. This filter is created by taking a real valued r with $|r| < 1$ and constructing the finite difference equation

$$y[n] = rx[n] + (1 - r)y[n - 1]. \tag{7.35}$$

This filter intuitively makes sense by updating the best guess of $x[n]$, $y[n]$ as a weighted average of the last best guess, $y[n - 1]$, and the newest measurement, which we expect to be noisy, $x[n]$. Equivalently, in terms of equation (7.12), $b_0 = r$, $a_0 = 1$, $a_1 = -(1 - r)$ and all other a_j and b_k's are equal to zero. The value of r can be found from the 3 dB cutoff frequency, f_{3dB}, and the sample spacing T_s, through the formula

$$r = e^{-2\pi T_s f_{\text{3dB}}}. \tag{7.36}$$

Figure 7.1 illustrates both the box filter with $M = 4$, and the exponential decay filter with $f_{\text{3dB}} = 10$ kHz. In both cases a sample-rate of 100 kSamples/s is used for illustration. Both filters display comparable, yet different, frequency responses, however the FIR box filter requires four multiplication and additions per sample to compute, while the exponential IIR filter requires two. This computational differ-

ence is easily made up if, for instance, a modern cpu is able to vectorize the FIR computation but not the IIR difference equation.

With both these example filters, the a_j and b_k coefficients are readily extractable from the design method. However, an alternate design method is manual placement of poles and zeros on the imaginary plane to design an LTI system with the desired frequency (and phase) response. Once the poles and zeros have been placed, a system function in the form of equation (7.30) can be written, and expanded out to a rational function with polynomials of z^{-1} in the numerator and denominator, in a form equivalent to equation (7.29). From here the a_j and b_k coefficients can be read to give a general description of the filter.

Although many recipes for various types of filter design exist, we will simply suggest using the filter design functions of an existing signal processing library, such as `scipy.signal`. Two filters, both with a cutoff of 10 kHz, are designed and shown in Figure 7.1. The first, a FIR filter constructed with `scipy.signal.firwin`, uses 50 coefficients and containing 49 zeros in the Z-transform. The second, a Butterworth IIR filter constructed with the `scipy.signal.butter` function, of order 8, contains eight poles and eight zeros in its Z-transform. Both these design functions return a list of a_j and b_k coefficients which can later be used without regard to the initially requested filter characteristics.

Filter realization

Once a filter has been described as a_j and b_k coefficients, a finite-difference equation can be constructed to realize the filter. This finite-difference equation can be programmed on a computer relatively easily, and is completely agnostic as to wether the filter high-passes or low-passes, the filter bandwidth, etc..

The `scipy.signal.lfilter` function is one such function that can apply an LTI system represented as a_j and b_k components to a signal, which can apply for either a
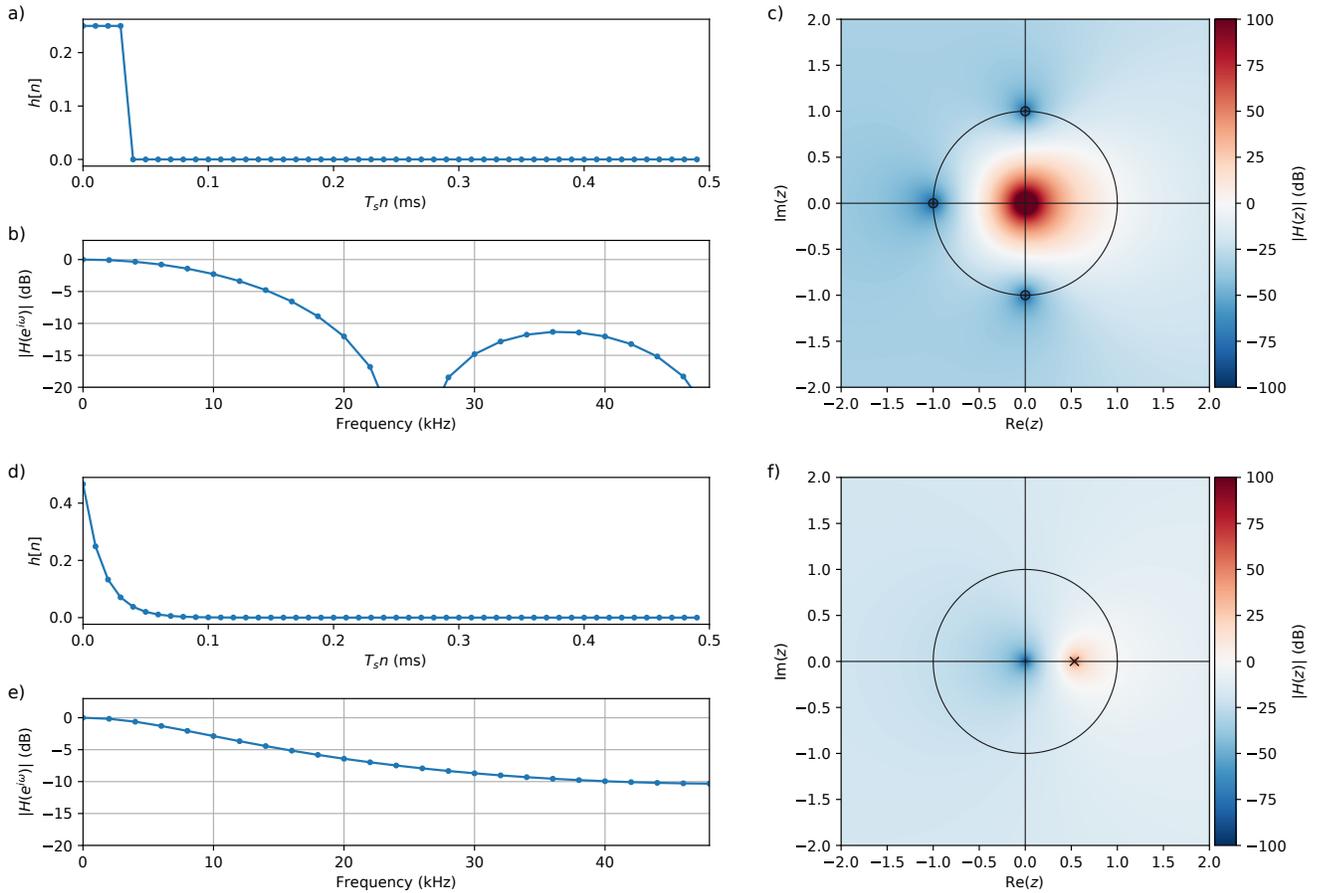
Figure 7.1: a) The unit impulse response, b) the amplitude transfer function, and c) the Z-transform of a FIR filter representing the average of four samples. Circles in c) point out locations of zeros in the system function. Similarly d) the unit impulse response, e) the amplitude transfer function, and f) the Z-transform of a simple exponential IIR filter described in the text. Crosses in f) locate poles in the transfer function.
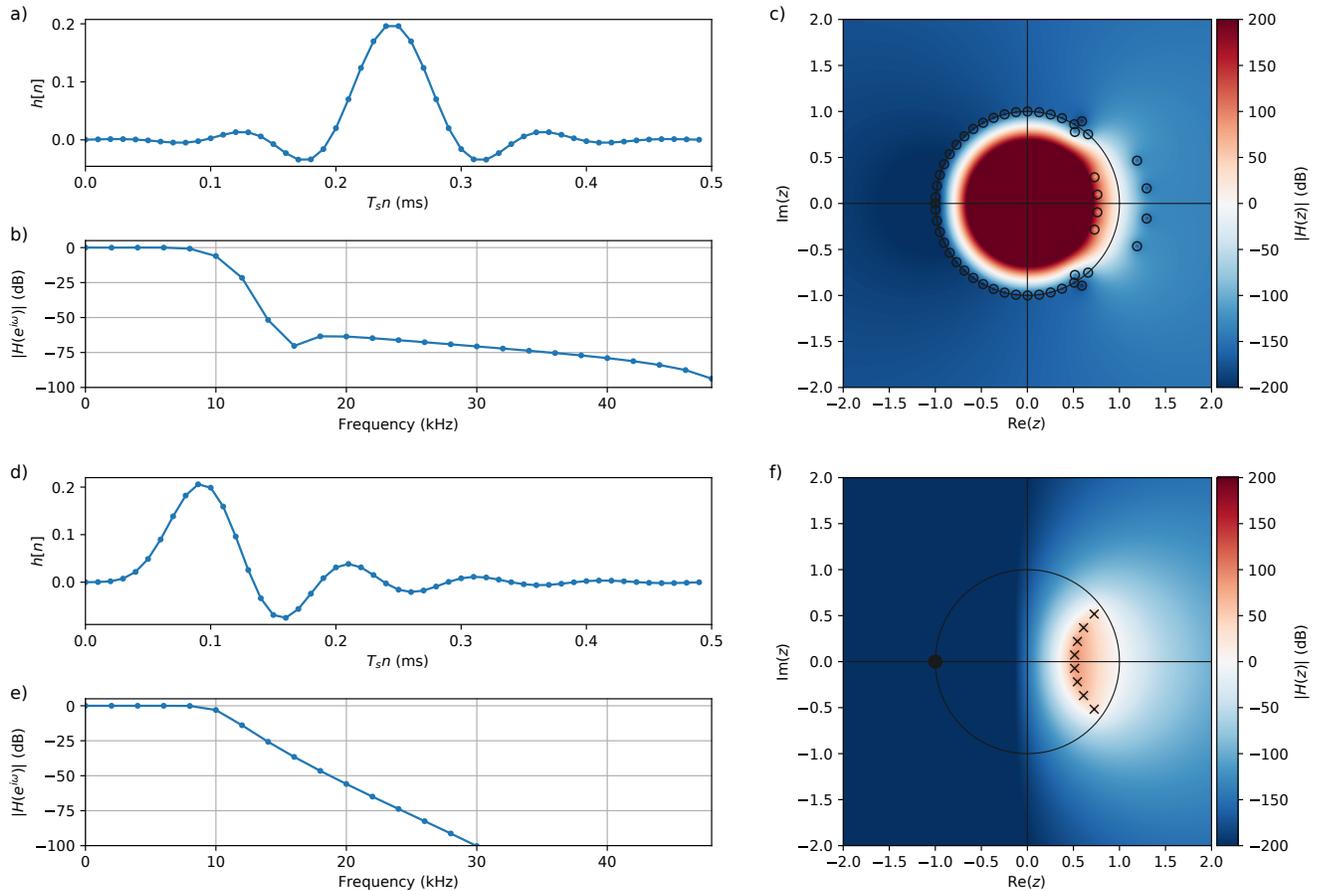
Figure 7.2: a) The unit impulse response, b) the amplitude transfer function, and c) the Z-transform of a 50 sample FIR filter created using the `scipy.signal.firwin` function. Circles in c) point out locations of zeros in the system function. Similarly d) the unit impulse response, e) the amplitude transfer function, and f) the Z-transform of an 8th-order Butterworth filter designed with `scipy.signal.butter` function. Circles in f) point out locations of zeros in the system function, while crosses locate poles in the transfer function.

FIR or IIR filter. However, in the case of a FIR filter, the finite-difference equation is exactly that of a convolution. Therefore, a FIR filter can be applied to a signal using either a convolution algorithm, such as `scipy.signal.convolve`, or a more general purpose finite-difference algorithm such as `scipy.signal.lfilter`.

7.3.2 Power spectral density estimation

One of the most basic tasks to do with a digital signal is to compute its power spectral density (PSD). The power spectral density of a signal is a spectral plot of the power in the signal per unit bandwidth. For instance, if a voltage signal is measured, the PSD will be in units of V^2/Hz, such that by multiplying the signal by a bandwidth will give the power of the signal—in this case given in units of V^2.

The power spectral density is an analog concept, such that ideally it is a continuous function of frequency. In digital signal processing we can find frequency information at discrete points by computing the Fourier transform of the signal, however since digital signals are often talked about in unitless terms, it is not completely obvious how to compute the PSD from a digital signal. In this section we will start from the continuous, analog definition of the power spectral density and discretize it to find how to compute it for a digital signal.

We are interested in estimating the power spectral density of a signal $x(t)$ sampled at discrete points in time $t_n = nT_s$ spaced at uniform intervals of T_s—the inverse sample-rate. In the continuous case, the power spectral density can be found by Fourier transforming the autocorrelation function of a signal—the Wiener-Khinchin theorem [171]. The time averaged continuous autocorrelation function is, approximately,

$$R_{\mathrm{x}}(\tau) = \frac{1}{T} \int_0^T x(t)x(t+\tau)\mathrm{d}t. \tag{7.37}$$

To be more precise, we should take the limit as $T \to \infty$, but since it is not possible to sample over time periods extending to infinity, we will use the given form for convenience, keeping in mind our goal is to *estimate* the PSD of our sampled signal. This estimation can be improved by averaging subsequent PSD estimates.

With the autocorrelation function determined, the PSD can be found by Fourier transforming it. If we assume our signal is periodic with a period T, the Fourier transform $X(\omega)$ of a periodic signal $x(t)$ is given by

$$X(\omega) = \int_0^T x(t)e^{-i\omega t}\mathrm{d}t. \tag{7.38}$$

Discretizing

To calculate the discrete case we will use forward Riemann sums. Given our signal is sampled N times over a time period T, such that samples are spaced in time by $T_s = T/N$, and each sample is indexed by n such that $x[n]$ is our estimate for $x(t)$ during the interval $t_n \leq t < t_{n+1}$, we can approximate

$$\int_0^T f(t)\mathrm{d}t \simeq \sum_{n=0}^{N-1} f[n]T_s. \tag{7.39}$$

Using this approximation we find for equation (7.37)

$$R_{\mathrm{x}}(m) \simeq \frac{1}{NT_s}\sum_{n=0}^{N-1} x[n]x[n+m]T_s, \tag{7.40}$$

and for equation (7.38)

$$\mathcal{F}_{\mathrm{k}}\{x(n)\} \simeq \sum_{n=0}^{N-1} x[n]e^{-i\omega_k n}T_s, \tag{7.41}$$

where $\omega_k = 2\pi k/N$ are the k frequencies we have chosen to evaluate the Fourier transform at as given in Section 7.2.6. Note that if we take $T_s \to 1$ we find the discrete autocorrelation and Fourier transform as often given.

All that is left to do is to put these equations together, such that the discrete Fourier transform of the discrete autocorrelation function is

$$
\begin{aligned}
S_{\mathrm{x}}[k] &= \sum_{m=0}^{N-1} e^{-i\omega_k m} T_s \ \frac{1}{NT_s} \sum_{n=0}^{N-1} x[n]x[n+m]T_s \\
&= \frac{T_s}{N} \sum_{n=0}^{N-1} e^{i\omega_k n} x[n] \sum_{m=0}^{N-1} e^{-i\omega_k(m+n)} x[m+n] \\
&= \frac{T_s}{N} X^*[k]X[k] \\
S_{\mathrm{x}}[k] &= \frac{T_s}{N} |X[k]|^2,
\end{aligned}
\tag{7.42}
$$

where $X[k]$ is the standard discrete Fourier transform as given by equation (7.33). We can note that T_s/N is the frequency spacing of the samples produced by the discrete Fourier transform, or the resolution bandwidth of the DFT. Therefore the PSD is found by taking the discrete Fourier transform of a signal, computing its amplitude squared—power—and dividing by the resolution bandwidth. Which seems obvious in hindsight.

One additional point is that of single-sided vs double-sided spectral densities. As given in equation (7.42), $S_{\mathrm{x}}[k]$ is normalized to the time-domain power via the discrete version of Parseval's theorem:

$$
T_s \sum_{n=0}^{N-1} |x[n]|^2 = \sum_{k=0}^{N-1} S_{\mathrm{x}}[k].
\tag{7.43}
$$

However, in the case of real valued $x[n]$, only floor$(N/2)+1$ coefficients of the Fourier transform are unique. This fact can be interpreted as the terms with $\pi < \omega_k < 2\pi$ corresponding to the negative frequencies $\omega_k - 2\pi$. It is often desirable to normalize the PSD such that only positive frequency terms are summed to match the power in

the time-series signal. If we define the single-sided PSD,

$$S_x^{ss}[k] = S_x[0]\delta[k] + S_x[N/2]\delta[k - N/2] + \sum_{j=1}^{N/2-1} 2S_x[k]\delta[k - j], \qquad (7.44)$$

where all the terms are doubled except for $\omega_k = 0$—and $\omega_k = \pi$ if N is even—the single-sided Parseval's theorem holds,

$$T_s \sum_{n=0}^{N-1} |x[n]|^2 = \sum_{k=0}^{N/2+1} S_x^{ss}[k], \qquad (7.45)$$

where S_x^{ss} is only summed over the floor$(N/2) + 1$ positive frequency components.

Finally, as alluded to earlier, the only way to compute the power spectrum exactly is to extend the autocorrelation function for all time periods extending to infinity. Therefore we are left to estimate the PSD. Computing one Fourier transform and normalizing it—sometimes referred to as a periodogram—is not a great estimate, and therefore we will introduce Bartlett's method for estimation of the PSD [172]. Bartlett's method suggests that when given a signal, $x[n]$ containing N samples, a better estimation of the PSD is made by dividing $x[n]$ into multiple sequential sequences with M samples each, such that $x_i[n] = x[iM + n]$. Then the periodogram of each sequence $x_i[n]$ can be computed and all averaged together to find a better estimate for the PSD of $x[n]$—at the expense of frequency resolution.

7.3.3 Software lock-in amplification

An instrument that is commonly used in experimental physics is the lock-in amplifier [173]. This instrument extracts a measurement from a noisy signal by isolating the signal of interest at a narrow band of frequencies around a frequency of interest, excluding the noise at all other frequencies. This operation is typically done with a

dedicated instrument, however the exact same operation can be performed digitally on a signal after capturing it with an analog-to-digital converter.

The signal processing done by a lock-in amplifier only takes a few steps. The signal of interest is first demodulated at the frequency of interest, effectively frequency shifting the signal to DC, and then low-passed filtered to remove high-frequency components. Finally the phase and amplitude of the signal can be extracted.

To perform lock-in amplification, the signal is first collected as the digital signal $x[n]$. This signal is typically a 1-channel voltage measurement and thus is real valued. To demodulate the signal at frequency f_0, the signal is multiplied by a complex sinusoidal signal $o[n] = e^{i2\pi f_0 T_s n}$, where f_0 is the demodulation frequency and T_s is the inverse sample rate, or sample spacing. Thus we compute the intermediate signal

$$
\begin{aligned}
y_0[n] &= x[n]o[n] \\
&= x[n]e^{-i2\pi f_0 T_s n},
\end{aligned}
\tag{7.46}
$$

where $y_0[n]$ is a complex signal containing the in-phase (I) and quadrature (Q) components in the real and imaginary parts, $i.e.$ acting as an IQ demodulator.

The oscillator signal, $o[n]$, is often output from a lock-in amplifier to provide drive of the system under test at the frequency of demodulation, therefore it may be useful to output this signal with a digital-to-analog converter, or with a separate function generator tuned to the same frequency. Further, $o[n] = e^{-i2\pi f_0 T_s n} = \cos(2\pi f_0 T_s n) - i\sin(2\pi f_0 T_s n)$ can be computed using the highly optimized sin and cos functions present in most programming languages, however in high-frequency real-time application the sin and cos values can be computed using a digital resonator filter [174], realizing $o[n] = (e^{-i2\pi f_0 T_s})^n$, or $o[n] = e^{-i2\pi f_0 T_s}o[n-1]$, requiring just one complex multiplication at each time step.

Next, the signal $y_0[n]$ is low-passed filtered to to remove frequency components away from the demodulation frequency f_0. Any FIR or IIR low-pass filter can be

103

used for this operation, and selection of the particular filter will be made based on performance and bandwidth characteristics. We will just say the signal is low-passed by the LTI system $\mathcal{L}$, such that we find the signal $y[n] = \mathcal{L}\{y_0[n]\}$, or

$$y[n] = \mathcal{L}\{x[n]e^{-i2\pi f_0 T_s n}\}. \tag{7.47}$$

Here $y[n]$ is the output of a lock-in amplifier. In the X, Y output of a lock-in amplifier, $X[n] = \mathrm{Re}(y[n])$, and $Y[n] = \mathrm{Im}(y[n])$, while in amplitude (R) and phase (ϕ) coordinates, $R[n] = |y[n]|$ and $\phi[n] = \arg(y[n])$.

7.4 Measuring a system response with a spread-spectrum drive

In a Section 7.3.2, we demonstrated how to estimate the power spectral density of a signal sampled as a digital time-series dataset. When measuring the power spectrum, we are already assuming some external power source is powering the measured signal. For instance, when measuring the thermomechanical motion of a nanomechanical cantilever, we are relying on the fact that thermal forces, constant across the frequency spectrum, are continually activating the mechanical motion of the cantilever in a way characterized by the mechanical susceptibility described earlier in Section 2.2.3.

However, it is often desirable to measure the response of a system in a controlled way such that both the phase and amplitude of the system function can be determined. One of the most straight-forward ways to achieve this is to generate a drive signal at specific frequency, and measure the response of the system to this drive signal. The response of an LTI system to a drive signal at a specific frequency is completely described by an amplitude and phase-shift of the drive signal. In practice, this response can be measured through the use of a lock-in amplifier—Section 7.3.3.

This drive signal can be swept over a discrete set of frequencies to map out the system response. However, determining the system response this way is a slow process, with only a very narrow bandwidth of the system being analyzed at a given time.

Instead of driving the system under test at a specific frequency, an alternative is to drive the system with a signal containing a flat frequency spectrum, for instance, with uncorrelated white noise or a delta function. However, because the drive power is so broadband, the power at any particular frequency ends up being quite low making good signal-to-noise measurements hard to realize. Instead, by driving the system with a drive pulse $d[n]$ containing an approximately flat power spectrum across only the frequency range of interest, drive power and therefore signal-to-noise can be better optimized.

Here we describe three methods to generate drive signals with an approximately flat power spectrum across a well-defined bandwidth of frequencies. This drive signal can be generated with the use of a digital-to-analog converter (DAC), applied to a system, and the response measured with an analog-to-digital converter (ADC). By computing the digital Fourier transform of both the drive, $D[n]$, and response, $Y[n]$, the system function $H[n] = Y[n]/D[n]$ can be constructed, revealing the phase and amplitude response of the system under test across the bandwidth of interest.

In this section, we will demonstrate the steps used to generate a drive pulse to measure the response of a system between 10 kHz and 20 kHz. We will use a sample rate of 100 kSamples/s, and aim for a resolution bandwidth of 100 Hz, such that the length of drive and response signal will need to be at least 10 ms in duration, or 1000 samples. These parameters were chosen to enable visualization of individual data points in the drive tone, yet containing enough datapoints for a fine-resolution image of the drive signal and spectral power of the drive. However these recipes can be adjusted for any combination of drive bandwidth, sample-rate, and resolution bandwidth requirements.

7.4.1 Linear phase FIR drive

For the first two methods, we will design a finite impulse response filter with the desired spectral characteristics, and then use the impulse response of the filter as the drive tone. For the first case, we will use the method of windowing to create a linear-phase FIR filter. This is a standard method of filter design implemented, for instance, by SciPy's `signal.firwin` and `signal.firwin2` functions and MATLAB's `fir1` and `fir2` functions.

The general method to create a FIR filter with a passband from ω_1 to ω_2 is as follows. We define the system function of the filter to be:

$$H(e^{i\omega}) = \begin{cases} e^{-i\omega M} & \text{if } \omega_1 \leq \omega \leq \omega_2 \\ 0 & \text{otherwise,} \end{cases} \tag{7.48}$$

such that the amplitude response of the filter is unity across the pass-band. The system function can then be inverse Fourier transformed to find the impulse response of the filter. In the continuous case—due to the perfectly sharp rising edge of the filter—the impulse response will be infinitely long, however it can be truncated to a finite length through the use of a window function, adding a transition width to the band edges and introducing ripple in the pass-band as a result of the Gibb's phenomena [169, 175].

The exact choice of window function presents a trade-off between the length of transition region at the band edge, and the amount of ripple introduced. However, for this study we will restrict ourselves to the use of the Hann window—a shifted and scaled cosine curve—due to its mathematical simplicity and relatively good spectral characteristics [176]. It is defined by

$$w[n] = \frac{1}{2}(1 + cos(\pi + 2\pi\frac{n}{N})), \tag{7.49}$$
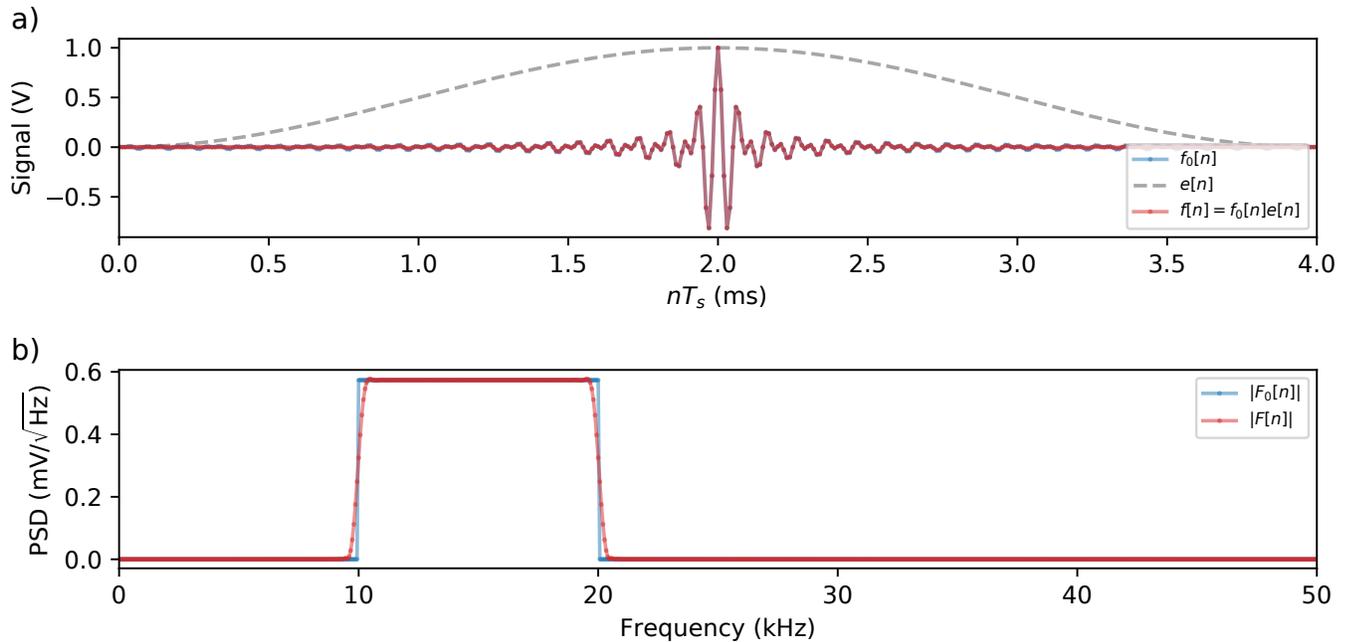
Figure 7.3: a) Time-series plot of the impulse response generated with the linear-phase FIR filter design method, $f[n]$ (blue). The ideal filter response $f_0[n]$ is enveloped with a 4 ms Hann window $e[n]$ (gray, dashed). Signals are normalized to a maximum field amplitude of ± 1 V. b) The power spectral density of the drive signals shown in a).

where $w[n]$ is the Hann window spaced across N samples.

To examine the choice of the phase for the filter described by equation (7.48), let us recall the time-shift property of the Z-transform (evaluated for $z = e^{i\omega}$):

$$\mathcal{Z}\{x[n-k]\} = \mathcal{Z}\{x[n]\}e^{-i\omega k}, \tag{7.50}$$

that is, the phase shift in equation (7.48), $e^{-i\omega M}$, is chosen such that the impulse response of the filter is delayed by M samples. This shift is done such that when we window the impulse response to $2M$ samples in length, the impulse response has no values at negative time periods and is therefore causal.

7.4.2 Quadratic phase FIR drive

Linear phase filters are often desired in signal-processing applications due to their constant delay across frequencies. However for our application of designing a drive pulse, the linear-phase filter presents a problem: most of the spectral power of the drive signal is located at the same location in time, causing a spike in the time-domain signal amplitude similar to a delta function.

Since the ability to generate a drive signal is usually limited by the maximum amplitude of a signal, a drive signal like that created with the linear-phase technique limits the average power in the drive signal. To navigate this limitation, we will design a quadratic-phase filter using the same approximate design methods as the linear phase filter, but with the characteristic of spreading out the spectral drive information over time such that larger average drive powers are possible.

To begin, we will introduce the idea of the group delay of a filter. If a filter has a phase response of $\phi(\omega)$, then the delay applied to a component of the signal with frequency ω, in samples, is [169, 177]

$$\tau_g(\omega) = -\frac{\partial \phi(\omega)}{\partial \omega}. \tag{7.51}$$

We can see that if we use the linear phase $\phi(\omega) = -\omega M$, a simple time delay of M samples expected, just as determined using the time-shift properties of the Z-transform.

We can use this to design the phase of the filter with a passband from ω_1 to ω_2 by requiring signals at ω_1 to be delayed to $M - D$ samples, while the signals at ω_2 are delayed to $M + D$ samples, such that the spectral band of the signal is spread over $2D$ samples centered at a delay of M samples. Starting with a quadratic phase ansatz of

$$\phi(\omega) = b\omega + c\omega^2, \tag{7.52}$$
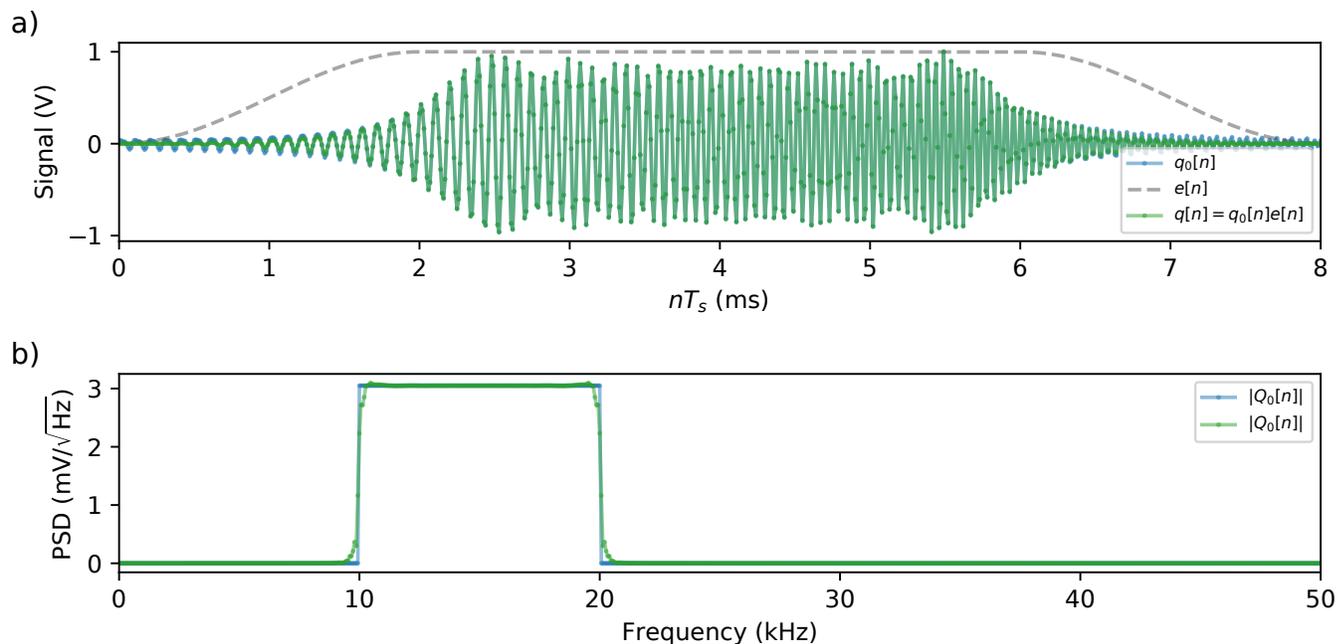
Figure 7.4: a) Time-series plot of the impulse response, $q[n]$ (blue), generated with the quadratic-phase FIR filter design method described in the text. The ideal filter response $q_0[n]$ is enveloped with $e[n]$ (gray, dashed). Signals are normalized to maximum field amplitude of ± 1 V. b) The power spectral density of the drive signals shown in a).

and requiring the conditions

$$\tau_g(\omega_1) = -b - 2c\omega_1 = M - D \tag{7.53}$$

$$\tau_g(\omega_2) = -b - 2c\omega_2 = M + D, \tag{7.54}$$

we find the desired phase of our filter

$$\phi_q(\omega) = -\left(M + \frac{D}{2}\frac{\omega_1 + \omega_2}{\omega_1 - \omega_2}\right)\omega + \frac{D}{\omega_1 - \omega_2}\omega^2. \tag{7.55}$$

Using this form for the phase of the filter response, we can construct the digital system function $H[k] = r[k]e^{i\phi(\omega_k)}$ and perform an inverse real digital Fourier transform to find the real-valued impulse response $h[n]$. This impulse response is then

109

enveloped with E samples on either side of the $2D$ region the drive signal is spread over such that the whole pulse is $2E + 2D = 2M$ samples long. Figure 7.4 illustrates such a quadratic drive signal.

7.4.3 Chirp drive

An alternative method to spreading the drive power out over time is to build a chirp filter. A chirp filter is very similar to the quadratic-phase filter just described, but constructed in the time-domain, rather than the frequency domain.

We begin by thinking about how the chirp filter should behave. If we imagine the chirp filter applied to a delta function, we expect the result to be a sine wave ramping in frequency from DC to the maximum frequency expressible by the sample rate, with a constant amplitude across frequencies. To construct the chirp, we will design what we expect the impulse response of the filter to look like.

First, we will introduce the idea of instantaneous frequency—somewhat analogous to the group delay used in designing the quadratic-phase filter. The instantaneous frequency of a signal $x(t) = A\cos(\phi(t))$ is $\Omega(t) = (\partial/\partial t)\phi(t)$ [178]. We want the instantaneous frequency of the impulse response to ramp from ω_0 to ω_1 over a period T, such that $\Omega(t) = \omega_0 + (\omega_1 - \omega_0)t$. Integrating $\Omega(t)$, we find

$$\phi(t) = \left(\omega_0 + \frac{1}{2}\frac{\omega_1 - \omega_0}{T}t\right)t + C.$$

(7.56)

Digitizing the signal with $t = nT_s$ and $T = NT_s$, and choosing C such the signal is 0 at $n = 0$, we can find the impulse response for our chirp as

$$c_0[n] = \sin\left(2\pi(f_0 + \frac{1}{2}\frac{f_1 - f_0}{N}n)nT_s\right),$$

(7.57)

where $f_i = 2\pi\omega_i$. For $f_0 = 8$ kHz and $f_1 = 22$ kHz, $c_0[n]$ and its spectral power are plotted in Figure 7.5.

110
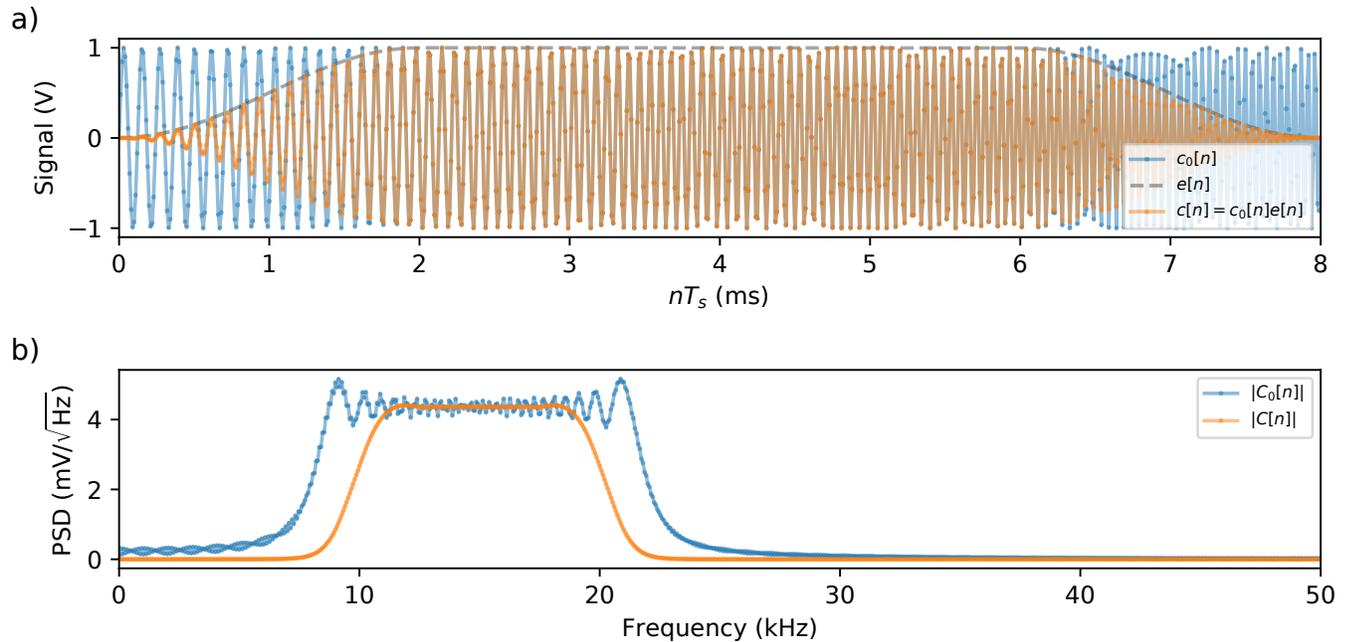
Figure 7.5: a) By ramping a sin wave from 8 kHz to 22 kHz instantaneous frequency a chirp function generated as $c_0[n]$ (blue). An envelope, $e[n]$ (gray dashed) is applied to reduce discontinuity at the beginning and end of the drive and resulting function $c[n]$ is shown in red. b) Power spectral density of drive signals plotted in a), computed by padding the drive signal to 15 ms with null signal increased frequency resolution. The envelope applied on the signal $c[n]$ with PSD $|C[n]|$ acts to smooth the signal in frequency-space reducing ripple in the drive band.

As can be seen in Figure 7.5, the chirped signal displays approximately the desired spectral frequency characteristics, however the drive band from 10 kHz - 20 kHz contains large ripples. To improve the ripple, the signal $c_0[n]$ can be enveloped. By enveloping $c_0[n]$ with a Hann window increasing (decreasing) over 2 ms at the beginning (end) of the chirp, the spectral characteristics are smoothed—Figure 7.5b.

Finally we can compare all three of the drives we have designed—Figure 7.6. Each drive was designed with a 2 ms rising and falling envelope, and designed to spread across a 8 ms drive length, with the exception of the linear-phase drive which we are unable to spread further across time. As shown in Figure 7.6b, the chirp drive achieves the most spectral power across the frequencies of interest, but the rising and falling edges of the passband are distributed across a wide range of frequencies,

111
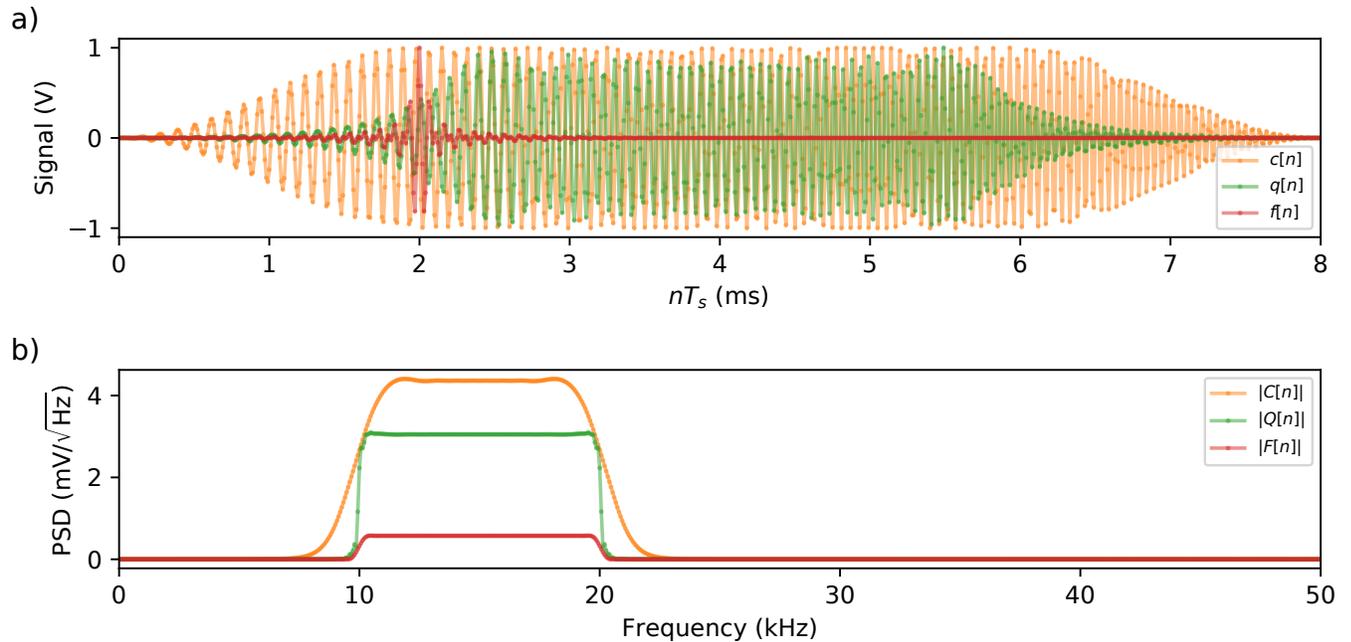
Figure 7.6:   a) By convoluting the FIR drive signal plotted in Figure 7.3 ($c[n]$, orange), and the chirped drive shown in Figure 7.5 ($c[n]$, red), a chirped FIR drive signal is produced (green) that is normalized to ± 1 V signal amplitude.   b) The power spectral density of the drive signals reveal the convoluted signal retains the same spectral shape as the FIR drive signal, but with average power almost reaching that of the chirped drive.

such that if sharp spectral shapes are required—for instance frequency responses approaching DC—a chirp drive may be a poor choice. The linear-phase drive achieves good spectral characteristics, but with significantly less drive power. The quadratic-phase filter retains much of the same spectral sharpness as the linear-phase drive, but is able to significantly more drive power, although not as much as the chirp drive.

7.5   Conclusion

We reviewed the basics of digital signal processing, aimed to help experimental physics researchers manipulate their data in powerful ways. The core approach is the framing of an operation as a linear time-invariant system. LTI systems represent a wide variety

of operations, including low-pass, band-pass, and high-pass filters which can be used to judiciously isolate signals from noise within a particular bandwidth of interest.

The Z-transform, a generalization of the discrete Fourier transform, provides a tool for manipulation of discrete LTI systems between their various representations. The system function of an LTI system provides the familiar frequency dependent amplitude and phase transfer-function depiction of a filter, while the finite-difference equation form gives an algorithmically implementable realization of the system. With these tools in hand, common measurement instruments such as a spectrum analyzer—used to compute the power spectral density of a signal—or a lock-in-amplifier—used to measure the system response to a sinusoidal tone—can be readily implemented in software.

Finally, we introduced a technique for driving a system with a broadband pulse, such that the system function can be determined in a more efficient manner than through amplitude and phase responses to individual sinusoidal drive tones. Three different methods for generating a broadband drive tone with sharply defined spectral characteristics were presented, such that fast time-resolved measurements of the transfer-function of an experimental system can be made.

Chapter 8

Conclusion

The silicon and silicon nitride optical and mechanical resonators measured in this thesis show promise as precise measurement devices to measure force and refractive index. Because they are fabricated from a single layer of material, the devices are robust and relatively easy to fabricate using either advanced photolithographic processes as done in Chapters 3 and 4, or through electron beam lithography as done in Chapters 5 and 6. Therefore the extension of these devices—either using optomechanical detection for high-sensitivity readout of a mechanical resonator, or using the optical resonators as refractive index sensors themselves—to commercial devices should be able to be navigated in a fairly straight-forward manner.

In Chapter 2, we developed the background theory of optical microdisks and mechanical resonators showing how mechanical resonators will fundamentally act as force sensors, with particularly high force sensitivity at AC frequencies around their mechanical resonance frequency. In the study of the interaction between optical and mechanical cavities—optomechanics—we developed a novel theoretical method of analyzing optomechanical systems in the bad-cavity limit: the regime where optical dissipation happens at a rate much quicker than the mechanical motion. This regime presents an accessible, well understood parameter space where optomechani-

cal cavities can act as precision displacement sensors of nanomechanical devices. In Chapter 3, we demonstrated the detection of femtogram mass cantilevers at 2.0 ± 0.6 fm Hz$^{-1/2}$ which achieve room temperature, thermal limited force sensing of 130 ± 40 aN Hz$^{-1/2}$. This detection is achieved in the directly detected, tuned-to-the-slope optomechanical detection scheme which does not require any additional expensive and bulky optical components required by, for instance, homodyne detection setups.

When measuring the silicon cantilevers, we observed a signal at exactly twice the mechanical resonator frequency, indicating a nonlinear transduction processes which we further inquired in Chapter 4. One sought-after goal in fundamental mechanical resonator research is to measure direct jumps in phonon number between Fock states—a key signature of quantum behavior. To perform these measurements, a particular type of measurement—a quantum non-demolition measurement—is required, and is expected to be able to be achieved through non-linear measurement of position arising from second order optomechanical coupling. Using the bad-cavity limit optomechanical theory we developed, we were able to show that it was nonlinearities elsewhere in the optical transduction, and not more fundamental phonon-number coupling to the optical resonator, causing the nonlinear transduction. However in doing so we presented a path forward in the characterization of optomechanical devices which may be able to perform such measurements.

In Chapter 5, we demonstrated that the same optical microdisk detection of nanomechanical resonators observed in silicon works just as well for devices fabricated out of silicon nitride. The high-stress silicon nitride that results from LPCVD deposition of stoichiometric silicon nitride resulted in the fabrication of nanostrings with picogram effective masses and high quality factors. We were able to fiber-waveguide these devices to create an integrated robust package that was able to withstand cooling to sub-kelvin temperatures, and due to relatively small optically induced heating, present a promising platform for future cryogenic optomechanical experiments.

In Chapter 6, we showed silicon nitride microdisks act well as sensors without being paired with nanomechanical devices. In water, where mechanical motion would be substantially damped, the refractive index sensing ability of the top-down fabricated microdisk reached the limit of detection approaching 10^{-6} refractive index units.

Although not well recognized, digital signal processing has become a foundation for experimental work in physics. In Chapter 7 we reviewed the basics of digital signal processing and explore the ways in which filters and LTI systems can be manipulated for signal processing applications. We introduced the basics of signal measurement tools such as the spectrum analyzer and lock-in amplifier, and presented a broadband drive technique for the determination of the system function of an experimental device. Recipes for the generation of drive signals were developed, with trade-offs between ease-of-implementation, the precision of spectral drive power, and the amplitude-limited average drive power. These drive tones have been used with great success in the measurement of superfluid helium Helmholtz resonators, which were otherwise outside of the scope of this thesis.

Put all together, the monolithically integrated optical and mechanical devices, the theory on optomechanical direct detection, and the know-how to extract meaningful signals from a noisy measured quantity via digital signal processing techniques, present a solid foundation to pursue further work in commercialization of these optomechanical sensors.

Bibliography

[1] K J Vahala. Optical microcavities. *Nature*, 424:839–846, 2003.

[2] J D Jackson. *Classical electrodynamics*, chapter 8. John Wiley & Sons, Inc., 1999.

[3] J D Joannopoulos, S G Johnson, J N Winn, and R D Meade. *Photonic Crystals: Molding the flow of light*. Princeton University Press, 2008.

[4] Baron Rayleigh and J W Strutt. *The theory of sound*, volume 2, chapter 14. Macmillan and Co., Ltd., 1896.

[5] D W Vernooy, V S Ilchenko, H Mabuchi, E W Streed, and H J Kimble. High-q measurements of fused-silica microspheres in the near infrared. *Opt. Lett.*, 23:247–249, 1998.

[6] AJR MacDonald, BD Hauer, X Rojas, PH Kim, GG Popowich, and JP Davis. Optomechanics and thermometry of cryogenic silica microresonators. *Physical Review A*, 93(1):013836, 2016.

[7] P.E. Barclay, K. Srinivasan, O. Painter, B. Lev, and H. Mabuchi. Integration of fiber-coupled high-q sinx microdisks with atom chips. *Appl. Phys. Lett.*, 89(13):131108, 2006.

[8] F. Vollmer, S. Arnold, and D. Keng. Single virus detection from the reactive shift of a whispering-gallery mode. *Proc. Natl. Acad. Sci.*, 105(52):20701–20704, 2008.

[9] M. S. McClellan, L. L. Domier, and R. C. Bailey. Label-free virus detection using silicon photonic microring resonators. *Biosens. Bioelectron.*, 31:388–392, 2012.

[10] M. R. Lee and P. M. Fauchet. Nanoscale microcavity sensor for single particle detection. *Opt. Lett.*, 32:3284–3286, 2007.

[11] Jiangang Zhu, Sahin Kaya Ozdemir, Yun-Feng Xiao, Lin Li, Lina He, Da-Ren Chen, and Lan Yang. On-chip single nanoparticle detection and sizing by mode splitting in an ultrahigh-q microresonator. *Nat. Photon.*, 4:46–49, 2010.

[12] S. I. Shopova, R. Rajmangal, Y. Nishida, and S. Arnold. Ultrasensitive nanoparticle detection using a portable whispering gallery mode biosensor driven by a periodically poled lithium-niobate frequency doubled distributed feedback laser. *Rev. Sci. Instr.*, 81:103110, 2010.

[13] T. Lu, H. Lee, T. Chen, S. Herchak, J. Kim, S. E. Fraser, R. C. Flagan, and K. Vahala. High sensitivity nanoparticle detection using optical microcavities. *Proc. Natl. Acad. Sci.*, 108:5976–5979, 2011.

[14] A. M. Armani, R. P. Kulkarni, S. E. Fraser, R. C. Flagan, and K. J. Vahala. Label-free, single-molecule detection with optical microcavities. *Science*, 317(5839):783–787, 2007.

[15] A. J. Qavi, T. M. Mysz, and R. C. Bailey. Isothermal discrimination of single-nucleotide polymorphisms via real-time kinetic desorption and label-free detection of dna using silicon photonic microring resonator arrays. *Anal. Chem.*, 83:6827–6833, 2011.

[16] M. D. Baaske, M. R. Foreman, and F. Vollmer. Single-molecule nucleic acid interactions monitored on a label-free microcavity biosensor platform. *Nat. Nanotech.*, 9:933–939, 2014.

[17] Genalyte. `https://www.genalyte.com/`. Online; accessed July 16, 2019.

[18] K. S. Thorne, R. W. P. Drever, C. M. Caves, M. Zimmermann, and V. D. Sandberg. Quantum nondemolition measurements of harmonic oscillators. *Phys. Rev. Lett.*, 40:667–671, 1978.

[19] V. B. Braginsky, Y. I. Vorontsov, and K. S. Thorne. Quantum nondemolition measurements. *Science*, 209:547–557, 1980.

[20] J. D. Teufel, T. Donner, M. A. Castellanos-Beltran, J. W. Harlow, and K. W. Lehnert. Nanomechanical motion measured with an imprecision below that at the standard quantum limit. *Nat. Nanotech.*, 4:820–823, 2009.

[21] B. D. Hauer, C. Doolin, K. S. D. Beach, and J. P. Davis. A general procedure for thermomechanical calibration of nano/micro-mechanical resonators. *Ann. Phys.*, 339:181–207, 2013.

[22] C Doolin, PH Kim, BD Hauer, AJR MacDonald, and JP Davis. Multidimensional optomechanical cantilevers for high-frequency force sensing. *New Journal of Physics*, 16(3):035001, 2014.

[23] Ultraview. `http://www.ultraviewcorp.com/`. Online; accessed July 16, 2019.

[24] Zurich instruments. `https://www.zhinst.com/`. Online; accessed July 16, 2019.

[25] Resolved instruments. `https://resolvedinstruments.com/`. Online; accessed July 16, 2019.

[26] M. Li, H. X. Tang, and M. L. Roukes. Ultra-sensitive nems-based cantilevers for sensing, scanned probe and very high-frequency applications. *Nature Nanotech.*, 2:114–120, 2007.

[27] M Belov, N J Quitoriano, S Sharma, W K Hiebert, T I Kamins, and S Evoy. Mechanical resonance of clamped silicon nanowires measured by optical interferometry. *J. Appl. Phys.*, 103:074304, 2008.

[28] B Sanii and P D Ashby. High sensitivity deflection detection of nanowires. *Phys. Rev. Lett.*, 104:147203, 2010.

[29] D Ramos, E Gil-Santos, O Malvar, J M Llorens, V Pini, A S Paulo, M Calleja, and J Tamayo. Silicon nanowires: where mechanics and optics meet at the nanoscale. *Sci. Rep.*, 3:3445, 2013.

[30] T. Fukuma. Wideband low-noise optical beam deflection sensor with photothermal excitation for liquid-environment atomic force microscopy. *Rev. Sci. Instrum.*, 80:023707, 2009.

[31] H. I. Rasool, P. R. Wilkinson, A. Z. Stieg, and J. K. Gimzewski. A low noise all-fiber interferometer for high resolution frequency modulated atomic force microscopy imaging in liquids. *Rev. Sci. Instrum.*, 81:023703, 2010.

[32] G. Anetsberger, O. Arcizet, Q. P. Unterreithmeier, Q. P. Rivière, A. Schliesser, E. M. Weig, J. P. Kotthaus, and T. J. Kippenberg. Near-field cavity optomechanics with nanomechanical oscillators. *Nature Phys.*, 5:909–914, 2009.

[33] P. H. Kim, C. Doolin, B. D. Hauer, A. J. R. MacDonald, M. R. Freeman, P. E. Barclay, and J. P. Davis. Nanoscale torsional optomechanics. *Appl. Phys. Lett.*, 102:053102, 2013.

[34] H.A. Haus. *Waves and fields in optoelectronics*. Prentice Hall, Incorporated, 1984.

[35] R.P. Feynman, R.B. Leighton, and M.L. Sands. *The Feynman Lectures on Physics*. Addison-Wesley Publishing Company, 1963.

[36] M D Sturge. *Statistical and Thermal Physics: Fundamentals and Applications*. A K Peters, Natick, Massachusetts, 2003.

[37] Peter R Saulson. Thermal noise in mechanical experiments. *Physical Review D*, 42(8):2437, 1990.

[38] MV Salapaka, HS Bergh, J Lai, A Majumdar, and E McFarland. Multi-mode noise analysis of cantilevers for scanning probe microscopy. *Journal of Applied Physics*, 81(6):2480–2487, 1997.

[39] Markus Aspelmeyer, Tobias J Kippenberg, and Florian Marquardt. Cavity optomechanics. *Reviews of Modern Physics*, 86(4):1391, 2014.

[40] G. Binnig, C. F. Quate, and C. Gerber. Atomic force microscope. *Phys. Rev. Lett.*, 56:930–933, 1986.

[41] F. J. Giessibl. Atomic resolution of the silicon (111)-(7x7) surface by atomic force microscopy. *Science*, 267:68–71, 1995.

[42] L. Gross, F. Mohn, N. Moll, P. Liljeroth, and G. Meyer. The chemical structure of a molecule resolved by atomic force microscopy. *Science*, 325:1110–1114, 2009.

[43] T. Fukuma, K. Kobayashi, K. Matsushige, and H. Yamada. True molecular resolution in liquid by frequency-modulation atomic force microscopy. *App. Phys. Lett.*, 86:193108, 2005.

[44] S. Sharma, H. Zhu, E. E. Grintsevich, E. Reisler, and J. K. Gimzewski. Correlative nanoscale imaging of actin filaments and their complexes. *Nanoscale*, 5:5692–5702, 2013.

[45] D. J. Müller and Y. F. Dufrane. Atomic force microscopy as a multifunctional molecular toolbox in nanobiotechnology. *Nature Nanotech.*, 3:261–269, 2008.

[46] M. B. Viani, L. I. Pietrasanta, J. B. Thompson, Ch, A, I. C. Gebeshuber, J. H. Kindt, M. Richter, H. G. Hansma, and P. K. Hansma. Probing protein-protein interactions in real time. *Nature Struct. Biol.*, 7:644–647, 2000.

[47] M. Rief, M. Gautel, F. Oesterhelt, Fern, J. M. ez, and H. E. Gaub. Reversible unfolding of individual titin immunoglobulin domains by afm. *Science*, 276:1109–1112, 1997.

[48] David J Brockwell, Emanuele Paci, Rebecca C Zinober, Godfrey S Beddard, Peter D Olmsted, D Alastair Smith, Richard N Perham, and Sheena E Radford. Pulling geometry defines the mechanical resistance of a β-sheet protein. *Nature Structural & Molecular Biology*, 10(9):731, 2003.

[49] T. Ando, N. Kodera, E. Takai, D. Maruyama, K. Saito, and A. Toda. A high-speed atomic force microscope for studying biological macromolecules. *Proc. Natl. Acad. Sci.*, 98:12468–12472, 2001.

[50] T. Uchihashi, R. Iino, T. Ando, and H. Noji. High-speed atomic force microscopy reveals rotary catalysis of rotorless f_1-atpase. *Science*, 333:755–758, 2011.

[51] I. Casuso, P. Sens, F. Rico, and S. Scheuring. Experimental evidence for membrane-mediated protein-protein interaction. *Biophys. J.*, 99:L47–L49, 2010.

[52] M. Endo, K. Hidaka, KatoT, K. Namba, and H. Sugiyama. Dna prism structures constructed by folding of multiple rectangular arms. *J. Am. Chem. Soc.*, 131:15570–15571, 2009.

[53] T. R. Albrecht, P. Grütter, D. Horne, and D. Rugar. Frequency modulation detection using high-q cantilevers for enhanced force microscope sensitivity. *J. App. Phys.*, 69:668–673, 1991.

[54] E. Gavartin, P. Verlot, and T. J. Kippenberg. A hybrid on-chip optomechanical transducer for ultrasensitive force measurements. *Nature Nanotech.*, 7:509–514, 2012.

[55] H. J. Mamin and D. Rugar. Sub-attonewton force detection at millikelvin temperatures. *Appl. Phys. Lett.*, 79:3358, 2001.

[56] S. S. Verbridge, R. Ilic, H. G. Craighead, and J. M. Parpia. Size and frequency dependent gas damping of nanomechanical resonators. *Appl. Phys. Lett.*, 93:013101, 2008.

[57] K Jensen, Kwanpyo Kim, and A Zettl. An atomic-resolution nanomechanical mass sensor. *Nature nanotechnology*, 3(9):533, 2008.

[58] Joel Moser, J Güttinger, Alexander Eichler, María J Esplandiu, DE Liu, MI Dykman, and Adrian Bachtold. Ultrasensitive force detection with a nanotube mechanical resonator. *Nature nanotechnology*, 8(7):493, 2013.

[59] J. M. Nichol, E. R. Hemesath, L. J. Lauhon, , and R. Budakian. Displacement detection of silicon nanowires by polarization-enhanced fiber-optic interferometry. *Appl. Phys. Lett.*, 93:193110, 2008.

[60] Christoph Reinhardt, Tina Müller, Alexandre Bourassa, and Jack C Sankey. Ultralow-noise sin trampoline resonators for sensing and optomechanics. *Physical Review X*, 6(2):021001, 2016.

[61] Madhav Kumar and Harish Bhaskaran. Ultrasensitive room-temperature piezoresistive transduction in graphene-based nanoelectromechanical systems. *Nano letters*, 15(4):2562–2567, 2015.

[62] K. L. Ekinci and M. L. Roukes. Nanoelectromechanical systems. *Rev. Sci. Instrum.*, 76:061101, 2005.

[63] T. J. Kippenberg and K. J. Vahala. Cavity opto-mechanics. *Opt. Express*, 15:17172–17205, 2007.

[64] M. Eichenfield, R. Camacho, J. Chan, K. J. Vahala, and O. Painter. A picogram- and nanometre-scale photonic-crystal optomechanical cavity. *Nature*, 459:550–555, 2009.

[65] G. Anetsberger, E. Gavartin, O. Arcizet, Q. P. Unterreithmeier, E. M. Weig, M. L. Gorodetsky, J. P. Kotthaus, and T. J. Kippenberg. Measuring nanomechanical motion with an imprecision below the standard quantum limit. *Phys. Rev. A*, 82:061804, 2010.

[66] C. P. Michael, M. Borselli, T. J. Johnson, C. Chrystal, and O. Painter. An optical fiber-taper probe for wafer-scale microphotonic device characterization. *Optics Express*, 15:4745–4752, 2007.

[67] K. Srinivasan, H. Miao, M. T. Rakher, M. Davanço, and V. Aksyuk. Optomechanical transduction of an integrated silicon cantilever probe using a microdisk resonator. *Nano Lett.*, 11:791–797, 2011.

[68] Y. Liu, H. Miao, V. Aksyuk, and K. Srinivasan. Wide cantilever stiffness range cavity optomechanical sensors for atomic force microscopy. *Optics Express*, 20:18268–18280, 2012.

[69] Richard A Norte, Joao P Moura, and Simon Gröblacher. Mechanical resonators for quantum optomechanics experiments at room temperature. *Physical review letters*, 116(14):147202, 2016.

[70] Amir H Ghadimi, Sergey A Fedorov, Nils J Engelsen, Mohammad J Bereyhi, Ryan Schilling, Dalziel J Wilson, and Tobias J Kippenberg. Elastic strain engineering for ultralow mechanical dissipation. *Science*, 360(6390):764–768, 2018.

[71] O. Arcizet, P. F. Cohadon, T. Briant, M. Pinard, and A. Heidmann. Radiation-pressure cooling and optomechanical instability of a micromirror. *Nature*, 444:71–74, 2006.

[72] C Doolin, BD Hauer, PH Kim, AJR MacDonald, H Ramp, and JP Davis. Nonlinear optomechanics in the stationary regime. *Physical Review A*, 89(5):053838, 2014.

[73] J. D. Teufel, T. Donner, M. A. Castellanos-Beltran, J. W. Harlow, and K. W. Lehnert. Nanomechanical motion measured with an imprecision below that at the standard quantum limit. *Nature Nano.*, 4:820–823, 2009.

[74] G. Anetsberger, E. Gavartin, O. Arcizet, Q. P. Unterreithmeier, E. M. Weig, M. L. Gorodetsky, J. P. Kotthaus, and T. J. Kippenberg. Measuring nanomechanical motion with an imprecision below the standard quantum limit. *Phys. Rev. A*, 82:061804, 2010.

[75] K. C. Schwab and M. L. Roukes. Putting mechanics into quantum mechanics. *Physics Today*, 58:36–42, 2005.

[76] A. A. Clerk, M. H. Devoret, S. M. Girvin, F. Marquardt, and R. J. Schoelkopf. Introduction to quantum noise, measurement and amplification. *Rev. Mod. Phys.*, 82:1155, 2010.

[77] Y. Chen. Macroscopic quantum mechanics: theory and experimental concepts of optomechanics. *J. Phys. B: At. Mol. Opt. Phys.*, 46:104001, 2013.

[78] V. B. Braginskii and Yu. I. Vorontsov. Quantum-mechanical limitations in macroscopic experiments and modern experimental technique. *Sov. Phys. Usp.*, 17:644, 1975.

[79] V. B. Braginskii, Yu. I. Vorontsov, and F. Ya. Khalili. Quantum singularities of a ponderomotive meter of electromagnetic energy. *Sov. Phys. JETP*, 46:705, 1977.

[80] W. G. Unruh. Analysis of quantum-nondemolition measurement. *Phys. Rev. D*, 18:1764, 1978.

[81] J. Chan, T. P. Mayer Alegre, A. H. Safavi-Naeini, J. T. Hill, A. Krause, S. Gröblacher, M. Aspelmeyer, and O. Painter. Laser cooling of a nanomechanical oscillator into its quantum ground state. *Nature*, 478:89–92, 2011.

[82] J. D. Teufel, T. Donner, D. Li, J. W. Harlow, M. S. Allman, K. Cicak, A. J. Sirois, J. D. Whittaker, K. W. Lehnert, and R. W. Simmonds. Sideband cooling of micromechanical motion to the quantum ground state. *Nature*, 475:359–363, 2011.

[83] A. D. O'Connell, M. Hofheinz, M. Ansmann, R. C. Bialczak, M. Lenander, E. Lucero, M. Neeley, D. Sank, H. Wang, M. Weides, J. Wenner, J. M. Martinis, and A. N. Cleland. Optomechanical crystals. *Nature*, 464:697–703, 2010.

[84] A. H. Safavi-Naeini, J. Chan, J. T. Hill, Thiago P. Mayer Alegre, A. Krause, and O. Painter. Observation of quantum motion of a nanomechanical resonator. *Phys. Rev. Lett.*, 108:033602, 2012.

[85] N. Brahms, T. Botter, S. Schreppler, D. W. C. Brooks, and D. M. Stamper-Kurn. Optical detection of the quantization of collective atomic motion. *Phys. Rev. Lett*, 108:133601, 2012.

[86] T. A. Palomaki, J. D. Teufel, R. W. Simmonds, and K. W. Lehnert. Entangling mechanical motion with microwave fields. *Science*, 342:710–713, 2013.

[87] S. Peil and G. Gabrielse. Observing the quantum limit of an electron cyclotron: Qnd measurements of quantum jumps between fock states. *Phys. Rev. Lett.*, 83:1287–1290, 1999.

[88] W. H. Zurek. Decoherence and the transition from quantum to classical. *Physics Today*, 44:36–44, 1991.

[89] W. H. Zurek. Decoherence, einselection, and the quantum origins of the classical. *Rev. Mod. Phys.*, 75:715–775, 2003.

[90] V. B. Braginsky and F. Ya. Khalili. *Quantum Measurement*. Cambridge University Press, Cambridge, UK, 1992.

[91] D. H. Santamore, A. C. Doherty, and M. C. Cross. Quantum nondemolition measurement of fock states of mesoscopic mechanical oscillators. *Phys. Rev. B*, 70:144301, 2004.

[92] J. B. Hertzberg, T. Rocheleau, T. Ndukum, M. Savva, A. A. Clerk, and K. C. Schwab. Back-action-evading measurements of nanomechanical motion. *Nature Phys.*, 6:213–217, 2010.

[93] S. K. Steinke, K. C. Schwab, and P. Meystre. Optomechanical backaction-evading measurement without parametric instability. *Phys. Rev. A*, 88:023838, 2013.

[94] Alex Szorkovszky, Aashish A Clerk, Andrew C Doherty, and Warwick P Bowen. Detuned mechanical parametric amplification as a quantum non-demolition measurement. *New Journal of Physics*, 16(4):043023, 2014.

[95] A. A. Gangat, T. M. Stace, and G. J. Milburn. Phonon number quantum jumps in an optomechanical system. *New Journal of Physics*, 13:043024, 2011.

[96] J. D. Thompson, B. M. Zwickl, A. M. Jayich, F. Marquardt, S. M. Girvin, and J. G. E. Harris. Strong dispersive coupling of a high-finesse cavity to a micromechanical membrane. *Nature*, 452:72–76, 2008.

[97] A. Nunnenkamp, K. Borkje, J. G. E. Harris, and S. M. Girvin. Cooling and squeezing via quadratic optomechanical coupling. *Phys. Rev. A*, 82:021806(R), 2010.

[98] S. Huang and G. S. Agarwal. Cooling and squeezing via quadratic optomechanical coupling. *Phys. Rev. A*, 83:023823, 2011.

[99] K. Borkje, A. Nunnenkamp, J. D. Teufel, and S. M. Girvin. Signatures of nonlinear cavity optomechanics in the weak coupling regime. *Phys. Rev. Lett.*, 111:053603, 2013.

[100] J. C. Sankey, C. Yang, B. M. Zwickl, A. M. Jayich, and J. G. E. Harris. Strong and tunable nonlinear optomechanical coupling in a low-loss system. *Nature Phys.*, 6:707–712, 2010.

[101] NE Flowers-Jacobs, SW Hoch, JC Sankey, A Kashkanova, AM Jayich, C Deutsch, J Reichel, and JGE Harris. Fiber-cavity-based optomechanical device. *Applied Physics Letters*, 101(22):221109, 2012.

[102] D Lee, M Underwood, D Mason, AB Shkarin, SW Hoch, and JGE Harris. Multimode optomechanical dynamics in a cavity with avoided crossings. *Nature communications*, 6:6232, 2015.

[103] H. Miao, S. Danilishin, T. Corbitt, and Y. Chen. Standard quantum limit for probing mechanical energy quantization. *Phys. Rev. Lett.*, 103:100402, 2009.

[104] J. T. Hill. Nonlinear optics and wavelength translation via cavity optomechanics. *Nonlinear optics and wavelength translation via cavity optomechanics. Ph.D. Thesis (California Inst. of Tech.)*, 2013.

[105] Hamidreza Kaviani, Chris Healey, Marcelo Wu, Roohollah Ghobadi, Aaron Hryciw, and Paul E Barclay. Nonlinear optomechanical paddle nanocavities. *Optica*, 2(3):271–274, 2015.

[106] Taofiq K Paraïso, Mahmoud Kalaee, Leyun Zang, Hannes Pfeifer, Florian Marquardt, and Oskar Painter. Position-squared coupling in a tunable photonic crystal optomechanical cavity. *Physical Review X*, 5(4):041024, 2015.

[107] PZG Fonseca, EB Aranas, J Millen, TS Monteiro, and PF Barker. Nonlinear dynamics and strong cavity cooling of levitated nanoparticles. *Physical review letters*, 117(17):173602, 2016.

[108] H. Rokhsari, T. J. Kippenberg, T. Carmon, and K. J. Vahala. Radiation-pressure-driven micro-mechanical oscillator. *Optics Express*, 13:5293–5301, 2005.

[109] Chenguang Huang, Jiahua Fan, Ruoyu Zhang, and Lin Zhu. Internal frequency mixing in a single optomechanical resonator. *Applied Physics Letters*, 101(23):231112, 2012.

[110] F. Liu and M. Hossein-Zadeh. On the spectrum of radiation pressure driven optomechanical oscillator and its application in sensing. *Optics Communications*, 294:338–343, 2012.

[111] C. H. Metzger and K. Karrai. Cavity cooling of a micro lever. *Nature*, 432:1002–1005, 2004.

[112] C. Metzger, I. Favero, A. Ortlieb, and K. Karrai. Optical self cooling of a deformable fabry-perot cavity in the classical limit. *Phys. Rev. B*, 78:035309, 2008.

[113] P. E. Barclay, K. Srinivasan, and O. Painter. Nonlinear response of silicon photonic crystal microresonators excited via an integrated waveguide and fiber taper. *Optics Express*, 13:801–820, 2005.

[114] C. P. Michael, M. Borselli, T. J. Johnson, C. Chrystal, and O. Painter. An optical fiber-taper probe for wafer-scale microphotonic device characterization. *Optics Express*, 15:4745–4752, 2007.

[115] B. D. Hauer, P. H. Kim, C. Doolin, A. J. R. MacDonald, H. Ramp, and J. P. Davis. On-chip cavity optomechanical coupling. *EPJ Tech. Instrum.*, 1:4, 2014.

[116] M. S. Bartlett. Smoothing periodograms from time-series with continuous spectra. *Nature*, 161:686–687, 1948.

[117] F. Marquardt, A. A. Clerk, and S. M. Girvin. Quantum theory of optomechanical cooling. *Journal of Modern Optics*, 55:3329–3338, 2008.

[118] A. A. Clerk, Florian Marquardt, and J. G. E. Harris. Quantum measurement of phonon shot noise. *Phys. Rev. Lett.*, 104:213603, 2010.

[119] BD Hauer, A Metelmann, and JP Davis. Phonon quantum nondemolition measurements in nonlinearly coupled optomechanical cavities. *Physical Review A*, 98(4):043804, 2018.

[120] A. Schliesser, R. Rivière, G. Anetsberger, O. Arcizet, and T. J. Kippenberg. Resolved-sideband cooling of a micromechanical oscillator. *Nature Phys.*, 88:415–419, 2008.

[121] S. Gröblacher, J. B. Hertzberg, M. R. Vanner, G. D. Cole, S. Gigan, K. C. Schwab, and M. Aspelmeyer. Quantum measurement of phonon shot noise. *Nature Phys.*, 5:485–488, 2009.

[122] H. Tan, F. Bariani, G. Li, and P. Meystre. Generation of macroscopic quantum superpositions of optomechanical oscillators by dissipation. *Phys. Rev. A*, 88:023817, 2013.

[123] Mingyun Yuan, Martijn A Cohen, and Gary A Steele. Silicon nitride membrane resonators at millikelvin temperatures with quality factors exceeding 108. *Applied Physics Letters*, 107(26):263501, 2015.

[124] Ralf Riedinger, Andreas Wallucks, Igor Marinković, Clemens Löschnauer, Markus Aspelmeyer, Sungkun Hong, and Simon Gröblacher. Remote quantum entanglement between two micromechanical oscillators. *Nature*, 556(7702):473, 2018.

[125] Amir H Safavi-Naeini, Simon Gröblacher, Jeff T Hill, Jasper Chan, Markus Aspelmeyer, and Oskar Painter. Squeezed light from a silicon micromechanical resonator. *Nature*, 500(7461):185, 2013.

[126] Thomas P Purdy, P-L Yu, RW Peterson, NS Kampel, and CA Regal. Strong optomechanical squeezing of light. *Physical Review X*, 3(3):031012, 2013.

[127] Emma Edwina Wollman, CU Lei, AJ Weinstein, J Suh, A Kronwald, F Marquardt, AA Clerk, and KC Schwab. Quantum squeezing of motion in a mechanical resonator. *Science*, 349(6251):952–955, 2015.

[128] Florent Lecocq, Jeremy B Clark, Raymond W Simmonds, Jose Aumentado, and John D Teufel. Quantum nondemolition measurement of a nonclassical state of a massive object. *Physical Review X*, 5(4):041037, 2015.

[129] Sungkun Hong, Ralf Riedinger, Igor Marinković, Andreas Wallucks, Sebastian G Hofer, Richard A Norte, Markus Aspelmeyer, and Simon Gröblacher. Hanbury brown and twiss interferometry of single phonons from an optomechanical resonator. *Science*, 358(6360):203–206, 2017.

[130] AP Reed, KH Mayer, JD Teufel, LD Burkhart, W Pfaff, M Reagor, L Sletten, X Ma, RJ Schoelkopf, E Knill, et al. Faithful conversion of propagating quantum information to mechanical motion. *Nature Physics*, 13(12):1163, 2017.

[131] Justin D Cohen, Seán M Meenehan, and Oskar Painter. Optical coupling to nanoscale optomechanical cavities for near quantum-limited motion transduction. *Optics express*, 21(9):11227–11236, 2013.

[132] Alexander G Krause, Martin Winger, Tim D Blasius, Qiang Lin, and Oskar Painter. A high-resolution microchip optomechanical accelerometer. *Nature Photonics*, 6(11):768, 2012.

[133] Raphael St-Gelais, Simon Bernard, Christoph Reinhardt, and Jack C Sankey. Swept-frequency drumhead optomechanical resonators. *ACS Photonics*, 6(2):525–530, 2019.

[134] Seán M Meenehan, Justin D Cohen, Gregory S MacCabe, Francesco Marsili, Matthew D Shaw, and Oskar Painter. Pulsed excitation dynamics of an optomechanical crystal resonator near its quantum ground state of motion. *Physical Review X*, 5(4):041002, 2015.

[135] BD Hauer, PH Kim, C Doolin, F Souris, and JP Davis. Two-level system damping in a quasi-one-dimensional optomechanical resonator. *Physical Review B*, 98(21):214303, 2018.

[136] H Ramp, BD Hauer, KC Balram, TJ Clark, K Srinivasan, and JP Davis. Elimination of thermomechanical noise in piezoelectric optomechanical crystals. *Physical Review Letters*, 123(9):093603, 2019.

[137] Justin D Cohen. *Fiber-optic integration and efficient detection schemes for optomechanical resonators*. California Institute of Technology, 2015.

[138] TJ Kippenberg, SM Spillane, and KJ Vahala. Modal coupling in traveling-wave resonators. *Optics letters*, 27(19):1669–1671, 2002.

[139] AJR MacDonald, GG Popowich, BD Hauer, PH Kim, A Fredrick, X Rojas, P Doolin, and JP Davis. Optical microscope and tapered fiber coupling apparatus for a dilution refrigerator. *Review of Scientific Instruments*, 86(1):013107, 2015.

[140] PH Kim, BD Hauer, C Doolin, F Souris, and JP Davis. Approaching the standard quantum limit of mechanical torque sensing. *Nature communications*, 7:13165, 2016.

[141] Richard A Norte, Moritz Forsch, Andreas Wallucks, I Marinković, and Simon Gröblacher. Platform for measurements of the casimir force between two superconductors. *Physical review letters*, 121(3):030405, 2018.

[142] Herbert R Philipp. Optical properties of silicon nitride. *Journal of the Electrochemical Society*, 120(2):295–300, 1973.

[143] C Doolin, P Doolin, BC Lewis, and JP Davis. Refractometric sensing of li salt with visible-light si3n4 microdisk resonators. *Applied Physics Letters*, 106(8):081104, 2015.

[144] M. S. Luchansky and R. C. Bailey. High-q optical sensors for chemical and biological analysis. *Anal. Chem.*, 84:793–821, 2012.

[145] F. Vollmer and L. Yang. Label-free detection with high-q micro cavities: a review of biosensing mechanisms for integrated devices. *Nanophotonics*, 1:267–291, 2012.

[146] A Meldrum and F Marsiglio. Capillary-type microfluidic sensors based on optical whispering gallery mode resonances. *Rev. Nanosci. Nanotechnol.*, 3:193–209, 2014.

[147] N. M. Hanumegowda, C. J. Stica, B. C. Patel, I. White, and X. Fan. Refractometric sensors based on microsphere resonators. *Appl. Phys. Lett.*, 87(20):201107, 2005.

[148] J. Lutti, W. Langbein, and P. Borri. A monolithic optical sensor based on whispering-gallery modes in polystyrene microspheres. *Appl. Phys. Lett.*, 93(15):151103, 2008.

[149] J. D. Swaim, J. Knittel, and W. P. Bowen. Detection of nanoparticles with a frequency locked whispering gallery mode microresonator. *Appl. Phys. Lett.*, 102:183106, 2013.

[150] H. Li and X. Fan. Characterization of sensing capability of optofluidic ring resonator biosensors. *Appl. Phys. Lett.*, 97(1):011105, 2010.

[151] R. W. Boyd and J. E. Heebneer. Sensitive disk resonator photonic biosensor. *Appl. Opt.*, 40:5742–5747, 2001.

[152] A. Schweinsberg, S. Hoc, N. N. Lepeshkin, R. W. Boyd, C. Chase, and J. E. Fajardo. An environmental sensor based on an integrated optical whispering gallery mode disk resonator. *Sensor. Actuat. B-Chem.*, 123(2):727–732, 2007.

[153] M. Iqbal, M. A. Gleeson, B. Spaugh, F. Tybor, W. G. Gunn, M. Hochberg, T. Baehr-Jones, R. C. Bailey, and L. C. Gunn. Label-free biosensor arrays based on silicon ring resonators and high-speed optical scanning instrumentation. *IEEE J. Quantum Electron.*, 16:654–660, 2010.

[154] B. Su, C. Wang, Q. Kan, and C. HongDa. Compact silicon-on-insulator dual-microring resonator optimized for sensing. *J. Lightwave Technol.*, 29:1535–1541, 2011.

[155] C. Ciminelli, F. Dell'Olio, D. Conteduca, C.M. Campanella, and M.N. Armenise. High performance soi microring resonator for biochemical sensing. *Opt. Laser. Technol.*, 59(0):60–67, 2014.

[156] C. A. Barrios, K. B. Gylfason, B. Sánchez, A. Griol, H. Sohlström, M. Holgado, and R. Casquel. Slot-waveguide biochemical sensor. *Opt. Lett.*, 32:3080–3082, 2007.

[157] T. Claes, J.G. Molera, K. De Vos, E. Schachtb, R. Baets, and P. Bienstman. Label-free biosensing with a slot-waveguide-based ring resonator in silicon on insulator. *IEEE Photon. J.*, 1(3):197–204, Sept 2009.

[158] C. F. Carlborg, K. B. Gylfason, A. Kaźmierczak, F. Dortu, M. J. Bañuls Polo, A. Maquieira Catala, G. M. Kresbach, H. Sohlström, T. Moh, L. Vivien, J. Popplewell, G. Ronan, C. A. Barrios, G. Stemmea, and W. van der Wijngaart. A packaged optical slot-waveguide ring resonator sensor array for multiplex label-free assays in labs-on-chips. *Lab on a Chip*, 10:281–290, 2010.

[159] M. Adams, G. A DeRose, M. Loncar, and A. Scherer. Lithographically fabricated optical cavities for refractive index sensing. *J. Vac. Sci. Technol. B*, 23:3168–3173, 2005.

[160] C. Baker, S. Stapfner, D. Parrain, S. Ducci, G. Leo, E. M. Weig, and I. Favero. Optical instability and self-pulsing in silicon nitride whispering gallery resonators. *Opt. Express*, 20:29076–29089, 2012.

[161] D. J. Moss, R. Morandotti, A. L. Gaeta, and M. Lipson. New cmos-compatible platforms based on silicon nitride and hydex for nonlinear optics. *Nature Photonics*, 7:597–607, 2013.

[162] M. Eichenfield, C. P. Michael, R. Perahia, and O. Painter. Actuation of micro-optomechanical systems via cavity-enhanced optical dipole forces. *Nature Photonics*, 1:416–422, 2007.

[163] A. Ksendzov and Y. Lin. Integrated optics ring-resonator sensors for protein detection. *Opt. Lett.*, 30:3344–3346, 2005.

[164] W. M. Haynes, editor. *CRC Handbook of Chemistry and Physics*. CRC Press, 95 edition, 2014.

[165] M. Oxborrow. Traceable 2-d finite-element simulation of the whispering-gallery modes of axisymmetric electromagnetic resonators. *IEEE Trans. Microw. Theory Techn.*, 55:1209–1218, 2007.

[166] I M White and X Fang. On the performance quantification of resonant refractive index sensors. *Opt. Express*, 16:1020–1028, 2008.

[167] M. Bañũls, V. González-Pedro, C. A. Barrios, R. Puchades, and Á. Maquieira. Selective chemical modification of silicon nitride/silicon oxide nanostructures to develop label-free biosensors. *Biosens. Bioelectron.*, 25:1460–1466, 2010.

[168] Alan V. Oppenheim and Ronald W. Schafer. *Digital signal processing.* Englewood Cliffs, N. J.: Prentice-Hall, 1975.

[169] John G. Proakis and Dimitris G. Manolakis. *Digital signal processing : principles, algorithms, and applications, 2nd ed.* New York: Macmillan, 1992.

[170] Mark Buxton. Haswell new instruction descriptions now available!, 2001–. Online; accessed May 14 2019.

[171] Daniel T Gillespie. The mathematics of brownian motion and johnson noise. *American Journal of Physics*, 64(3):225–240, 1996.

[172] MS Bartlett. Smoothing periodograms from time-series with continuous spectra. *Nature*, 161(4096):686, 1948.

[173] Walter C Michels and Norma L Curtis. A pentode lock-in amplifier of high frequency selectivity. *Review of Scientific Instruments*, 12(9):444–447, 1941.

[174] Sen M. Kuo, Bob H. Lee, and Wenshun Tian. *Real-time digital signal processing : implementations and applications, 2nd ed.* Chichester, England: John Wiley, 2006.

[175] J Willard Gibbs. Fourier's series. *Nature*, 59(1522):200, 1898.

[176] Ralph Beebe Blackman and John Wilder Tukey. The measurement of power spectra from the point of view of communications engineering—part i. *Bell System Technical Journal*, 37(1):185–282, 1958.

[177] Julios O. Smith III. *Introduction to Digital Filters with Audio Applications.* https://ccrma.stanford.edu/~jos/filters/Group_Delay.html, 2007. Online; accessed July 16, 2019.

[178] L Griffiths. Rapid measurement of digital instantaneous frequency. *IEEE Transactions on Acoustics, Speech, and Signal Processing*, 23(2):207–222, 1975.

[179] Paul H Kim. *Nanoscale Torsional Optomechanics.* University of Alberta, 2014.

[180] MA Mohammad, T Fito, J Chen, S Buswell, M Aktary, M Stepanova, and SK Dew. Systematic study of the interdependence of exposure and development conditions and kinetic modelling for optimizing low-energy electron beam nanolithography. *Microelectronic Engineering*, 87(5-8):1104–1107, 2010.

Appendix A

Nanofabrication of devices

A.1 Nanofabrication of silicon devices

The silicon microdisks and cantilevers measured in Chapters 3 and 4 were fabricated at the Interuniversity Microelectronics Center (IMEC) foundry, where a deep UV photolithography process and subsequent etch was used to pattern the 220 nm silicon film. Post processing of the wafers received from IMEC were performed, which included dicing of wafers into 1 cm × 1 cm chips, and release of the mechanical resonators by removal of a SiO_2 layer with a buffered oxide etch. Post processing of the chips was performed by Paul Kim and further fabrication details are available in his masters thesis [179].

A.2 Nanofabrication of silicon nitride nanostrings

The devices measured in Chapter 5 were fabricated from wafers having a 217 nm thick high-stress LPCVD silicon nitride film covering a 3 µm sacrificial silicon dioxide layer all deposited on a silicon wafer. Wafers with films deposited on them were purchased from Rogue Valley Microdevices, which were diced to centimeter scale chips that are then individually processed.

In order to fabricate waveguides to the edge of a chip, a specialized electron-beam lithography (EBL) fabrication process was developed. Typically, when spin-coated onto a chip, resist gathers at the edge of the wafers causing thickening of the resist over millimeter distances at the edges—a process called beading. This interferes with exposure at the edge of the chips preventing accurate patterning to the edges. To avoid this problem, the chip to be patterned was first scored on the underside with a dicing saw, leaving $\sim$200 μm of silicon. The chip is cleaned with a 3:1 H_2SO_4:H_2O_2 "Piranha" solution before being spin-coated with ZEP520-A electron beam resist to a thickness of 350 nm (5 minute 180°C post-bake). Immediately following, the chip is further coated with a layer of Electra 92 conductive polymer to aid in dissipation of electron-beam current during writing. After spin coating, the chip can be easily cleaved along the score on the bottom of the chip, such that the resist forms a clean surface to the edge of the chip.

The design is then patterned on the chip with a RAITH150-Two electron beam lithography writer with a 30 kV acceleration voltage and a 215 μC/cm^2 dose, followed by cold development with the Zed N50 developer at -10 °C for 90 s. Development is stopped with a 20 s rinse in isopropyl alcohol also at -10 °C and dried with N_2.

Using the ZEP resist as a mask, the Silicon Nitride layer is etched with a CHF_3 / CF_4 reactive ion etch (Oxford Instruments PlasmaPro 80 RIE), and the ZEP mask is removed with UV exposure and gentle agitation in an acetone bath.

To release the mechanics the chip is submerged in a buffered oxide etch (BOE) bath for 50 minutes to remove $\sim$2.5 μm of the oxide layer, followed by a critical point drying (CPD) step.

A.3 Nanofabrication of silicon nitride optical microdisks

The silicon nitride optical microdisks studied an Chapter 6 were fabricated from wafers similar to the nanostrings, except with a 150 nm film of LPCVD silicon nitride on 3 μm of oxide. Low-voltage electron beam lithography (10 kV, RAITH150-Two) was used to pattern polymethyl methacrylate (PMMA) electron beam resist to enable lift-off patterning of an aluminum hard mask [180]. After development of the PMMA resist with a 7:3 IPA:water development solution, a thin layer of aluminum was deposited via electron beam evaporation. The PMMA and unwanted aluminum was removed with sonication in acetone to leave an aluminum hard mask defining disk geometry. A SF_6 reactive ion etch was performed to etch the SiN layer, after which a buffered oxide etch removed 3 μm of the buried oxide and the aluminum mask.